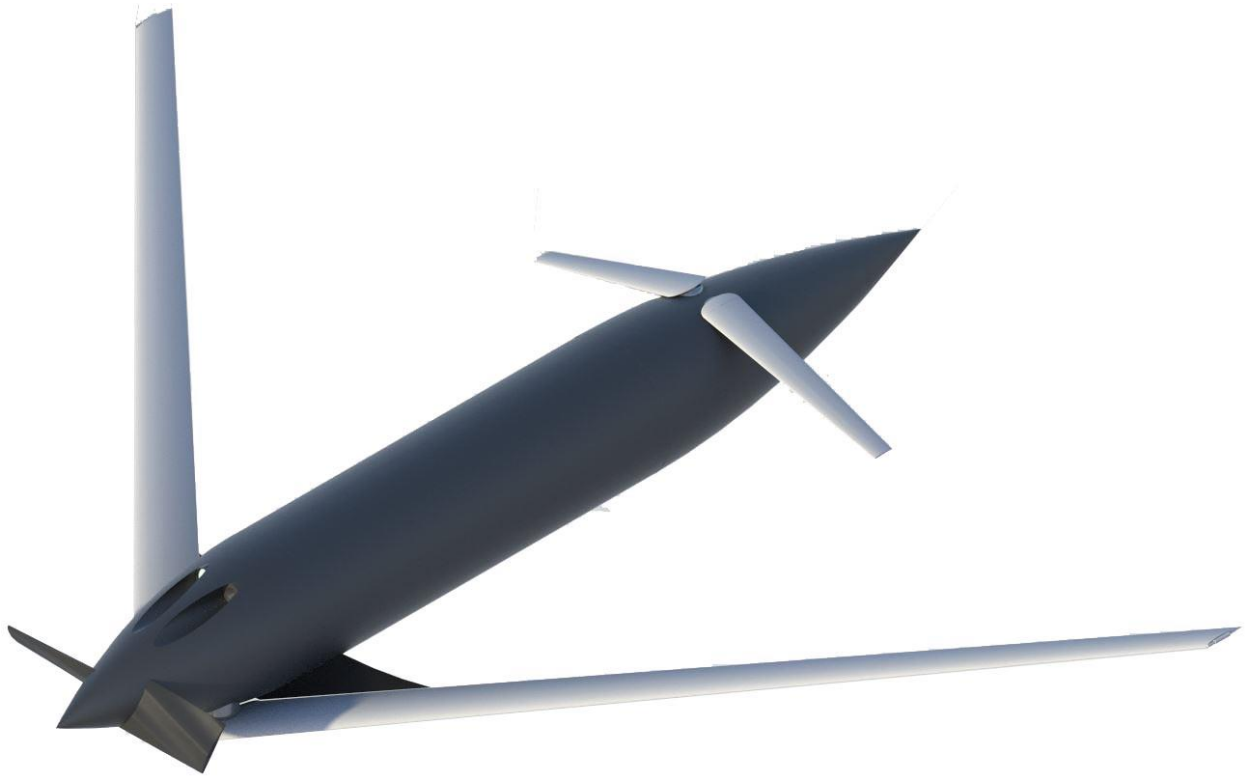





Team Valkyrie AIAA 2020-2021 Graduate Team Missile Design



Team Members			Team Advisor
 <p>Nathan Wolf</p> <p><i>Nathan Wolf</i></p> <p>ID: 998647</p>	 <p>Joe Coldiron</p> <p><i>Joseph Coldiron</i></p> <p>ID: 1230703</p>	 <p>Austin Dooley</p> <p><i>Austin Dooley</i></p> <p>ID: 936985</p>	<p>Dr. Ron Barrett</p> <p><i>Ron Barrett</i></p> <p>ID: 022393</p>



ACKNOWLEDGEMENTS

The design team would like to take this opportunity to thank several people who have supported us both in this project and throughout our time at the University of Kansas. First, we would like to recognize our families who supported us in our youth and encouraged us to pursue our passions in aerospace engineering. Secondly, we would like to thank the number of subject matter experts who reviewed our design reviews and offered advice throughout the design process. Finally, we would like to take this opportunity to thank Dr. Ron Barrett for his continual support throughout this process, and especially for his contributions to the wind tunnel testing of the model of the Valkyrie.

COMPLIANCE MATRIX

RFP Requirement	Demonstrated	Page No.
<u>Technical Requirements:</u>		
Target group 1 and 2 UAVs	Group 1 & 2 UAVs	69
Range: 3nmi (R), 3.5nmi (O)	3.5nmi from Figure 13.1	70
Intercept Altitude: 3,000ft (R), 5,000ft (O)	6,000ft from Figure 12.1	68
Weight of launcher + one missile < 40lbs	Launcher weight: 5.6 lb Missile Weight: 0.5 lb Net Weight: 14 lb Total: 20.1 lb	33,34,37
Weight of launcher + 10 missiles < 125lbs	Launcher Weight: 5.6 lb Ten Missiles: 5 lb Net Weight: 14 lb Total: 24.6 lb	33-34,37
Distribution between 3 personnel with < 50lbs per individual	System overall weight under 25 lbs	33,34,37
Capable of raid scenario (detect, acquire, target, and engage up to 10 UAVs in an hour)	M203 rate of fire: 5-7 rounds/minute	37
System compatible with safe storage, transportation, and handling requirements for at least 10 years without maintenance	Stored for 10+ years	30
Decibel noise level < 120dBA within 100ft of launch location	<120dBA within 100 ft	39-40
Acceleration < 2g's at launch	<2g's at launch	40
Payloads capable of changing in < 5 minutes	Not Applicable	N/A
Production run of 200 missiles and 20 launchers a year for 10 years, plus 15 missiles for development testing	Table 19.1.1	81
Initial operational capability before December 2027	Development Plan	82

Data Requirements:		
Concepts of Operation	Launcher, Engagement, and Recovery System	39, 41-52
Performance Assessments	Shotgun range testing, Acoustic Vector Sensors, Antenna Range, Wind Tunnel and Flight Testing	23-26, 41-44, 61-66, 89-91
System Analysis	Engagement System, Battery Sizing and Propulsion, Avionics and Sensors, Weight and Balance, Stability and Control Wind Tunnel and Flight Testing	23-26, 30-34, 41-66, 21,71, 72-80, 89-91
Cost Estimate	Cost Estimate	81-82
Development Plan	Development Plan	82-89
Deliverables	200 missiles/year for 10 years, plus 15 test missiles	81-89

Table of Contents

LIST OF SYMBOLS 4

LIST OF TABLES 8

LIST OF FIGURES 8

1. INTRODUCTION, MISSION SPECIFICATION AND PROFILE 11

1.1. MISSION PROFILES..... 12

2. MARKET REVIEW AND COMPETITION IN THE MARKET 13

3. DESIGN OPTIMIZATION FUNCTION 17

3.1. OPTIMIZATION FUNCTION..... 17

4. STAMPED DATA PRESENTATION 19

5. CLASS I WEIGHT SIZING 21

6. DESIGN OF ENGAGEMENT SYSTEM..... 22

7. WING, BATTERY, AND POWERPLANT SIZING..... 30

8. CLASS I CONFIGURATION MATRIX AND DOWN SELECTION 35

8.1. MAJOR IMPACTS ON DESIGN 35

8.2. CONCEPT OF OPERATIONS 35

8.3.	CONFIGURATION AND DOWN SELECTION	35
8.4	CONCLUSIONS.....	36
9.	CLASS II LAUNCHER, ENGAGEMENT AND RECOVERY SYSTEMS	37
10.	SENSOR, GUIDANCE, NAVIGATION, & COMUNICATION SYSTEM DESIGN	41
11.	V-N DIAGRAM	67
12.	DOGHOUSE PLOT AND MANEUVERABILTIY DIAGRAM.....	68
13.	PAYLOAD-RANGE DIAGRAM	70
14.	CLASS II WEIGHT AND BALANCE	71
14.1.	WEIGHT AND BALANCE CALCULATIONS.....	71
14.2.	CONCLUSIONS.....	71
15.	CLASS I STABILITY AND CONTROL ANALYSIS	72
16.	CLASS I DRAG POLAR	75
17.	ANALYSIS OF WEIGHT AND BALANCE, STABILITY AND CONTROL, AND L/D RESULTS	76
18.	CLASS II STABILITY AND CONTROL.....	77
19.	COST ANALYSIS AND DEVELOPMENT PLAN.....	82
19.1.	COST ANALYSIS.....	82
19.2.	DEVELOPMENT PLAN.....	83
20.	WIND TUNNEL AND FLIGHT TESTING.....	90
20.1.	WIND TUNNEL AND FLIGHT TEST MODEL FABRICATION	90
20.2.	WIND TUNNEL TESTING	91
20.3.	FREEFLIGHT AND SPIN TESTING.....	92

LIST OF SYMBOLS

<u>Acronym</u>	<u>Definition</u>	<u>Units</u>
AVS	Acoustic Vector Sensor	~
c	Speed of Light	m/s
C_{D_1}	Airplane Steady State Drag Coefficient	~
$C_{D_{ivee}}$	Airplane Drag Coefficient Due to V-tail Incidence Derivative	rad ⁻¹
C_{D_u}	Airplane Drag Due to Speed Derivative Coefficient	~

C_{Dq}	Airplane Drag Coefficient Due to Drag Coefficient	rad^{-1}
$C_{D\alpha}$	Airplane Drag Coefficient Due to Angle of Attack Derivative	rad^{-1}
$C_{D\dot{\alpha}}$	Airplane Drag Coefficient Due to Angle of Attack Rate Derivative	rad^{-1}
C_{L_1}	Airplane Steady State Lift Coefficient	\sim
$C_{L_{i_{vee}}}$	Airplane Lift Coefficient Due to V-tail Incidence Derivative	rad^{-1}
C_{Lq}	Airplane Lift Coefficient Due to Pitch Rate Derivative	rad^{-1}
C_{Lu}	Airplane Lift Coefficient Due to Speed Coefficient	\sim
$C_{L\alpha}$	Airplane Lift Curve Slope including any Flap Effects	rad^{-1}
$C_{L\dot{\alpha}}$	Airplane Lift Coefficient Due to Angle of Attack Rate Derivative	rad^{-1}
$C_{l_{i_{vee}}}$	Airplane Rolling Moment Coefficient Due to V-tail Incidence Derivative	rad^{-1}
C_{lp}	Airplane Rolling Moment Coefficient Due to Roll Rate Derivative	rad^{-1}
C_{lr}	Airplane Rolling Moment Coefficient Due to Yaw Rate Derivative	rad^{-1}
$C_{l\beta}$	Airplane Rolling Moment Coefficient Due to Sideslip Derivative	rad^{-1}
$C_{l\dot{\beta}}$	Airplane Rolling Moment Coefficient Due to Sideslip Rate Derivative	rad^{-1}
C_{m_1}	Airplane Steady State Pitching Moment Coefficient	\sim
$C_{m_{i_{vee}}}$	Airplane Steady State Pitching Coefficient Due to V-tail Incidence Derivative	rad^{-1}
$C_{m_{T_1}}$	Airplane Steady State Thrust Pitching Moment Coefficient	\sim
$C_{m_{Tu}}$	Thrust Pitching Moment Coefficient Due to Speed Derivative	\sim
$C_{m_{T\alpha}}$	Thrust Pitching Moment Coefficient Due to Angle of Attack Derivative	rad^{-1}
C_{mq}	Airplane Pitching Moment Coefficient Due to Pitch Rate Derivative	rad^{-1}
C_{mu}	Airplane Pitching Moment Coefficient Due to Speed Derivative	\sim
$C_{m\alpha}$	Pitching Moment Coefficient Due to Angle of Attack Derivative	rad^{-1}

$C_{m\alpha}$	Airplane Pitching Moment Coefficient Due to Angle of Attack Derivative	rad^{-1}
$C_{nT\beta}$	Airplane Thrust Yawing Moment Coefficient Due to Sideslip Derivative	rad^{-1}
$C_{n_{i\text{vee}}}$	Airplane Yawing Moment Coefficient Due to V-tail Incidence Derivative	rad^{-1}
C_{np}	Airplane Yawing Moment Coefficient Due to Roll Rate Derivative	rad^{-1}
C_{nr}	Airplane Yawing Moment Coefficient Due to Yaw Rate Derivative	rad^{-1}
$C_{n\beta}$	Airplane Yawing Moment Coefficient Due to Sideslip Derivative	rad^{-1}
$C_{n\dot{\beta}}$	Airplane Yawing Moment Coefficient Due to Sideslip Rate Derivative	rad^{-1}
$C_{T_{x_1}}$	Airplane Steady State Thrust Coefficient	\sim
$C_{T_{x_u}}$	Airplane Thrust Due to Speed Derivative Coefficient	\sim
$C_{T_{z_1}}$	Airplane Steady State Thrust Force Coefficient	rad^{-1}
$C_{yT\beta}$	Airplane Thrust Sideforce Coefficient Due to Sideslip Derivative	rad^{-1}
$C_{y_{i\text{vee}}}$	Airplane Sideforce Coefficient Due to V-tail Incidence Derivative	rad^{-1}
C_{yp}	Airplane Sideforce Coefficient Due to Roll Rate Derivative	rad^{-1}
C_{yr}	Airplane Sideslip Coefficient Due to Yaw Rate Derivative	rad^{-1}
$C_{y\beta}$	Airplane Sideforce Coefficient Due to Sideslip Derivative	rad^{-1}
$C_{y\dot{\beta}}$	Airplane Sideforce Coefficient Due to Sideslip Rate Derivative	rad^{-1}
C-UAS	Counter-Unmanned Aerial System	\sim
f	Frequency	MHz
G_r	Receive Gain	dBm
G_t	Transmit Gain	dBm
g	Acceleration of Gravity	m/s^2
h	Height	m
L	Length	m
L_g	Patch Antenna Length	m

L_p	Roll Angular Acceleration Imparted to the Airplane as a Result of a Unit Change in Roll Rate	s^{-1}
L_{δ_a}	Rolling Moment Due to Aileron Deflection	s^{-2}
M_q	Pitch Angular Acceleration Imparted to the Airplane as a Result of a Unit Change in Pitch Rate	s^{-1}
$M_{\dot{\alpha}}$	Pitch Angular Acceleration Imparted to the Airplane as a Result of a Unit Change in Rate of Change of Angle of Attack	s^{-1}
M_{α}	Pitch Angular Acceleration Imparted to the Airplane as a Result of a Unit Change in Rate of Angle of Attack	s^{-2}
N_r	Yaw Angular Acceleration Imparted to the Airplane as a Result of a Unit Change in Yaw Rate	s^{-1}
N_{β}	Yaw Angular Acceleration Imparted to the Airplane as a Result of a Unit Change in Sideslip Angle	s^{-2}
P_{max}	Maximum Roll Rate	deg/sec
P_r	Receive Power	mW
P_t	Transmit Power	mW
R	Distance between Antennas	m
SWAP-C	Size, Weight, Power, and Cost	~
U_1	Steady State Speed	m/s
UAS	Unmanned Aerial System	~
UAV	Unmanned Aerial Vehicle	~
W	Width	m
W_e	Empty Weight	lb
$W_{oe,tent}$	Tentative operating empty weight	lb
W_{to}	Takeoff weight	lb
Y_r	Lateral Acceleration Imparted to the Airplane as a Result of a Unit Change in Yaw Rate	ft/s
Y_{β}	Lateral Acceleration Imparted to the Airplane as a Result of a Unit Change in Sideslip Angle	ft/s ²
Z_{α}	Vertical Acceleration Imparted to the Airplane as a Result of a Unit Change in Angle of Attack	ft/s ²
Greek Symbols		
δ_a	Aileron Deflection	deg
ϵ_r	Refractive Index	~

ϵ_{reff}	Effective Refractive Index	~
λ	Wavelength	m
ζ_D	Dutch Roll Damping Ratio	~
ζ_P	Phugoid Damping Ratio	~
ζ_{SP}	Short Period Damping Ratio	~
ω_{nD}	Dutch Roll Natural Frequency	rad/sec
ω_{nP}	Phugoid Natural Frequency	rad/sec
ω_{nSP}	Short Period Natural Frequency	rad/sec

LIST OF TABLES

Table 1.1: Technical Requirements [1].....	11
Table 3.1.1: Mission Requirements	17
Table 3.1.2: Design and Ancillary Objectives	18
Table 6.1 Initial Designs Considered for Engagement System.....	22
Table 6.2 Shotgun Based Engagement Systems	23
Table 7.1: Sizing constants [11].....	30
Table 8.8.3.1 Configuration Down selection and Objective Function.....	36
Table 10.1: Sensor, Guidance, and Communication System Power Draw	45
Table 10.2: Valkyrie Characteristics.....	56
Table 10.3: Antenna Properties Summary	66
Table 17.1 Longitudinal and Directional Stability.....	76
Table 18.1: Class II Stability and Control Variables	78
Table 18.2: Stability and Control Derivatives.....	81
Table 19.1.1: Cost analysis of program development.....	82

LIST OF FIGURES

Figure 1.1.1: Three possible mission profiles: A, B, and C	12
Figure 2.1: Fortem Technology DroneHunter [4].....	13
Figure 2.2: DroneHunter Concept of Operations.....	14
Figure 2.3: AMTEC Skynet Mi5 [4].....	14
Figure 2.4: OpenWorks Skywall [6].....	15
Figure 2.5: Centrifugal Net Deployment CONOPS.....	15
Figure 2.6: IXI Technology Dronekiller [8]	15
Figure 2.7: RF Blocker Concept of Operations	16

Figure 4.1: RF Jammers Graphed	19
Figure 4.2 Kinetic Weapons (Top) and Unconventional (Bottom) Market Competitors	20
Figure 6.1 Emptied 12-Gauge Shells (left) and Weight of Shot (right).....	24
Figure 6.2 Catalogue of Tests Including Effectiveness Test Against a Tree Branch.....	25
Figure 6.3 ARMRS Assembly Diagram	28
Figure 6.4 ARMRS Installed Onboard the Valkyrie System (rendered in clear polycarbonate to show shell detail)	29
Figure 7.1: 1998 DARPA MAV Program Battery Densities [10]	31
Figure 7.2 BEMT Equations [13]	32
Figure 7.3 Power Required vs Wing Area For 200g (top) and 220g (bottom) Aircraft.....	33
Figure 7.4 Sizing Chart for 210.2 g Aircraft Tuned Battery Size	34
Figure 8.8.3.1 Configuration Sweep	36
Figure 9.1 M203 Grenade Launcher	37
Figure 9.2 Compact Net Packing	38
Figure 9.3 M203 Grenade Launcher with 90th Percentile Male 10th Percentile Female	38
Figure 9.4 Net Capture System.....	39
Figure 9.5 M203 with Silencer	40
Figure 10.1: Pair of anemometer wires [19]	41
Figure 10.2: 3D acoustic vector sensor [19]	42
Figure 10.3: Hans-Elias de Bree’s Helicopter Test [19].....	42
Figure 10.4: Hans-Elias De Bree’s Gunshot Test [19]	44
Figure 10.5: Sensor, Guidance, and Communication System Design	45
Figure 10.6: Valkyrie Loading.....	46
Figure 10.7: M203 Firing the Valkyrie System	47
Figure 10.8: Valkyrie Cruise and Acoustic Vector Sensor Lock-on of Hostile UAS.....	48
Figure 10.9: Valkyrie Pulls Ahead of Hostile UAS.....	49
Figure 10.10: Valkyrie Discards Tail Cone and Cloth Wing.....	50
Figure 10.11: Valkyrie ARMRS System Engagement of UAS and Simultaneous Forward Wing Shift....	51
Figure 10.12: Valkyrie Glides into Net.....	52
Figure 10.13: Valkyrie Acoustic Vector Sensor Lock-on of Enemy Sniper.....	53
Figure 10.14: Valkyrie Acoustic Vector Sensor Lock-on of Enemy Artillery	54
Figure 10.15: Valkyrie 3-view with Folded, Cruise, and Glide Configurations Shown.....	55
Figure 10.16: Valkyrie Electronics	57
Figure 10.17: Valkyrie Internal Structure	58
Figure 10.18: Valkyrie Exploded View	59
Figure 10.19: Valkyrie Reloading.....	60
Figure 10.20: Dipole Antenna in HFSS	62
Figure 10.21: Dipole Return Loss and Resonant Frequency before Tuning.....	62
Figure 10.22: Dipole Return Loss and Resonant after Tuning	62
Figure 10.23: Dipole Realized Gain Polar Plot.....	62
Figure 10.24: Dipole Radiation Pattern	63
Figure 10.25: Patch Antenna in HFSS	63
Figure 10.26: Patch Return Loss and Resonant Frequency	64

Figure 10.27: Patch Realized Gain Polar Plot.....	64
Figure 10.28: Patch Radiation Pattern	65
Figure 11.1 Valkyrie V-n Load Diagram.....	67
Figure 12.1 Doghouse Plot	68
Figure 12.2 Maneuverability Diagram.....	69
Figure 13.1 Valkyrie Payload Range Diagram for Cruise Altitude of 6000 ft	70
Figure 15.1 Longitudinal Stability X-Plot Before and After Shot	73
Figure 15.2 Directional Stability X-Plot.....	74
Figure 16.1 Perimeter Plot	75
Figure 18.1: Longitudinal Damping Ratio Levels Achieved.....	78
Figure 18.2: Spiral and Dutch Roll Levels Achieved	78
Figure 18.3: AAA Trim Diagram	80
Figure 19.1.1: Estimated Price per Missile at Various Production Runs on a Logarithmic Scale.....	83
Figure 19.2.1: Skin Manufacturing and Assembly Diagram	84
Figure 19.2.2: Wing Manufacturing and Assembly Diagram.....	85
Figure 19.2.3: V-tail Manufacturing and Assembly Diagram	85
Figure 19.2.4: ARMRS Manufacturing and Assembly Diagram.....	87
Figure 19.2.5: Internal Structure and Electronics Manufacturing and Assembly Diagram	88
Figure 19.2.6: Final Assembly and Testing Diagram	89
Figure 20.1.1: Wind Tunnel Model Dimensions	90
Figure 20.1.2: Wind Tunnel Model During Fabrication.....	91
Figure 20.1.1: 100% Scale Wind Tunnel Model	91
Figure 20.2.1: 100% Scale Wind Tunnel Model in KU 3 x 4' Tunnel.....	92
Figure 20.3.2: 100% Scale Model prior to Spin Test Launch.....	92

1. INTRODUCTION, MISSION SPECIFICATION, AND PROFILE

The objective of this project is to respond to the request for proposal by AIAA to design a shoulder-launched anti-UAV missile. The missile can have either lethal or non-lethal means to destroy or disable the UAV. As UAVs are highly maneuverable, the missile shall demonstrate that it is capable of endgame maneuvers. In addition, this report provides engineering analysis and total system design associated with this missile system including personnel effects. This report determines a system concept that best satisfies mission requirements and goals stated in the RFP and describes the design process, the physical and performance characteristics of the final system design and its components, an operational concept, cost estimate, development plan, and necessary support equipment and other resources necessary to comply with the technical requirements [1].

Table 1.1: Technical Requirements [1]

Target UAVs	Group 2 UAVs (threshold) – group 1 UAVs (objective)
Range	3 nmi (threshold) – 3.5 nmi (objective)
Service ceiling	3,000 ft (threshold) – 5,000 ft (objective)
Launcher + 1 missiles weight	< 40 lb
Launcher + 10 missiles weight	< 125 lb
Launcher + 10 missiles pack weight	< 50 lb (distributed across 3 people)
Interdiction rate	≥10 UAVs/hour
System storage without maintenance	≥ 10 years
Warhead arming distance (if used)	≥ 200 ft
Noise level withing 100 ft of launch	≤ 120 dBa
Launch acceleration	≤ 2 g's
Time to change payload (if used)	≤ 5 minutes
Production rate	200 missiles and 20 launchers a year for 10 years plus 15 missiles for development testing
System initial operating capability	≤ December 2027

1.1. MISSION PROFILES

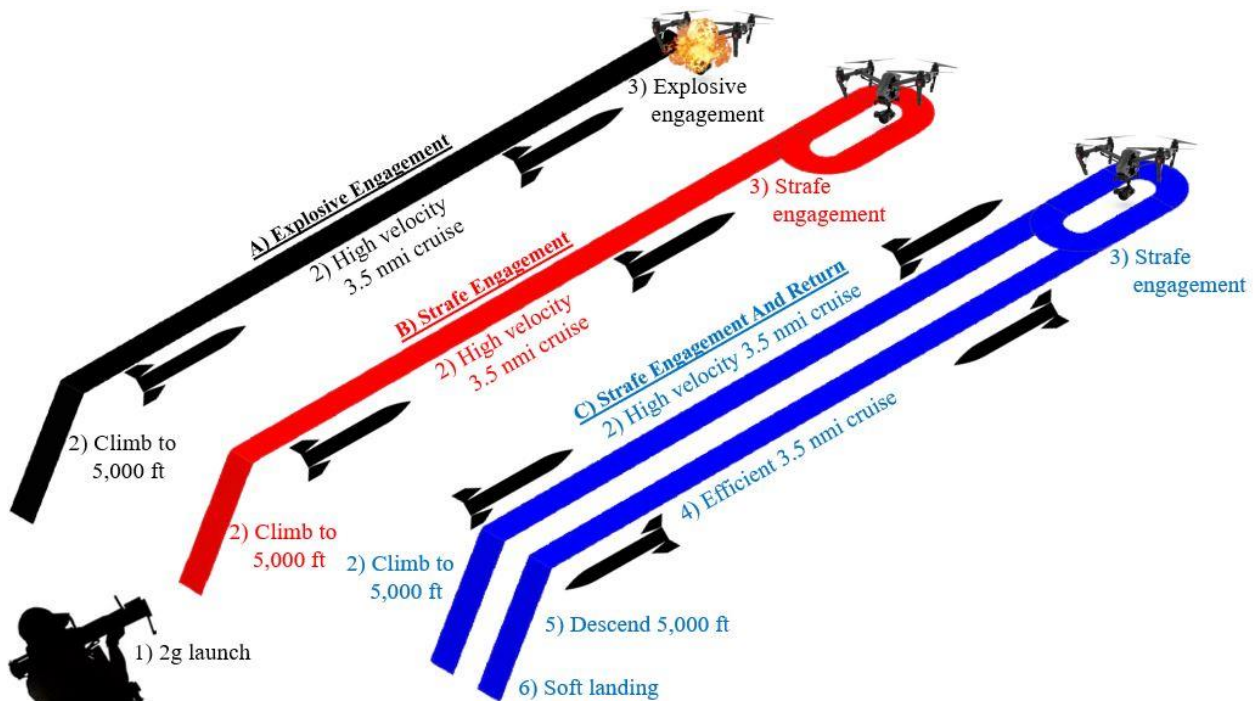


Figure 1.1.1: Three possible mission profiles: A, B, and C

Based on initial technical requirements, three possible mission profiles were considered as shown above. The first is a typical shoulder launched missile explosive engagement. The second is a non-explosive engagement such as a net or other entanglement mechanism. The third is a reusable system. As seen in further sections of this report, the Valkyrie system design most closely resembles this third mission profile in order to capitalize on the reusability of the system and the cost benefits associated with such a design.

2. MARKET REVIEW AND COMPETITION IN THE MARKET

Current counter-unmanned aircraft systems (C-UAS) must partially rely on non-traditional methods to detect the presence of hostile or unauthorized small UAS because of their inability to be detected based on their size, construction, and flight altitude. These methods include using electro-optical, infrared, or acoustic sensors to detect targets by visual, heat, or sound signatures [2]. Radar systems are another method, but unreliable due to the signature and size of small UAS. Identifying the wireless signal used to control these systems can also be used. For redundancy, most of these systems can be combined to provide more reliable systems.

After detecting UAS, a number of methods can be used to disable or destroy them. This includes jamming their signals to interfere with communications to their operator, or using guns, nets, directed energy, traditional air defense systems, or trained animals such as eagles [2]. Because the threat of small UAS has developed within the last few years, most C-UAS systems are very new or still in development.

One of the most capable C-UAS is Fortem Technology's DroneHunter. This drone is a fully autonomous system that detects, classifies, and captures drones within a geofenced area. The air-to-air system uses SWAP-C electronically scanned phased array radar that allows for good range, resolution, accuracy, and clutter rejection, and can be used day or night in different kinds of weather.



Figure 2.1: Fortem Technology DroneHunter [4]

After identifying its target, the DroneHunter can track and follow the target until it captures it with a net and carries it to a safe location [3].

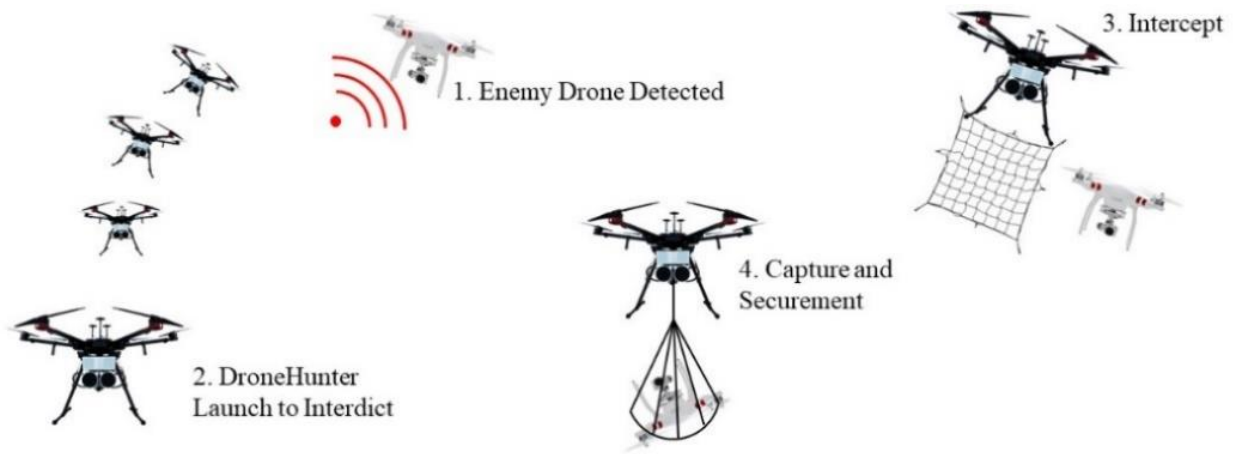


Figure 2.2: DroneHunter Concept of Operations

Low-cost solutions for close range defense utilize nets fired by humans. AMTEC's Skynet Mi5 is a 12 gauge round fired through a choked and rifled 12-gauge shotgun. It contains five segments that use centrifugal force to separate and create a 5-foot-wide net to trap and disable a drone. It was developed for rapid deployment to defend against commercially available drones [4]. Drone Defense' NetGun X1, developed in the UK, is a handheld gun that can shoot two different kinds of nets up to 15 meters and is mainly catered toward law enforcement and security [5]. Neither of these systems are automated and would likely only be considered last resort systems for military defense applications.



Figure 2.3: AMTEC Skynet Mi5 [4]

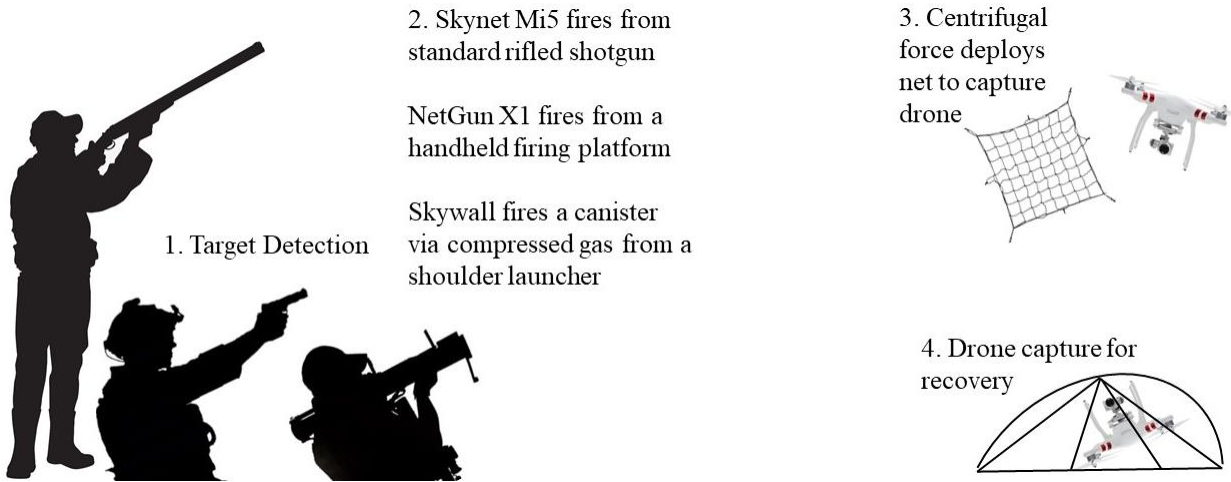


Figure 2.4: Centrifugal Net Deployment CONOPS

OpenWorks Engineering’s Skywall system is a man-portable shoulder launcher that uses compressed gas to launch a projectile toward a drone using its SmartScope technology that compensates for the drone’s speed and range automatically. The projectile explodes into a net that then captures and disables the drone causing it to fall to the ground. It has two kinds of reusable projectiles--one with a net only and one with a net and parachute--that are pre-programmed by the gun’s targeting system to expand the net at the right time (Figure 2.5) [7].



Figure 2.5: OpenWorks Skywall [6]



Figure 2.6: IXI Technology Dronekiller [8]

IXI Technology’s Dronekiller is another man-portable handheld C-UAS that utilizes software defined radio. This allows the system to target the specific frequencies a drone is using and add noise or additional data to the signal to break the link between the drone and operator. It also works against drones capable of channel-hopping while still only blocking

certain frequencies so as to not jam other nearby devices using similar frequencies. The loss of communication between the drone and operator causes the drone to return to its home base (Figure 2.7) [8].

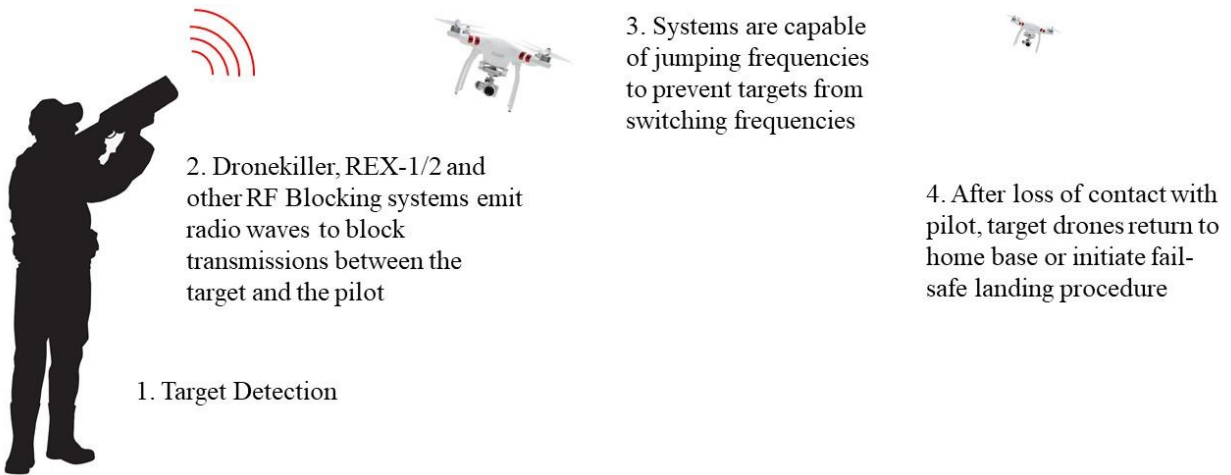


Figure 2.7: RF Blocker Concept of Operations

3. DESIGN OPTIMIZATION FUNCTION

The purpose of this chapter is to develop the optimization function for the anti-UAV system. Mission requirements (Table 3.1.1) are based on technical requirement thresholds. Mission objectives are based on cost and mission effectiveness as well as objectives listed in the technical requirements. Ancillary objectives (Table 3.1.2) are based on subject matter expert feedback. From these requirements and objectives, the optimization function can be found using the following equation:

$$\text{General Optimization Function} = \text{GOF} = \prod_1^i R_i \left(\frac{1}{m} \sum_1^m O_j + \frac{1}{n\text{ROWF}} \sum_1^n AO_k \right)$$

3.1. OPTIMIZATION FUNCTION

Table 3.1.1: Mission Requirements

R₁	Target UAV size	{ 1 if missile can disable group ≤ 2 UAVs 0 if missile can disable group > 2 UAVs
R₂	Range	{ 1 if range ≥ 3 nmi 0 if range < 3 nmi
R₃	Service ceiling	{ 1 if altitude ≥ 3,000 ft above ground level 0 if altitude < 3,000 ft above ground level
R₄	Launcher + 1 missiles weight	{ 1 if weight of launcher + 1 missile ≤ 40 lb 0 if weight of launcher + 1 missile > 40 lb
R₅	Launcher + 10 missiles weight	{ 1 if weight of launcher + 10 missiles ≤ 125 lb 0 if weight of launcher + 10 missiles > 125 lb
R₆	Launcher + 10 missiles pack weight	{ 1 if $\frac{\text{weight of launcher + 10 missiles}}{3 \text{ people}} \leq 50 \text{ lb}$ 0 if $\frac{\text{weight of launcher + 10 missiles}}{3 \text{ people}} > 50 \text{ lb}$
R₇	Interdiction rate	{ 1 if interdiction rate ≥ 10 UAVs/hour 0 if interdiction rate < 10 UAVs/hour
R₈	System storage without maintenance	{ 1 if storage without maintenance ≥ 10 years 0 if storage without maintenance < 10 years
R₉	Warhead arming distance (if used)	{ 1 if warhead arming distance ≥ 200 ft 0 if warhead arming distance < 200 ft
R₁₀	Noise level withing 100 ft of launch	{ 1 noise within 100 ft ≤ 120 dBa 0 noise within 100 ft > 120 dBa
R₁₁	Launch acceleration	{ 1 if launch acceleration ≤ 2 g's 0 if launch acceleration > 2 g's
R₁₂	Time to change payload	{ 1 if time to change payload ≤ 5 min 0 if time to change payload > 5 min
R₁₃	System initial operating capability	{ 1 if IOC ≤ December 2027 0 if IOC > December 2027
R₁₄	Production rate	200 missiles and 20 launchers a year for 10 years plus 15 missiles for development testing

Table 3.1.2: Design and Ancillary Objectives

O₁	Target UAV size	$\begin{cases} \frac{1}{2} & \text{if missile can disable group 2 UAVs} \\ 1 & \text{if missile can disable group 1 UAVs} \end{cases}$
O₂	Range	$\begin{cases} \frac{\text{Range} - 3 \text{ nmi}}{0.5 \text{ nmi}} & \text{if } 3 \text{ nmi} < \text{Range} < 3.5 \text{ nmi} \\ 1 & \text{if range } \geq 3.5 \text{ nmi} \end{cases}$
O₃	Service ceiling	$\begin{cases} \frac{\text{Service ceiling} - 3,000 \text{ ft}}{2,000 \text{ ft}} & \text{if } 3,000 \text{ ft} < \text{service ceiling} < 5,000 \text{ ft} \\ 1 & \text{if range } \geq 5,000 \text{ ft} \end{cases}$
O₄	Kill probability	$\begin{cases} \left(\frac{\text{PK} - 90\%}{10\%}\right)^2 & \text{if } 90\% < \text{PK} < 100\% \\ 1 & \text{if Pk} = 100\% \end{cases}$
O₅	Minimum cost	$\frac{\text{Cost}_{\text{Competitive system}} - \text{Cost}_{\text{Valkyrie system}}}{\text{Cost}_{\text{Competitive system}}}$
O₆	Minimum complexity	$\frac{\text{Part count}_{\text{Competitive system}} - \text{Part count}_{\text{Valkyrie system}}}{\text{Part count}_{\text{Competitive system}}}$
O₇	Minimum weight	$\frac{W_{\text{Competitive system}} - W_{\text{Valkyrie system}}}{W_{\text{Competitive system}}}$
AO₁	Interoperable with civil airspace and law enforcement	$\begin{cases} 1 & \text{if interoperable with civil airspace/law enforcement} \\ 0 & \text{if not interoperable with civil airspace/law enforcement} \end{cases}$
AO₂	Compatible with FCC and FAA regulations	$\begin{cases} 1 & \text{if compatible with FCC and FAA regulations} \\ 0 & \text{if not compatible with FCC and FAA regulations} \end{cases}$
AO₃	Optional hard launch	$\begin{cases} 1 & \text{if hard launch capable} \\ 0 & \text{if not hard launch capable} \end{cases}$
AO₄	No energetics	$\begin{cases} 1 & \text{if no energetics used} \\ 0 & \text{if energetics used} \end{cases}$
AO₅	No pyrotechnics	$\begin{cases} 1 & \text{if no pyrotechnics used} \\ 0 & \text{if pyrotechnics used} \end{cases}$
AO₆	Safe bystander engagement	$\begin{cases} 1 & \text{if safe bystander engagement method} \\ 0 & \text{if unsafe bystander engagement method} \end{cases}$
AO₇	Day/night/all-weather interdiction capability	$\begin{cases} 1 & \text{if day/night/all - weather interdiction capability} \\ 0 & \text{if no day/night/all - weather interdiction capability} \end{cases}$
AO₈	Minimal training	$\begin{cases} 1 & \text{if minimal training required} \\ 0 & \text{if extensive training required} \end{cases}$
AO₉	AVS accommodation with telemetry	$\begin{cases} 1 & \text{if AVS compatible with telemetry} \\ 0 & \text{if AVS noncompatible with telemetry} \end{cases}$
AO₁₀	1 minute interception	$\begin{cases} 1 & \text{if time to intercept } \leq 1 \text{ min} \\ 0 & \text{if time to intercept } > 1 \text{ min} \end{cases}$
AO₁₁	Target UAV size	$\begin{cases} 1 & \text{if missile can disable group 3 UAVs} \\ 0 & \text{if missile can't disable group 3 UAVs} \end{cases}$

Based on subject matter expert feedback, the ancillary objectives were weighted half as much as the mission objectives leading to the following system optimization function:

$$OF = \prod_1^{14} R_i \left(\frac{1}{7} \sum_1^7 O_j + \frac{1}{11 \times \frac{1}{2}} \sum_1^{11} AO_k \right)$$

4. STAMPED DATA PRESENTATION

The following section examines the current competitors in the UAV suppression market. The examples presented in this section are divided into three categories based on the method of interdiction used to down enemy drones. The first of these methods is radio frequency jamming. RF is an engagement form where drone communication is interrupted, defaulting the drone to emergency landing or retreat procedures. This method of interdiction is measured in in hours of use per charge compared to weight. The second method of interdiction is kinetic kills, which either impact enemies destroying their components or destroying the drone itself, or trapping the enemy drone for capture. These engagement types are measured in number of interdictions compared to weight, as some like the stinger missile are single shot, while others allow multiple uses. Finally, there are a number of interdiction systems which do not fit into one of the two categories above. These are presented in the section marked other mechanisms and are tracked in number of interdictions per weight. The following page contains a graphical representation of the market competitors.

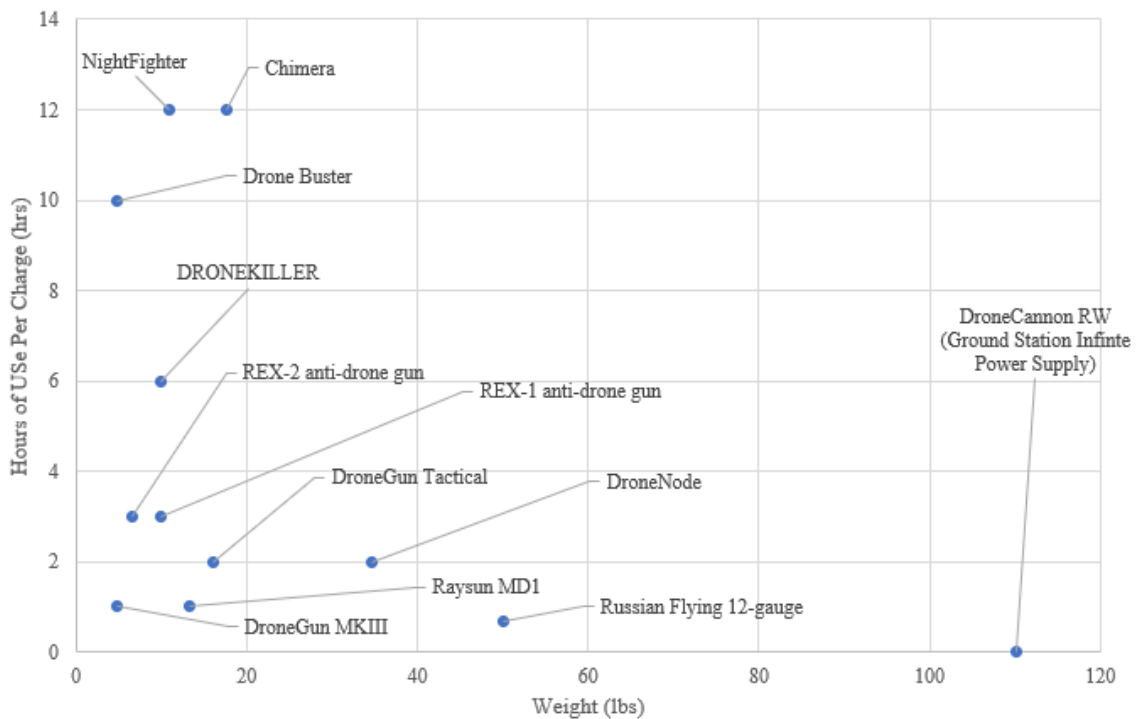


Figure 4.1: RF Jammers Graphed

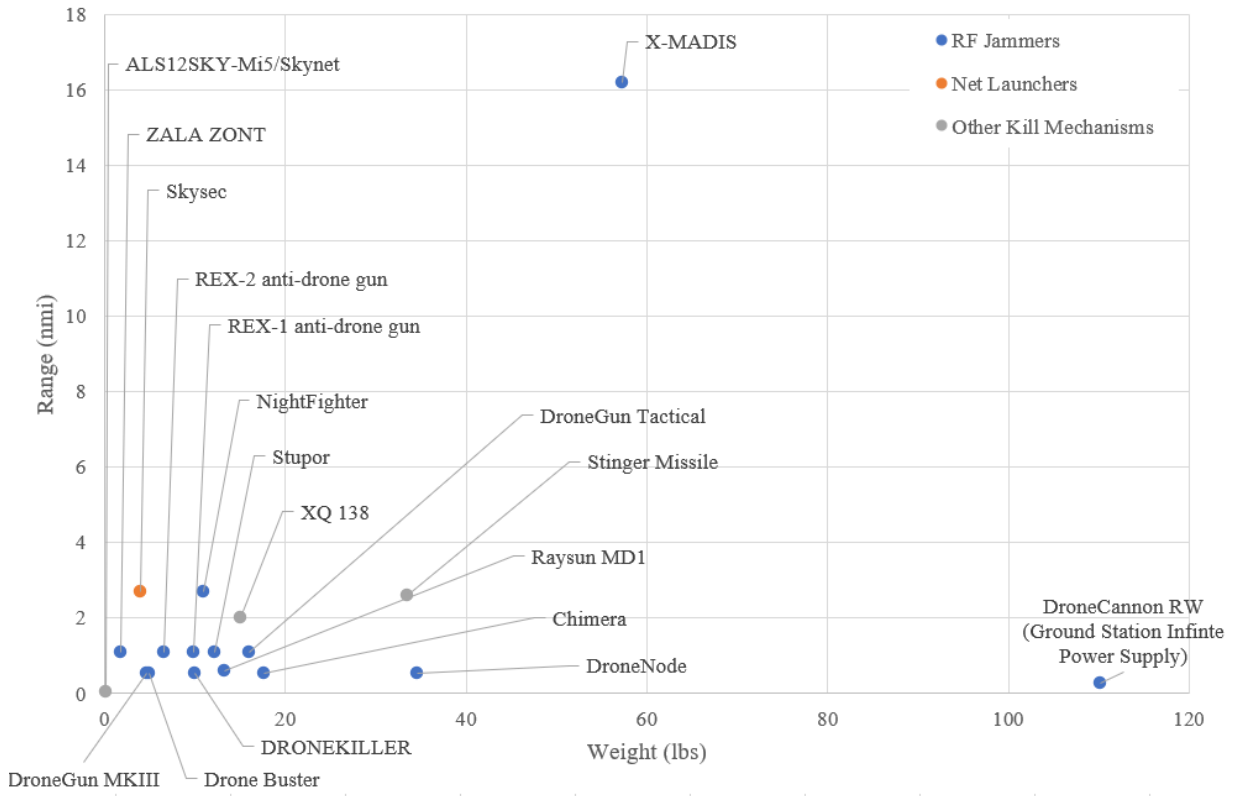
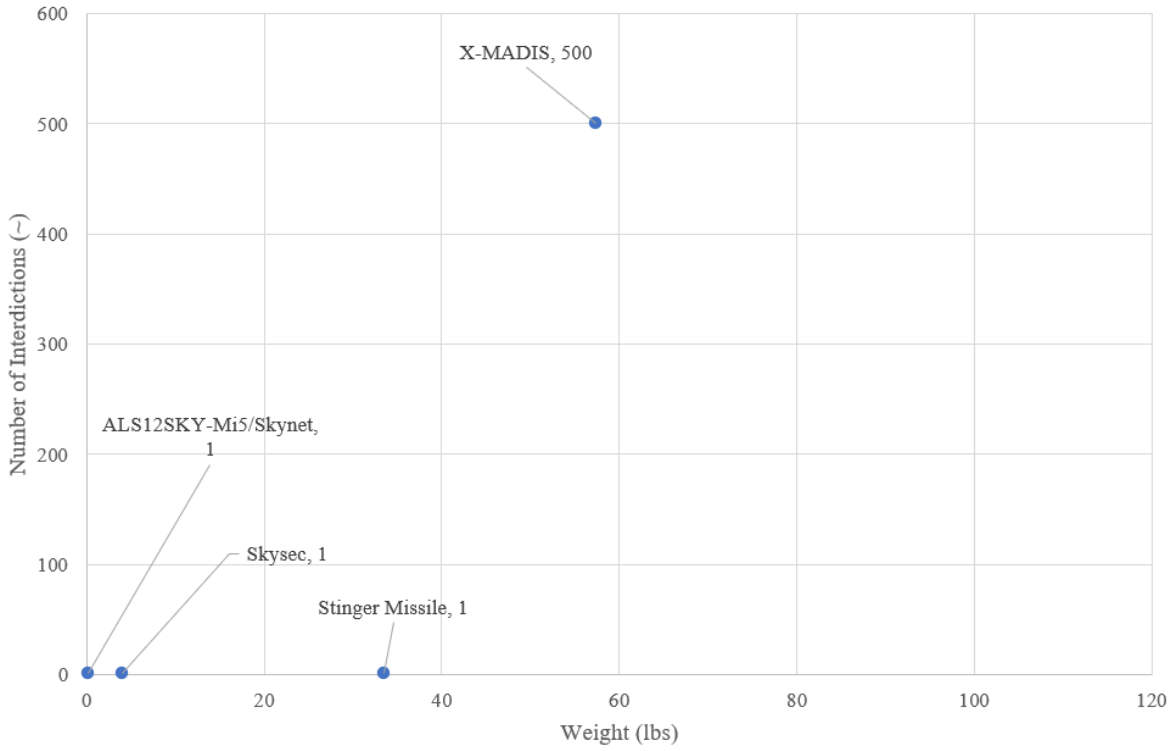


Figure 4.2 Kinetic Weapons (Top) and Unconventional (Bottom) Market Competitors

5. CLASS I WEIGHT SIZING

The weight sizing methods performed in this section are based on STAMPED analysis of empty weight to takeoff weight ratios. A modified iterative process from Dr. Jan Roskam's Airplane Design Part 1 [9] is used to estimate the takeoff, empty, and fuel weight of the system. Based on assumptions made from similar UAS in Group 1 as defined by the Department of Defense, initial preliminary estimations were made for the takeoff weight of the system and empty to takeoff weight ratio. The tentative operating empty weight is calculated based on these estimations. Empty weight and operating empty weight will always be equal because there is no weight of a crew and no trapped (unusable) fuel and oil in an electric system.

Instead of using fuel weight estimations as described in Airplane Design Part 1 [9], an alternative method is used to account for the mass of the battery in place of fuel. A lithium-thionyl chloride battery with specific power of 1000 watts/kg [10] is used to estimate the mass of the battery needed. A cruising speed of 150 ft/s is considered for the amount of power needed. For each iteration, a takeoff weight is estimated to determine the battery sizing and empty weight of the aircraft until the empty weight estimation is within 0.5% of the design point. After several iterations, a battery weight of 0.035 lbf is calculated with a payload weight of 0.11 lbf and takeoff weight of 0.29 lbf.

The final preliminary weight sizing configuration is show in Table 5.1. Unfortunately, there are very few systems currently available with similar specifications and information about them is very scarce. Many assumptions were made based on the information found through STAMPED analysis and requirements from the RFP. Sample calculations for the final preliminary weight estimations are shown in the appendix.

Table 5.1: Final Preliminary Weight Sizing

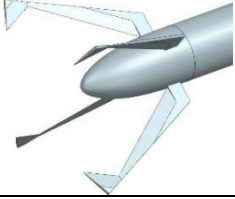
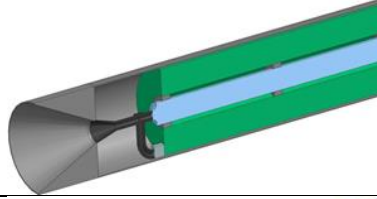
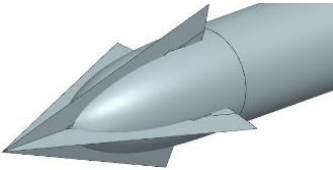
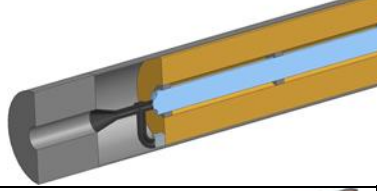
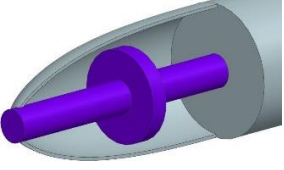
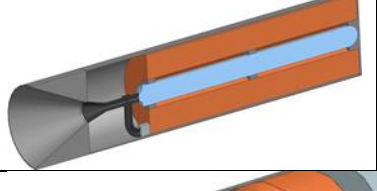
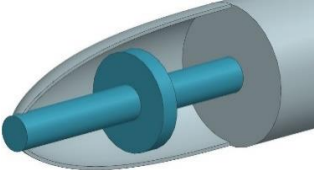
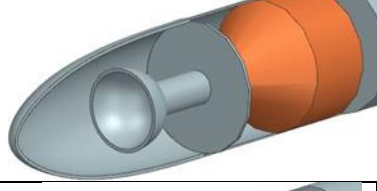
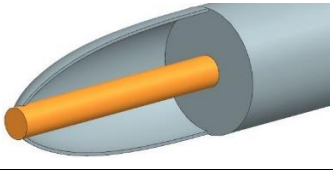
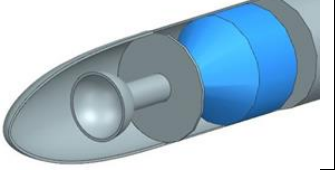
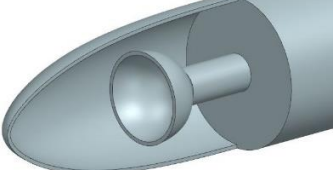

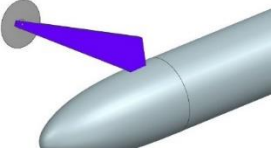
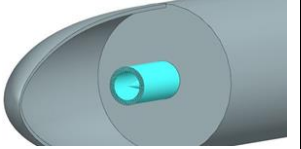
W_{to} (lbf)	$W_{battery}$ (lbf)	W_{oe} (lbf)	W_{pl} (lbf)
0.29	0.035	0.15	0.11

6. DESIGN OF ENGAGEMENT SYSTEM

This chapter of the report covers the various engagement systems considered in the design process.

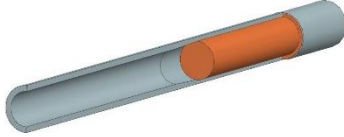
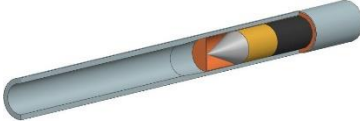
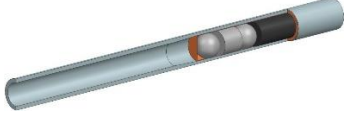
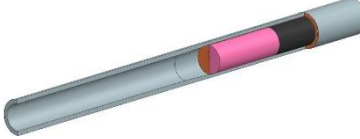
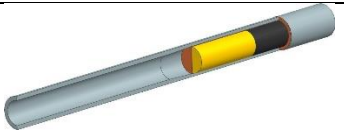
Table 6.1 below shows designs that were considered but decided against for a variety of safety and complexity concerns.

Table 6.1 Initial Designs Considered for Engagement System

Concept of Interdiction	Method	Concept of Interdiction	Method
	<p>Grapppler:</p> <ul style="list-style-type: none"> Add weight to cause loss of control 		<p>EMF Absorbing Paint:</p> <ul style="list-style-type: none"> Spray EMF absorbing paint disrupting communication
	<p>Kinetic Kill:</p> <ul style="list-style-type: none"> Ram into and pierce enemy UAVs 		<p>Expanding Foam:</p> <ul style="list-style-type: none"> Spray foam increasing drag and eliminating lift
	<p>EMP:</p> <ul style="list-style-type: none"> Short circuit enemy hardware to cause loss of control 		<p>Flamethrower:</p> <ul style="list-style-type: none"> Melt or destroy sensitive components
	<p>Electromagnet:</p> <ul style="list-style-type: none"> Corrupt or erase data Cause loss of control 		<p>Napalm Charge:</p> <ul style="list-style-type: none"> Melt or destroy sensitive components
	<p>High Power Laser:</p> <ul style="list-style-type: none"> Melt or destroy sensitive components 		<p>Explosive Charge:</p> <ul style="list-style-type: none"> Destroy enemy UAVs with an explosive blast
	<p>RF Jammer:</p> <ul style="list-style-type: none"> Interrupt communication to cause loss of control 		<p>Semi-Auto Rifle:</p> <ul style="list-style-type: none"> Tube-magazine fed .22 long rifle system
	<p>Retractable Saw:</p> <ul style="list-style-type: none"> Remove critical components 		<p>Collapsible Spear:</p> <ul style="list-style-type: none"> Ram into and pierce enemy UAV

Further design consideration produced the designs presented below in Table 6.2. These design options addressed safety concerns associated with engagement methods relying on large explosives and fire-based engagement systems, as well as energy use and mechanical complexity concerns brought up by previous designs.

Table 6.2 Shotgun Based Engagement Systems

Concept of Interdiction	Method	Concept of Interdiction	Method
	<p>.410 Shotgun:</p> <ul style="list-style-type: none"> • Destroy sensitive and un-armored components 		<p>Rope Dart:</p> <ul style="list-style-type: none"> • Destroy sensitive and un-armored components • Tether target to interceptor, allowing capture
	<p>Chain Shot:</p> <ul style="list-style-type: none"> • Chain Shot (two heavy spheres bound together with a length of chain) to shatter enemy quadcopter limbs 		<p>Net Cannon:</p> <ul style="list-style-type: none"> • Entangle propellers or engines to cause loss of control
	<p>Kevlar Wad:</p> <ul style="list-style-type: none"> • Entangle propellers or engines to cause loss of control 		

The natural limitations of range present in shotguns also addressed the concern with having a gun platform mounted to the interceptor associated with the semi-automatic rifle design discussed previously. Several of these designs were later tested according to safe handling procedures to determine effectiveness of deployment.

Range experiments were conducted at the Platte Falls Conservation Area Shotgun Range. Safety of personnel involved in the testing process as well as of any individuals not involved in the test was of the utmost importance during the testing process. In the pursuit of safety, all individuals were required to wear

hearing and eye protection during the test firing procedure. During the test firing, the shotgun used to fire the test shells was mounted to a ground stand designed to absorb recoil, secure the firearm, and to place the test individuals outside the potential danger zone. Typically when firing a shotgun or similar firearm, the user's face is placed next to the breech of the gun, and so by using the test stand, the individuals conducting the test were removed from the zone of danger in case of a breech explosion due to misloading.

Rounds tested at the range included a selection of the engagement systems outlined in Table 6.2, namely the Chain Shot and Kevlar Wad. In addition to these designs, the team also tested firing strands of Kevlar loaded loosely, strands with weight on only one end, and finally strands with a single weight brushed to form a cat of nine tails. Each test procedure began with carefully slicing the top off of a standard 12-gauge shell and carefully weighing the shot present in the shells as shown Figure 6.1. The shells were then reloaded with the test round, and the original weight was matched by supplementing the test round with pellets extracted from the standard round. After this, the shell was taped shut and carefully loaded into the shotgun. Prior to cocking the gun, safety checks were conducted to ensure that no personnel were in the field of fire and that all members present had donned proper safety gear. After completing all safety checks, the gun was cocked and fired. [One such test can be seen here.](#)

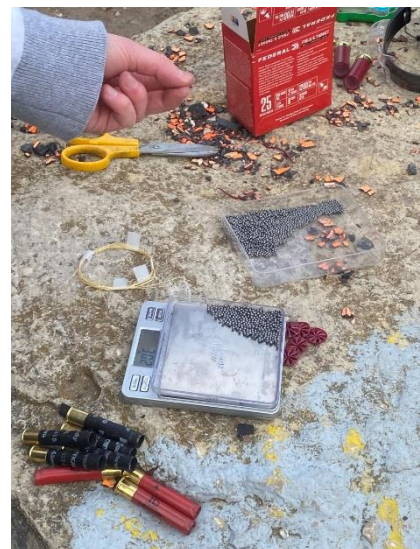


Figure 6.1 Emptied 12-Gauge Shells (left) and Weight of Shot (right)



Figure 6.2 Catalogue of Tests Including Effectiveness Test Against a Tree Branch

As seen on the previous page, the long chain design of shell loading was extremely effective. In this configuration, a Kevlar strand was tied to a split shot pellet on either end. In the effectiveness test, a single strand was loaded into a shell and filled to original capacity before being tested. This test deliberately fired the shell into a grove of trees so that the designers could track damage caused by the design. This range data was used to down select from this group of designs to the final loading of the shell which is comprised of a series of long chain shots. Using multiple chains will allow the Valkyrie to cover more area with its shot, thereby increasing the likelihood of hitting an enemy target.

After study of the market competition for the Valkyrie system, and after speaking with subject matter experts, the design of the shotgun engagement system was specially configured to feature an octagonally rifled barrel designed to impart spin on the shot and Kevlar system. This rotational velocity serves to facilitate the opening and spread pattern of the shot similar to the Skynet Mi5. To facilitate this system, extensive modifications were made to the firing assembly to mitigate recoil forces and their effects on the airframe.

The firing of the shotgun shell, following Newton's third law, imparts a huge amount of energy into the Valkyrie system. In the Skynet system, like all firearms, the barrel and structure of the launcher is orders of magnitude larger than the projectile, meaning that while the bullet experiences an acceleration to supersonic speeds, the acceleration of the firearm is in turn orders of magnitude less. The same can be said of the rotational acceleration, whereby the mass of the gun platform mitigates the angular acceleration of the firearm. Unfortunately, in the Valkyrie system, the mass of the firearm is the mass of the aircraft, meaning that the inherent ability of the gun platform to resist angular accelerations is mitigated. Initially, the authors of this report intended to allow the aircraft to absorb the angular acceleration by simply using ailerons to roll through several 360-degree revolutions. However, necessary growth of the aspect ratio of the wing increased the risk of this method overstressing the wing structure.

The complex problem presented required a unique solution. Onboard the Valkyrie system, the specially designed shotgun shell and barrel combination are mounted to the Airborne Recoil Mitigation Rotational Stabilizer or ARMRS. In this system, a two layered barrel system made from polycarbonate to reduce weight is mounted in the tail of the Valkyrie system. The outer barrel, shown in black in Figure 6.3 on the next page, is fixed and provides the mounting point for the rear tail surface. The internal barrel, shown in cream in Figure 6.3, is mounted in such a way as to prevent removal while allowing rotation about the central axis of the vehicle. The inner walls of the inner barrel form an octagonal barrel with a quarter twist rifling pattern. The shell, shown in red in Figure 6.3, has a matching rifling pattern. To load the ARMRS, the user aligns the base of the shell with the barrel and presses the shell into the base of the inner barrel, thus arming the engagement system. When the Valkyrie system moves into engagement position, it electrically triggers the shell, and the payload leaves the barrel spinning like a round from a conventional firearm. This spin helps to disperse the shell contents to more effectively engage enemies. On the airframe side, a coating of sorbothane between the inner and outer barrels serves to absorb some of the initial recoil forces, while the inner barrel spins in the opposite direction of the projectile, bleeding off energy to friction, thereby absorbing the rotational recoil energy. Figure 6.4 on the next page show the ARMRS installed in the Valkyrie System.

The design of the ARMRS system allows the user to select what form of engagement is desired by changing the type of shell loaded. Possible loadings include commercial shell designs like birdshot or buckshot and the custom designed chain shots outlined above. As will be discussed later, several auxiliary missions are within the capabilities of the Valkyrie system, and in the case of these missions, the entire ARMRS can be replaced with a single large explosive charge of the same mass. Replacement of the ARMRS with an explosive charge does negate the reusable nature of the Valkyrie system and will limit the user base to military applications as the use of explosives will preclude civilian buyers.

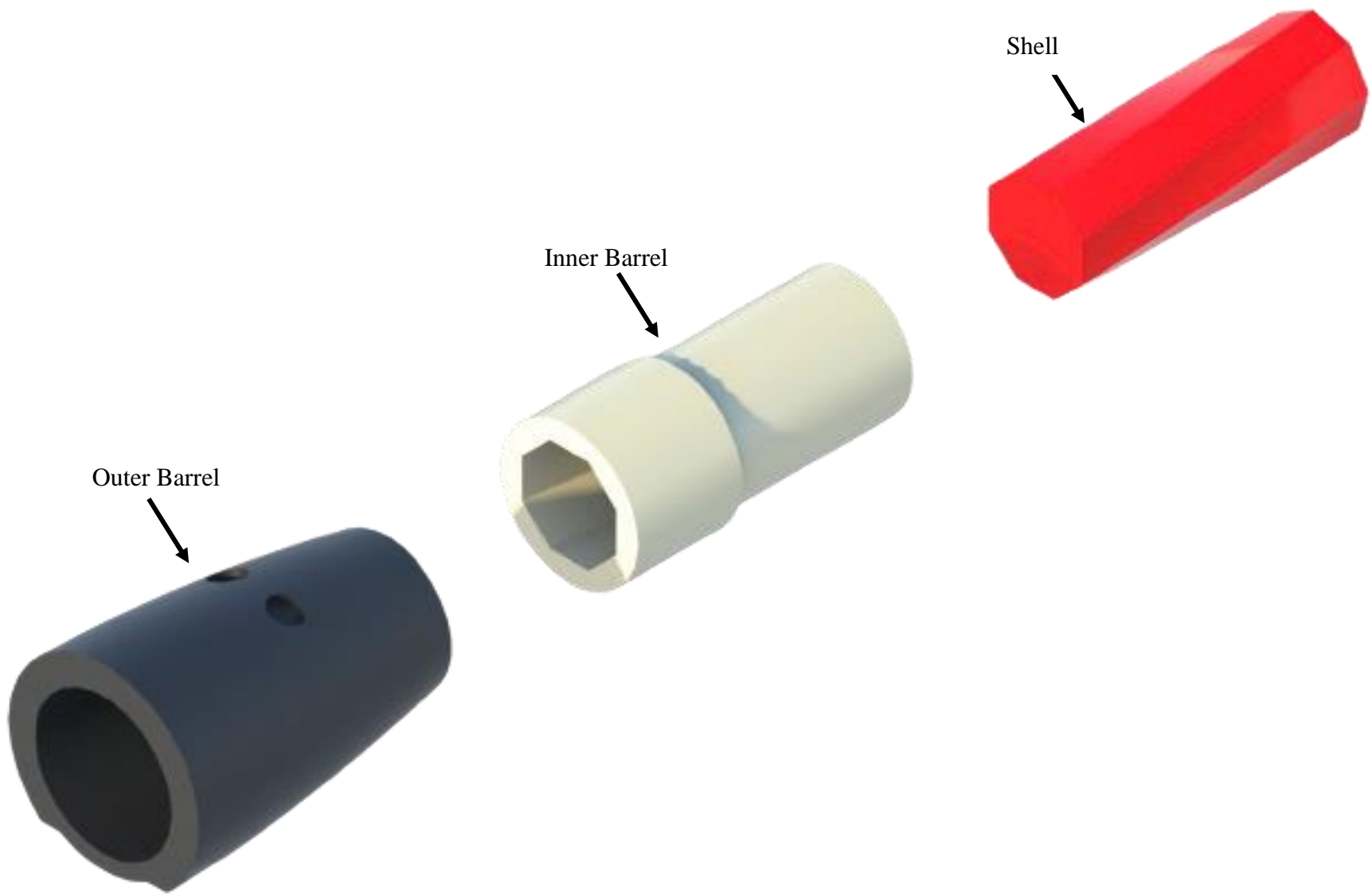


Figure 6.3 ARMRS Assembly Diagram

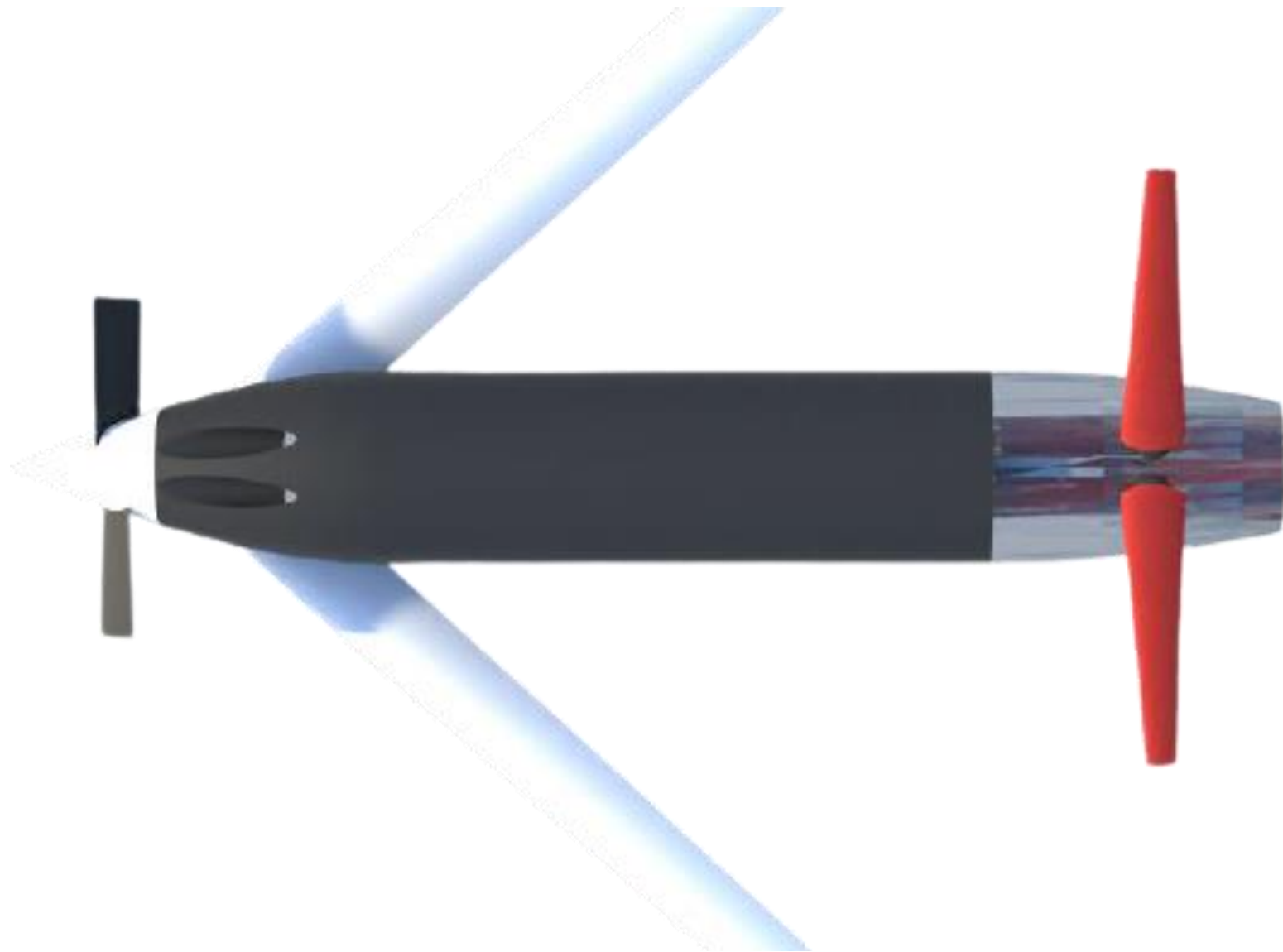


Figure 6.4 ARMRS Installed Onboard the Valkyrie System (rendered in clear polycarbonate to show shell detail)

7. WING, BATTERY, AND POWERPLANT SIZING

To start the sizing process, various approximations and values had to be determined through research. This includes mass density, wattage density, and power draw of electronics, as well as reasonable assumptions about what percent propulsion will constitute of the total system mass. The power and energy densities for our batteries were found using experimentally gathered data points in the 1998 DARPA MAV program as seen in Figure 7.1 below. Once these values are found, the motor, battery, and ESC volume and weight can be calculated using the equations seen below.

Because the avionics, wiring, and shotgun shell can easily meet the RFP's requirement of a safe storage life of 10 years or more, the batteries are the limiting factor for safe storage. This is partly why Lithium thionyl chloride and lithium iron sulfide batteries were specifically chosen to meet the RFP requirement of a safe storage life of 10 years [12].

Table 7.1: Sizing constants [11]

Term	Value
$\frac{W_{propulsion}}{W_{total}}$	0.38
$\frac{P}{W_{motor,ESC,prop}}$	3.37 W/g
$\frac{P}{W_{motor}}$	5.15 W/g
$\frac{P}{W_{Li-thynl\ chloride\ battery}}$	0.790 W/g
$\frac{P}{W_{Li-Fe\ sulfide\ battery}}$	2 W/g
$\frac{P}{W_{ESC}}$	34.3 W/g
Motor mass density	6 g/cc
Li-thionyl chloride battery mass density	2 g/cc
Li-Fe sulfide battery mass density	1946 g/cc
ESC mass density	3 g/cc

$$P_{systemshaft} = \frac{W_{propulsion}}{\frac{1}{\frac{P}{W_{motor,ESC,prop}}} + \frac{1}{\frac{P}{W_{battery}}}}$$

$$\frac{P}{V_{motor}} = \text{Motor Mass Density} \times \frac{P}{W_{motor}}$$

$$V_{Motor} = \frac{P_{systemshaft}}{\frac{P}{V_{motor}}}$$

$$W_{Motor} = \frac{P_{systemshaft}}{\frac{P}{W_{motor}}}$$

$$\frac{P}{V_{battery}} = \text{Battery Mass Density} \times \frac{P}{W_{battery}}$$

$$V_{battery} = \frac{P_{systemshaft}}{\frac{P}{V_{battery}}}$$

$$W_{battery} = \frac{P_{systemshaft}}{\frac{P}{W_{battery}}}$$

$$\frac{P}{V_{ESC}} = \text{ESC Mass Density} \times \frac{P}{W_{ESC}}$$

$$V_{ESC} = \frac{P_{systemshaft}}{\frac{P}{V_{ESC}}}$$

$$W_{ESC} = \frac{P_{systemshaft}}{\frac{P}{W_{battery}}}$$

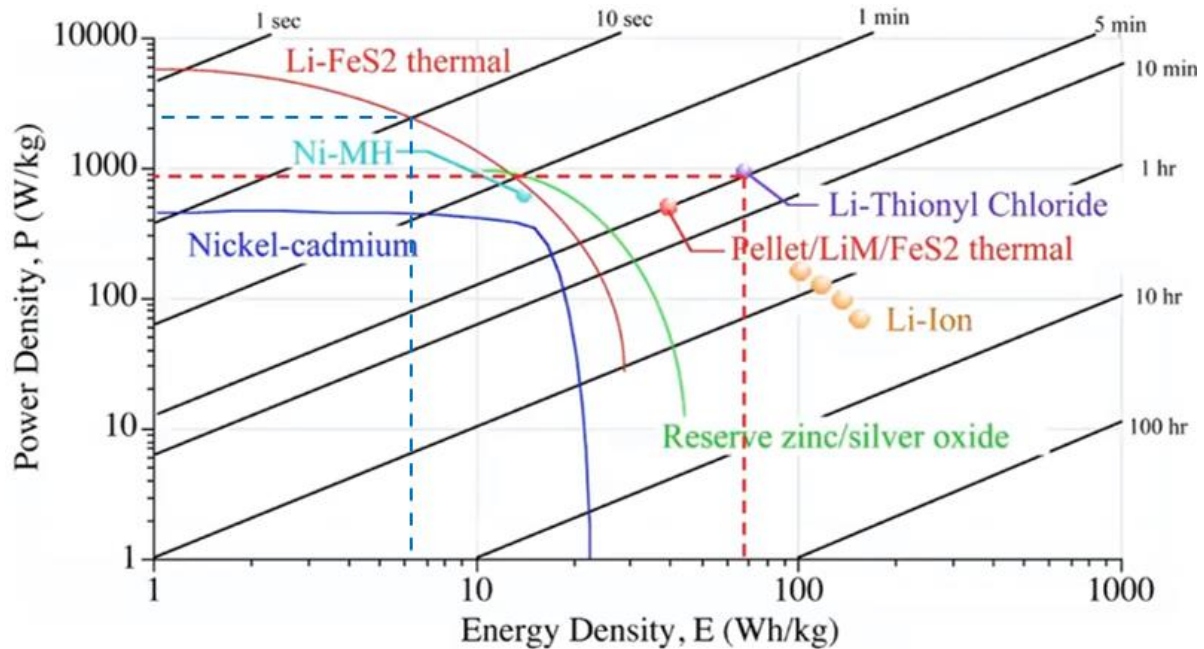


Figure 7.1: 1998 DARPA MAV Program Battery Densities [10]

Once these values are calculated, the fuselage size and wetted area must be calculated. To do this an estimation must be made for the avionics and mission package volume. From subject matter expert feedback and experimentation, the volume of a 12-gauge shotgun short-shell was chosen for the mission package.

$$V_{\text{fuselage}} = \Pi r^2 L$$

$$L = \frac{V_{\text{fuselage}}}{\Pi r^2}$$

$$S_{\text{wet}} = \Pi dL + 2\Pi r^2$$

Once the fuselage volume is determined, the form factor of the fuselage must be determined to find the fuselage wetted area. Standard gun barrel sizes were considered from a 410-gauge shotgun shell to a 40mm grenade. The closest standard barrel size that resulted with a fineness ratio of greater than 4 was a 10-gauge shotgun shell with a diameter of 0.775 in. With this diameter chosen, the fuselage wetted area can be calculated using the equation for a cylinder.

$$V_{\text{launch}} = \sqrt{\frac{2Eg}{W_{\text{launch}}}}$$

Eq. 1

$$C_L = \frac{2W}{\rho V^2 S}$$

Eq. 2

$$S_{\text{wing required}} = \sqrt{\frac{2W_{\text{launch}}}{\rho V^2 C_{L_{\text{max}}}}}$$

Eq. 3

To sweep through various configurations with respect to wing wetted area, a graph is made of the shaft power required with respect to wetted wing area. Then the total system shaft power available is graphed as a horizontal line and the wetted wing area required to avoid stall is graphed as a vertical line. Then the thrust required is calculated for various wing size configurations and Blade Element Momentum Theory (BEMT) is used to create a propeller that matches the thrust and power required for the configuration.

The graphs generated with the BEMT code are used to narrow the possible configurations of weight and form factors. The BEMT code functions by taking in

$$\theta_0(1) (rad) = \frac{6C_{Treq}(\sim)}{\sigma C_{la}(\frac{1}{rad})} - 0.75 * \theta_{tw}(rad) + \frac{3\sqrt{2}}{4} \sqrt{C_{Treq}(\sim)} \quad \text{Eq. 4}$$

inputs from the user and iterating through a series of equations, shown in Figure 7.2 at the right, at each user defined station along the length of the propeller blade.

$$\theta(rad) = \theta_0(rad) + R_n(\sim) * \theta_{Tw}(rad) \quad \text{Eq. 5}$$

Eq. 4 shows the first step of the code, which calculates the root twist of the propeller using inputs of

$$\lambda(r_n) (\sim) = \frac{\sigma(\sim) C_{la}(\frac{1}{rad})}{16 F(r_n)(\sim)} \left(\sqrt{1 + \frac{32 F(r_n) (\sim)}{\sigma(\sim) C_{la}(\frac{1}{rad})} \theta(r_n) (rad) r_n (\sim) - 1} \right) \quad \text{Eq. 6}$$

required thrust defined by the user. Eq. 5 shows the calculation of the next twist angle, using the twist rate and station of the propeller. Eq. 6 solves for the inflow ratio, which is then used in Eq. 7 to calculate the differential change in thrust coefficient. The differential thrust coefficients for each station along the propeller are then summed to find the total thrust coefficient for the propeller which is used in Eq. 8 to find

$$dC_T(\sim) = \frac{\sigma(\sim) * C_{la}(\frac{1}{rad})}{2} * (\theta_0(i) * (r(\sim))^2 - \lambda(\sim) r(\sim)) * dr(\sim) \quad \text{Eq. 7}$$

$$T(lbf) = C_T(\sim) * \rho \left(\frac{slugs}{ft^3} \right) * \pi(\sim) * R^2(ft^2) * V_{Tip}^2 \left(\frac{ft^2}{s^2} \right) \quad \text{Eq. 8}$$

Figure 7.2 BEMT Equations [13]

the thrust of the propeller. By manipulating the input values of characteristics for the propeller to meet the required thrust while remaining within the limits of the battery system, a final propeller configuration was designed for the aircraft.

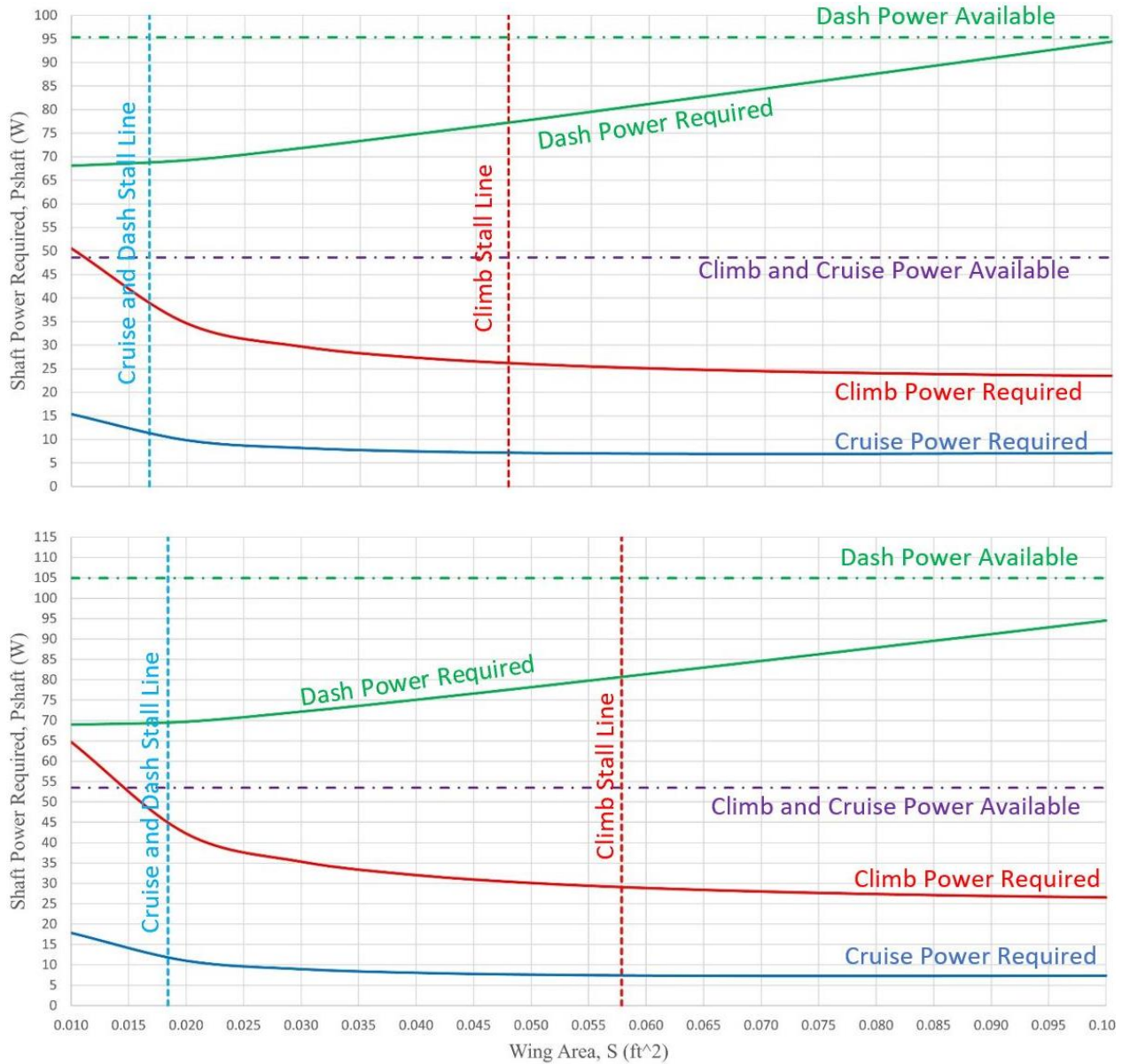


Figure 7.3 Power Required vs Wing Area For 200g (top) and 220g (bottom) Aircraft

The design point for the weight of the aircraft was set at half a pound to enable compliance with FAA regulations, as the desired availability in the police and civilian markets was likely to be compromised if the half pound threshold was breached. Converting to grams, the mass of the aircraft was set at 210.2, and

sizing of components was adjusted accordingly. Figure 7.4 below, with the design point marked with a yellow star, shows a graph similar to the center graph of Figure 7.3 on the previous page. In Figure 7.4 however, the percentage mass of the aircraft devoted to batteries has been reduced to the minimum allowable mass. This was accomplished by setting the power available equal to the power required at the design point wing area and solving for the mass percentage attributed to the batteries. This graph also takes into account the need for extra power in one in one million gust scenarios. According to Mil-F-8785B, at altitudes seen by the Valkyrie system this gust condition is 20 feet per second. This speed was added to the velocity parameter in the sizing chart prior to reducing the battery size, ensuring capabilities required to maintain flight.

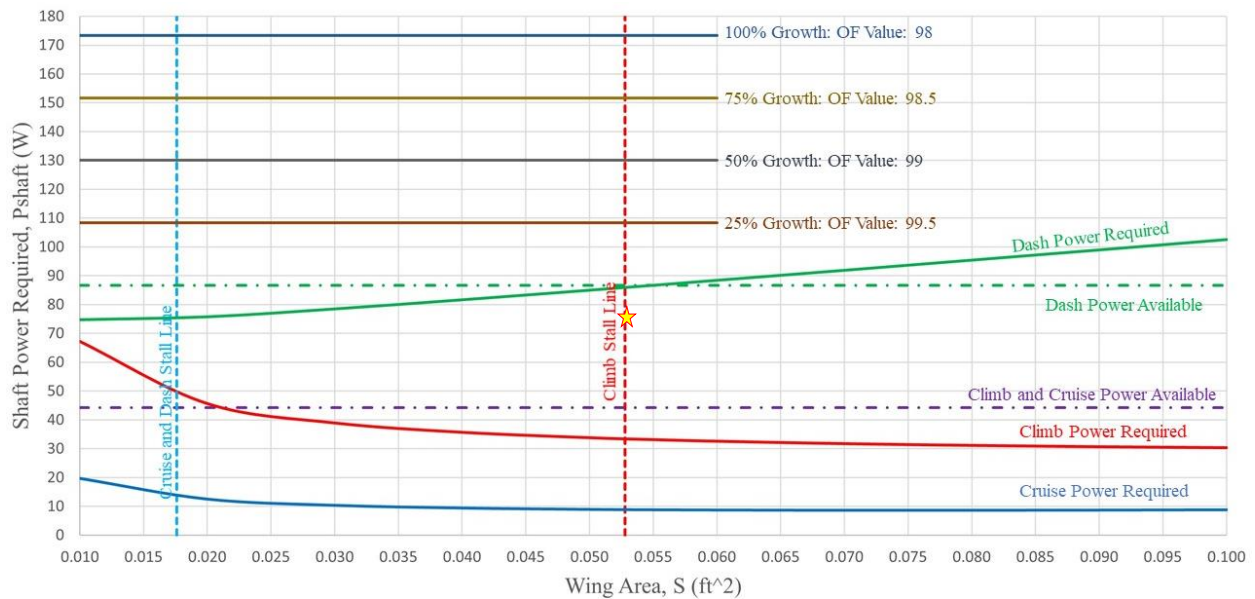


Figure 7.4 Sizing Chart for 210.2 g Aircraft Tuned Battery Size

Further refinement of the design was accomplished through development of a series of design point optimization isoclines showing

$$OF = 102 - \frac{2 * Power}{Power_{Baseline}}$$

the effect that oversizing the powerplant system has on the optimization function value of the design. Using the equation shown on the right, relative optimization scores of engine increases were evaluated and scored.

This chart illustrates the penalties associated with unnecessarily growing the powerplant sizing larger than what is required to operate.

8. CLASS I CONFIGURATION MATRIX AND DOWN SELECTION

The configuration and down selection performed in this section are based on methods described in Dr. Jan Roskam's Airplane Design Part II [14].

8.1. MAJOR IMPACTS ON DESIGN

Major impacts on design are determined by referring to the mission RFP [1] and objective function defined previously in Chapter 3 of this report:

- Objective range of 3.5 nmi
- Objective ceiling of 3,500 ft AGL
- Target dash speed of 250 ft/s
- Minimal weight of entire system
- $<2g$ acceleration at launch
- $<120\text{dBA}$ noise within 100 ft of launch
- Target Group 1 & 2 UAVs
- Interdiction rate of ≥ 10 UAVs/hour

8.2. CONCEPT OF OPERATIONS

The primary objective of the design is the ability to destroy or disable Group 1 and 2 UAVs while minimizing the system's cost, complexity, and weight as stated in the RFP [1]. The C-UAS will launch from a shoulder-held launcher and use an electric motor and propeller to climb to the objective ceiling of 3,500 ft AGL. It will use on-board systems to intercept the objective within 3.5 nmi, be capable of dash speeds of 250 ft/s, and perform endgame maneuvers. The system must be capable of detecting, acquiring, targeting, and engaging 10 UAVs per hour such that a C-UAS can be launched approximately every six minutes for an hour in a raid scenario. Depending on the power remaining after the mission, the system will have the ability to return to its base by normal flight and/or gliding without power.

8.3. CONFIGURATION AND DOWN SELECTION

Because the threat of small-UAVs is a relatively new concept, there are very few systems with similar profiles and performance specifications related to this design, so the configuration and down selection decisions are mostly based on satisfying the requirements in the RFP and the objective function in Section 3. Figure 8.8.3.1 below shows the configuration sweep with varying combinations of size, powerplant,

wing, and tail configurations. Table 8.8.3.1 lists advantages and disadvantages to each configuration and indicates if it satisfies the objective function.

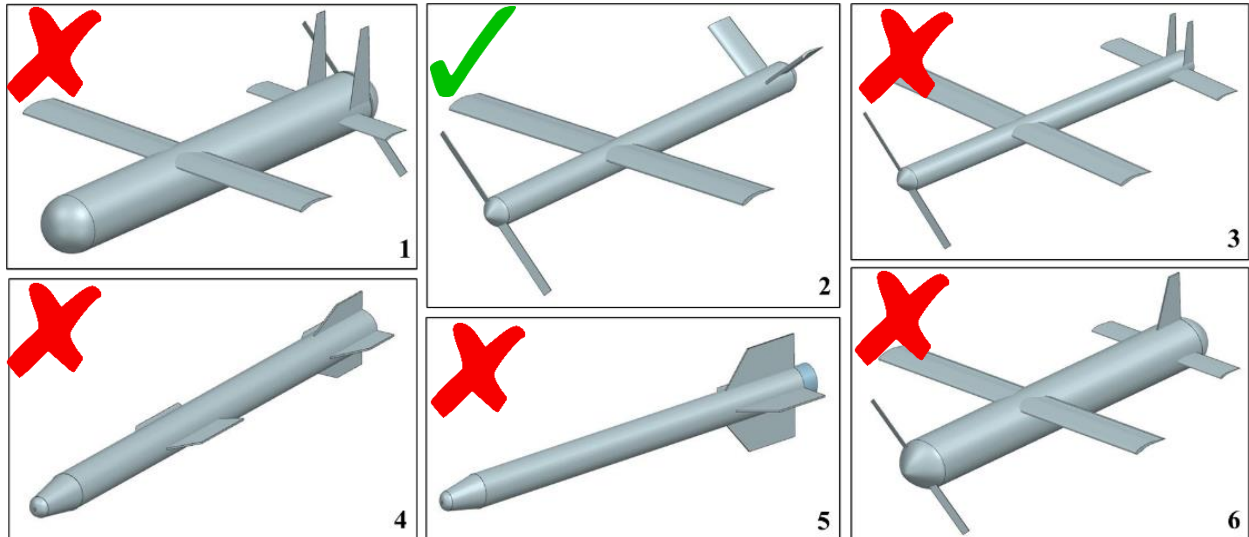


Figure 8.8.3.1 Configuration Sweep

Table 8.8.3.1 Configuration Down selection and Objective Function

Configuration	Advantages / Disadvantages	OF
1	Easy to control; Large payload volume / Large wetted area; High Drag	0
2	Lightweight; High velocity / Complex controls; Small payload volume	>0
3	Lightweight; High velocity; Easy to control / Small payload volume	>0
4	High velocity / Heavy; Expensive; Difficult CG control	0
5	High velocity / Heavy; Expensive; Difficult CG control; Lack of control surfaces	0
6	Easy to control; Large payload volume / Large wetted area; High drag	0

8.4 CONCLUSIONS

Although some aspects of the objective function are not able to be determined until later in the design process, the preliminary results show that smaller, lightweight, high-velocity systems are favored by the RFP requirements. Electric propulsion with modern power sources are capable of achieving high velocities needed to intercept UAVs. Between the two configurations with an objective function greater than zero, configuration 2 is chosen because of its simplicity in control surfaces.

9. CLASS II LAUNCHER, ENGAGEMENT, AND RECOVERY SYSTEMS

This section will detail the launch, engagement, and recovery systems for the Valkyrie system. Rough dimensions and weight sizing estimations are made for each component. The Valkyrie system will be launched from an M203 40-mm grenade launcher. The M203 is a lightweight and versatile weapon that allows for easy storage. It weighs roughly 5.6 lbs., has a length of about 29 in., and can include a folding stock for more compact storage. Together with the recovery net system (weighing approximately 14 lb), they can be stored in a single 20x12x8” backpack with extra room for missiles (Figure 9.1). As stated above in Chapter 7, the missile is designed to weigh just under 0.5 lb. Therefore, a single missile, net recovery system, and M203 launcher weight just over 20 lb meeting the RFP requirement of a launcher and a missile weighing under 40 lb. Adding a further 9 missiles only adds 4.5 lb bringing the total weight to a little less than 25 lb. Once again this meets the RFP requirement of a launcher and 10 missiles weighing less than 125 lb. Finally, this also meets the RFP requirement of a launcher and 10 missiles weighing less than 50 lb when distributed among 5 people as even if the total system and missiles are carried by a single person it does not exceed 50 lb. The M203 was also selected due to its high rate of fire, around 5-7 rounds a minute [15]. This rate of fire allows it to intercept 10 UAVs in two minutes in a raid scenario--far less time than the RFP’s hour time requirement. The figures below show the launcher relative to the size of a 90th percentile male human and 10th percentile human female.

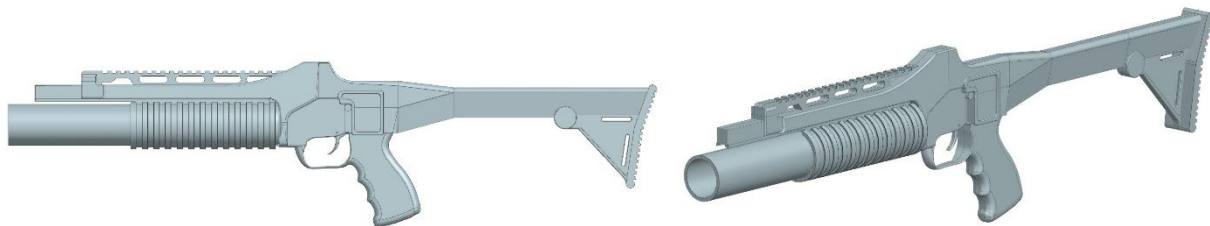


Figure 9.1 M203 Grenade Launcher



Figure 9.3 M203 Grenade Launcher with 90th Percentile Male 10th Percentile Female

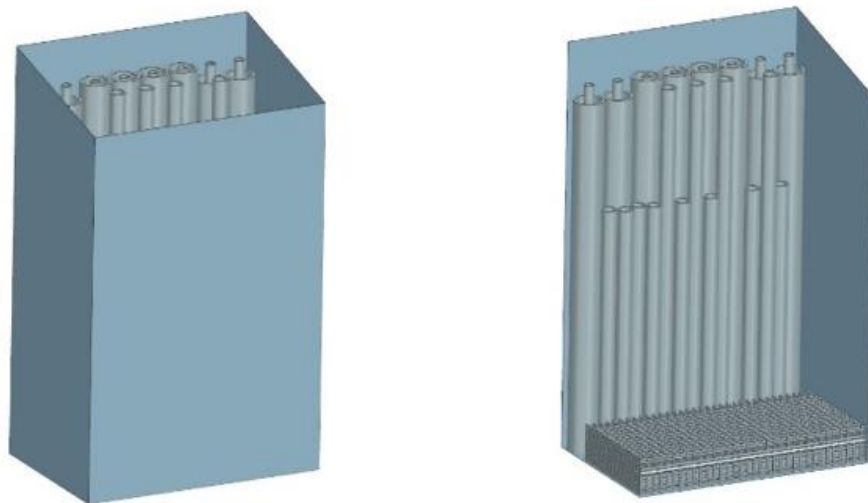


Figure 9.2 Compact Net Packing

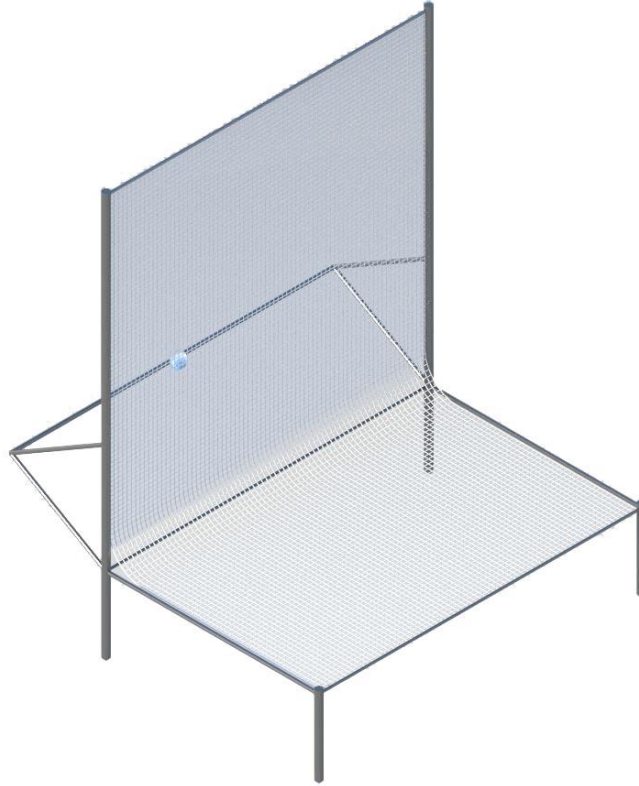


Figure 9.4 Net Capture System

Directly after launch, the wings will unfold, and the aircraft's propulsion and control system will take over the aircraft. The Valkyrie system is able to intercept a drone, perform endgame maneuvers if needed, and glide back to its base station where the lightweight net system will be able to capture the aircraft safely. This is discussed in further detail in the next chapter. The net system consists of an aluminum frame that is taken apart for storage and transportation, seen in Figure 9.4. It also utilizes an antenna mounted on the back side to communicate with the aircraft.

40 mm grenade launchers have been shown to have a maximum sound pressure level of 145 dB [16] at a distance of 1 ft away from the launcher. This has been proven to have little to no adverse effects on users especially considering that most users are wearing hearing protection when firing. However, if the desire is to mitigate the sound pressure level so as to meet the 120 dB requirement in the RFP a 4 in diameter and 12 in long silencer can be manufactured to mitigate the sound pressure level by 30 dB thereby lowering the

total sound pressure level to 115 dB and meeting the RFP requirement. The silencer would have internal rails running parallel to the barrel so as to make it compatible with the Valkyrie system sabot. This can be seen in Figure 9.5 below.



Figure 9.5 M203 with Silencer

Per US Army Medical Research and Mechanical Command, shoulder launched munitions may impart no more than 59 ft-lbs. of recoil energy to the shoulder of the soldiers using them [17]. Using the mass of an M203 grenade launcher [15] and the mass of an M-4 [18] as the standard deployment method, the acceleration due to recoil can be calculated using the equation below.

$$Energy = Mass * Acceleration * Distance$$

$$59ft * lbs = (0.0932 + 0.241)slugs * Acceleration * 1ft (M203 Barrel Length)$$

$$Acceleration = 176.75ft/s^2 = 5.49 Gs$$

Despite exceeding the allowable G limit spelled out in the RFP, the Valkyrie system is designed to be compliant with the recoil energy accepted by the United States Military. By adhering to this limit, the Valkyrie does comply with the requirement eliminate the possibility of injury to the user.

10. SENSOR, GUIDANCE, NAVIGATION, & COMMUNICATION SYSTEM DESIGN

The Valkyrie system is limited in both weight and space and therefore special consideration must be given to the sensor, guidance, navigation, and comms system design. Perhaps the most important aspect of this system is the identification and tracking of targets. To this end, the goal for the design of these systems is to achieve the most accurate and robust tracking and identification system possible while maintaining as little power draw and weight as possible.

To satisfy these requirements, a combination of four sensors are used: a magnetometer, a horizon sensor, acoustic vector sensors, and a navigational camera. Before the Valkyrie system is loaded into a 40mm grenade launcher (see Figure 10.6 below), it is given the initial launch location's GPS position. Once shot (see Figure 10.7), the Valkyrie system can be sent out in either a patrol pattern or in the known direction of a hostile UAS based on the initial location data uploaded to it as well as the on-board magnetometer and horizon sensors. The magnetometer maintains the direction of the Valkyrie system while the horizon sensor keeps it upright. As Valkyrie approaches an enemy UAS (see Figure 10.8), the acoustic vector sensors pick up on the sound of its propulsion system and are used to accurately guide to the enemy UAS position.

Acoustic vector sensors are made up of a pair of anemometer wires with a small amount of current running through them. Due to the current, they become slightly warm. This results in the temperature of the anemometer wire being directly proportional to the resistance of the wire; therefore, if the wire is cooled the temperature will decrease and so will the resistance. An acoustic wave will [cause particles in its path to shift](#). Coincidentally, this

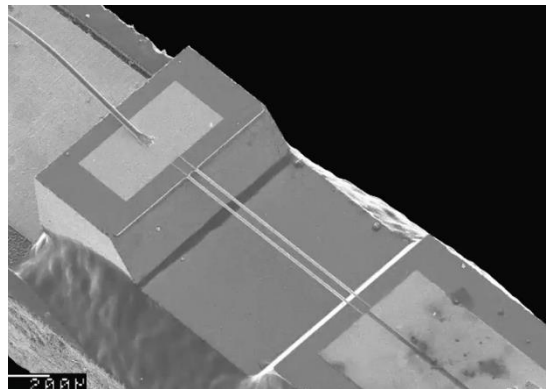


Figure 10.1: Pair of anemometer wires [19]

motion will cool anemometer wires that are in its path. Because of this, having two anemometer wires such as those seen in Figure 10.1 mean that if an acoustic wave is coming from the top right of the image, both



Figure 10.2: 3D acoustic vector sensor [19]

wires will be cooled, but the top right wire will be cooled slightly more than the bottom left wire by the particles effected by the acoustic wave and vice versa if the wind was coming from the bottom left. Knowing this, a pair of acoustic vector sensors like those shown in Figure 10.1 create a 1D acoustic vector sensor. Therefore, putting three pairs of anemometer wires in the X, Y, and Z axis creates a 3D acoustic vector sensor as seen in Figure 10.2. In addition,

having multiple 3D acoustic vector sensors at a set distance apart from each other allows for an accurate, real time tracking of aircraft. This was proven in a [Microflown AVS test by Hans-Elias de Bree](#) where a helicopter was flown between two acoustic vector probes set a distance apart and it was shown that the acoustic vector sensors could accurately predict the 3D location of the helicopter during flight (see Figure 10.3 below).

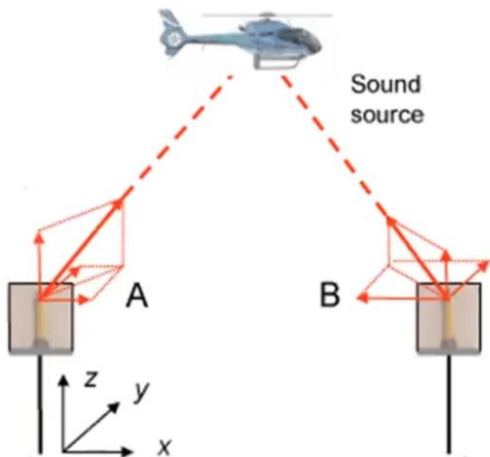


Figure 10.3: [Hans-Elias de Bree's Helicopter Test](#) [19]

Valkyrie's acoustic vector sensors are set a fixed distance apart similar to the Microflown test by placing an acoustic vector sensor on each wing tip (see Figure 10.16). The Valkyrie system does not have the onboard capacity to interpret the acoustic vector sensor data itself due to weight and size limitations. However, it can easily send the data back to the ground station and have the computer analyze the data and transmit it back to the UAS. Because a ground station is already required for manual pilot control, this adds little to no cost.

Finally, after Valkyrie is guided to an enemy UAS by the acoustic vector sensors, the pilot can visually confirm the presence of a hostile UAS and tell Valkyrie to engage. This allows the pilot to call off the strike in the event of accidental targeting of friendlies or non-combatants. Once this is done, the autopilot takes over, pulling directly ahead of the enemy UAS and executing endgame maneuvers at a faster rate than any human pilot could (see Figure 10.9). After Valkyrie is in front of the enemy UAS, it uses a charged capacitor to release a small cloth wing section required for climb as well as the tail cone in preparation to use the ARMRS system discussed in Chapter 6 (see Figure 10.10). With the tail cone removed and the hexagonal shot exposed, Valkyrie lines up the shot and fires Kevlar strands, shot, or various other loads at the hostile UAS, successfully disabling the hostile system (see Figure 10.11). After the engagement, a small amount of power is left in the lithium iron sulfide battery to keep the navigation and control powered, but not the propulsion system. However, the aircraft is more than capable of gliding over 15,000 ft at an L/D of 32 and a speed of 57 knots at the engagement altitude of 5000ft. Once again, the magnetometer and horizon sensors are used to guide the aircraft back to base. Once the aircraft gets close enough, the acoustic vector sensors pick up on the non-audible sound emitted from the ground station and guide the aircraft safely into the net (see Figure 10.12) where it can be recovered and brought back to base to be reloaded for a future engagement (see Figure 10.19).

In addition to its role as an anti-UAV missile system, the Valkyrie system can be used in an anti-sniper or artillery role. In these cases, the ARMRS section would be removed and replaced with an explosive

charge as discussed in Chapter 6, thus making the engagement a one-way trip. However, this allows for a much wider range of applications, opening the system to a larger range of audiences and lowering the overall cost. These operations would start very similar to that of the anti-UAV operation discussed above except that the acoustic vector sensors would lock onto the barrel noise of a sniper or artillery position (see Figure 10.13 and 10.14) instead of the engine noise of a hostile UAS. [Another test by Hans-Elias De Bree](#) showed this exact use of acoustic vector sensors with great success as seen in Figure 10.4 below.



Figure 10.4: [Hans-Elias De Bree's Gunshot Test](#) [19]

Analysis of the total sensor, guidance, navigation, and control system can be seen below in Figure 10.5. The total power draw (Table 10.1) was analyzed using gathered data from online retailers for electrical components similar to those that would be used on the Valkyrie system.

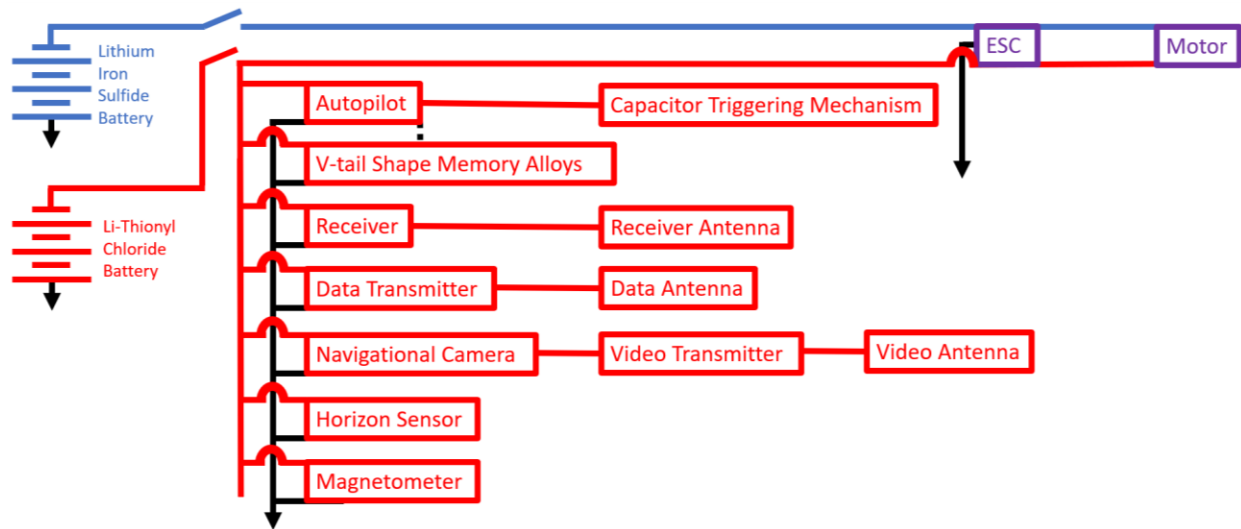


Figure 10.5: Sensor, Guidance, and Communication System Design

Table 10.1: Sensor, Guidance, and Communication System Power Draw

Electrical Load Item	T/O Climb (13 seconds)	Cruise (125 seconds)	Intercept (10 seconds)	Return (84 seconds)
ESC	26 kJ	252 kJ	20 kJ	0 J
Motor	22 kJ	220 kJ	18 kJ	0 J
Autopilot and Magnetometer	33 J	313 J	25 J	210 J
Receiver and Antenna	5 J	50 J	4 J	34 J
Data Transmitter and Antenna	13 J	125 J	10 J	84 J
Navigational Camera	10 J	100 J	8 J	67 J
Video Transmitter and Antenna	10 J	25 J	2 J	17 J
Totals	48 kJ	472 kJ	38 kJ	412 J

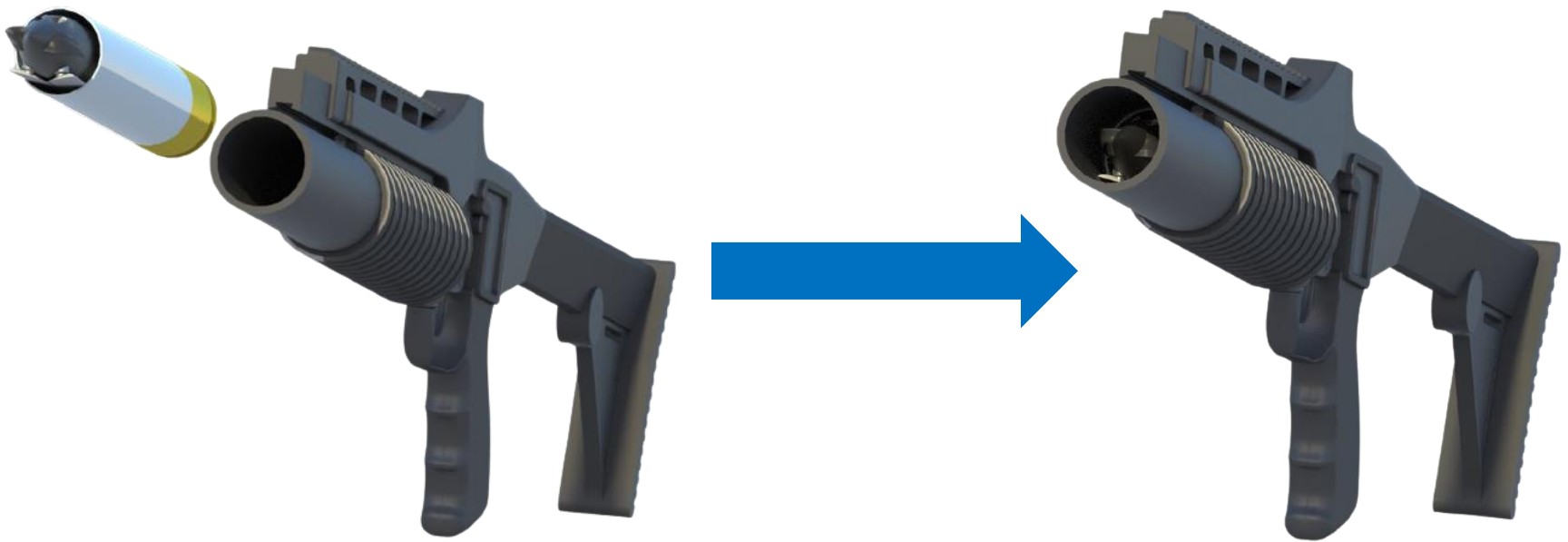


Figure 10.6: Valkyrie Loading

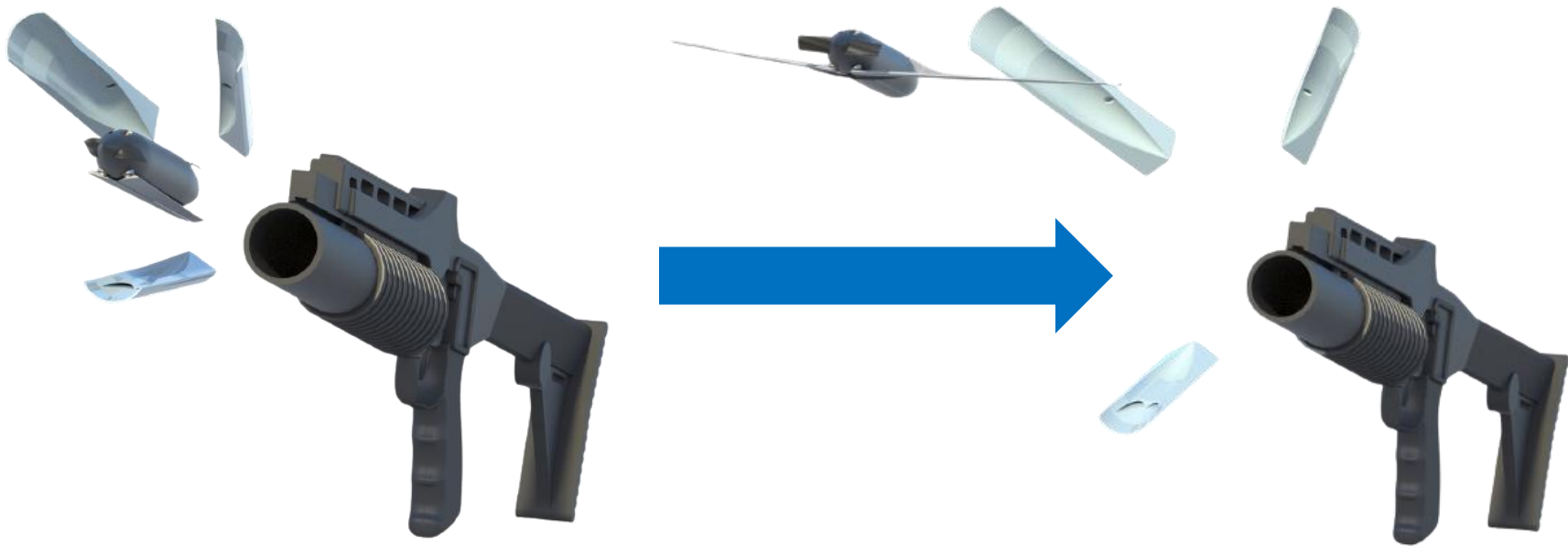


Figure 10.7: M203 Firing the Valkyrie System

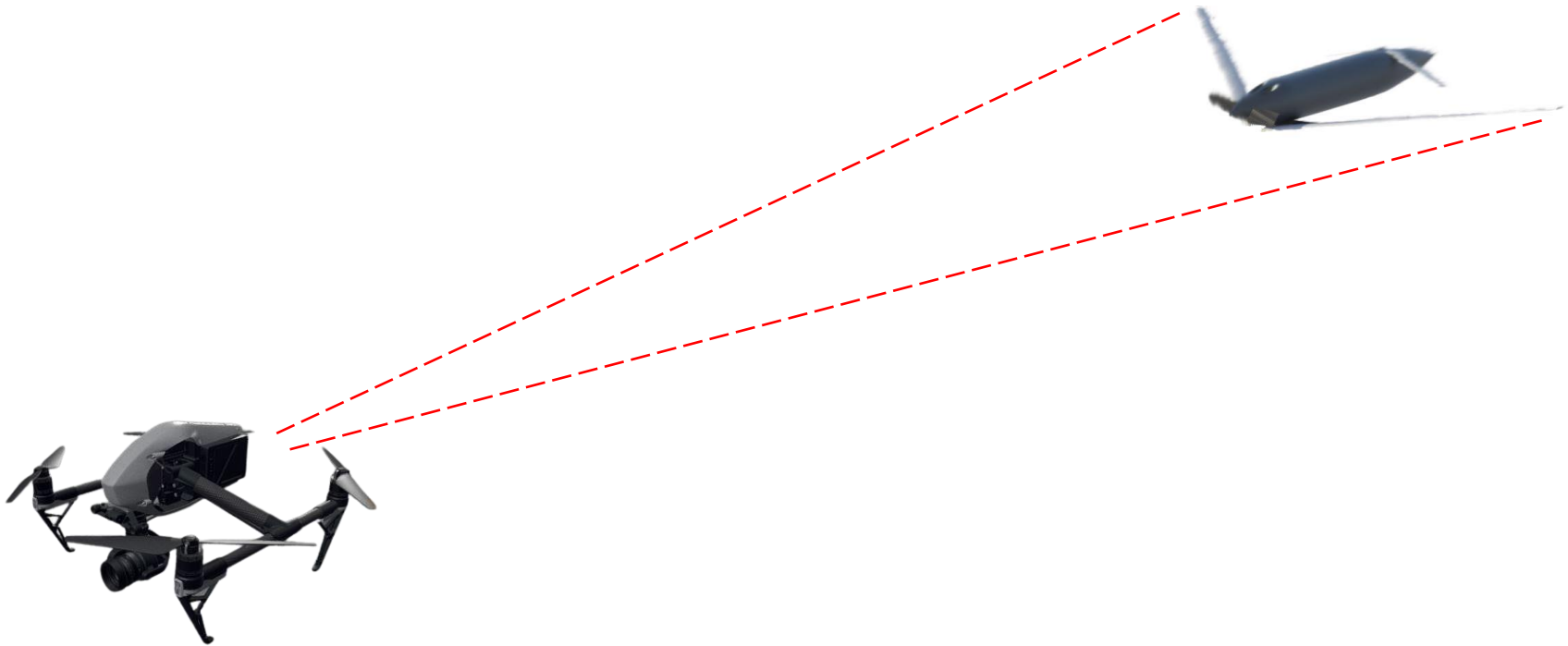


Figure 10.8: Valkyrie Cruise and Acoustic Vector Sensor Lock-on of Hostile UAS

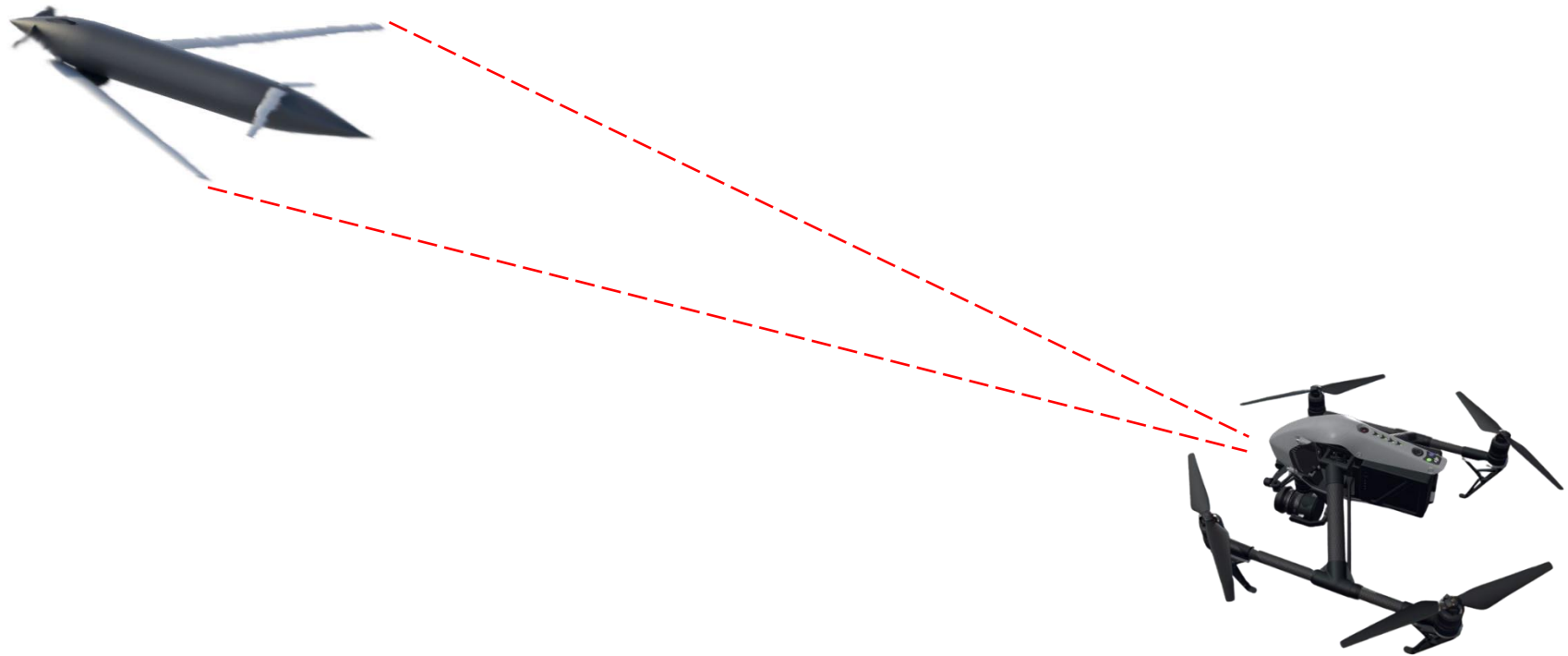


Figure 10.9: Valkyrie Pulls Ahead of Hostile UAS



Figure 10.10: Valkyrie Discards Tail Cone and Cloth Wing

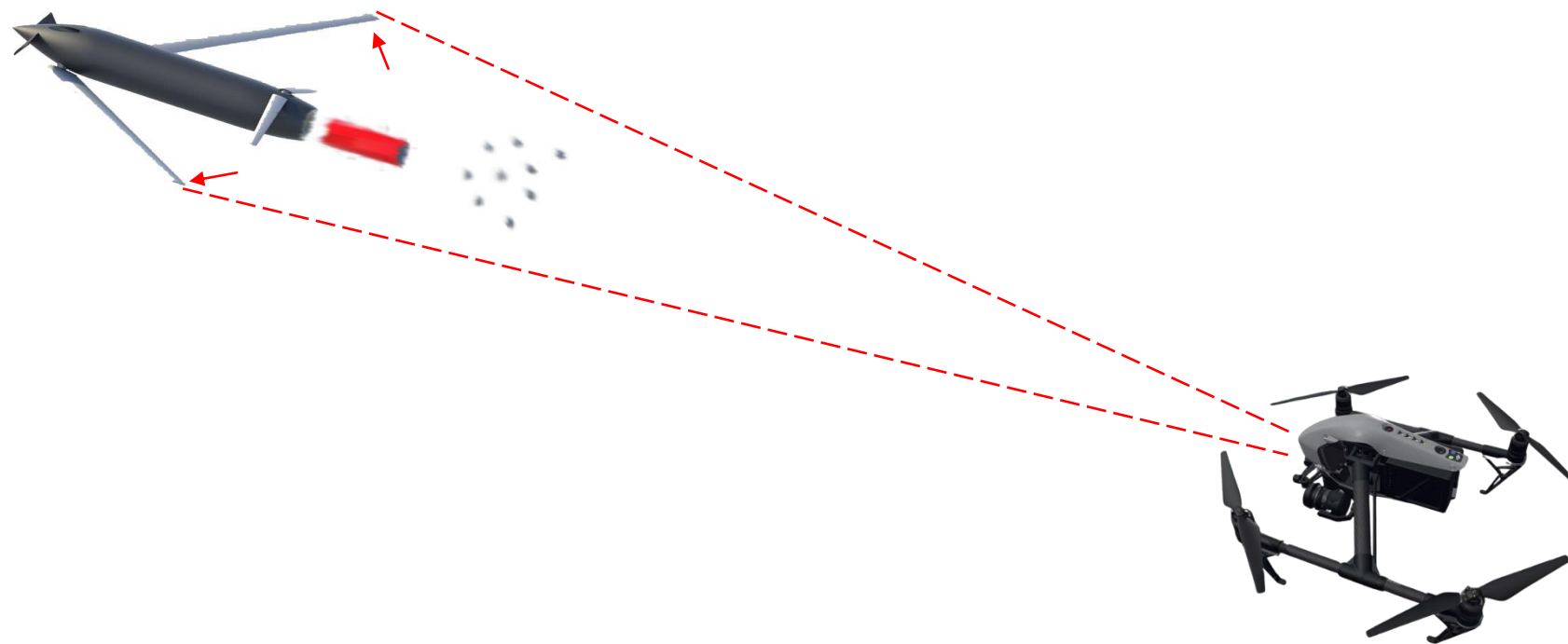


Figure 10.11: Valkyrie ARMRS System Engagement of UAS and Simultaneous Forward Wing Shift

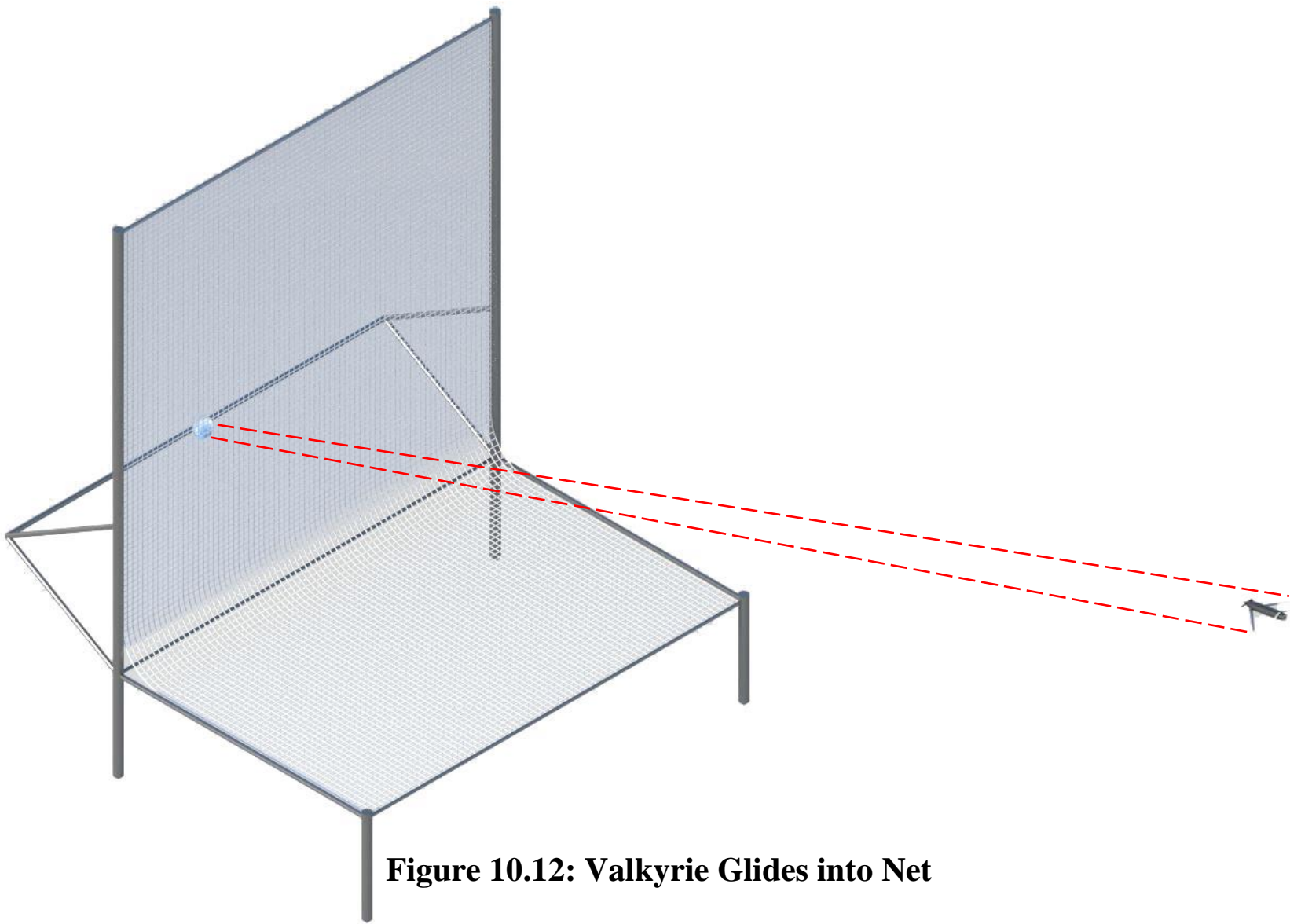


Figure 10.12: Valkyrie Glides into Net

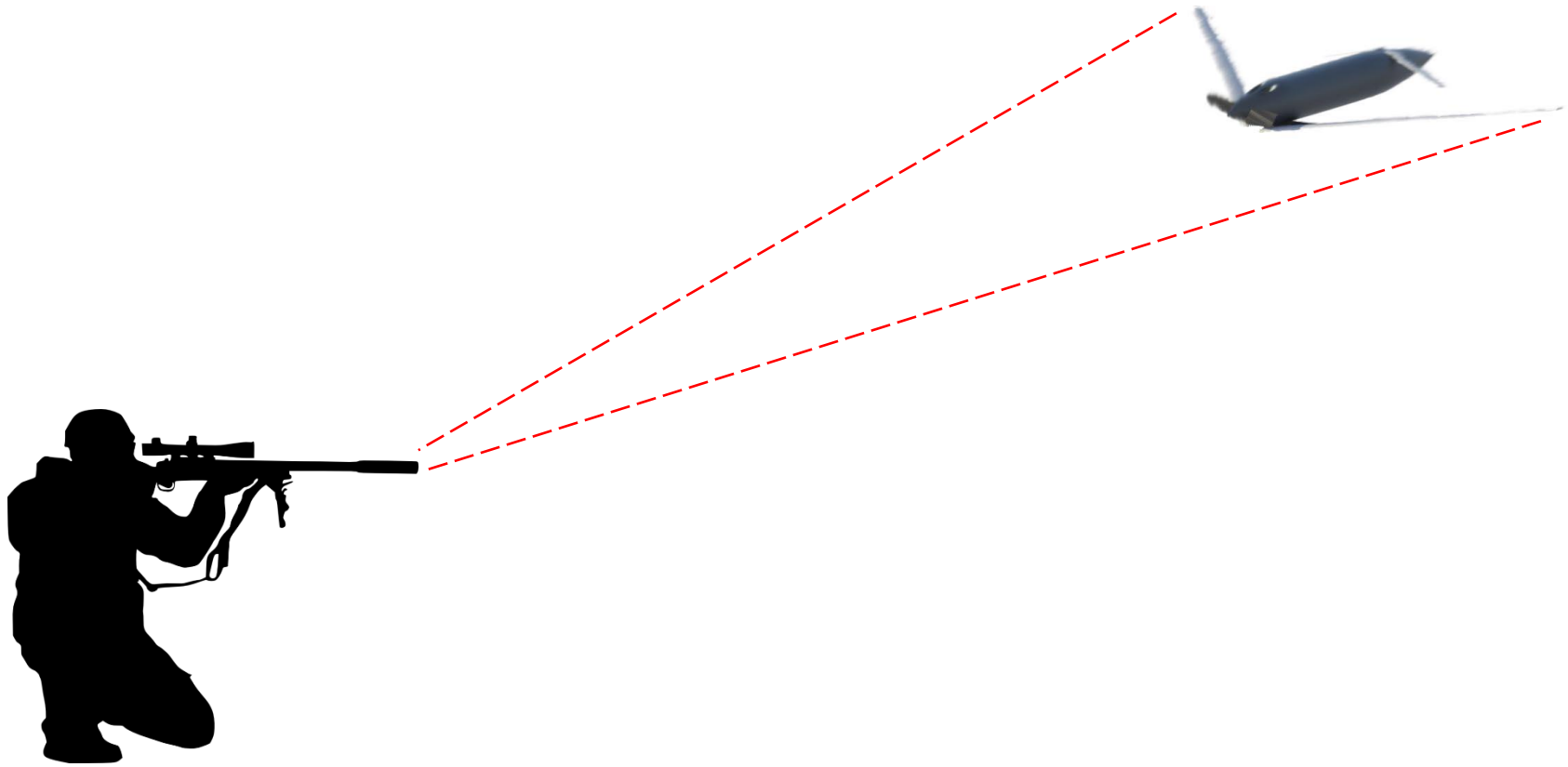


Figure 10.13: Valkyrie Acoustic Vector Sensor Lock-on of Enemy Sniper

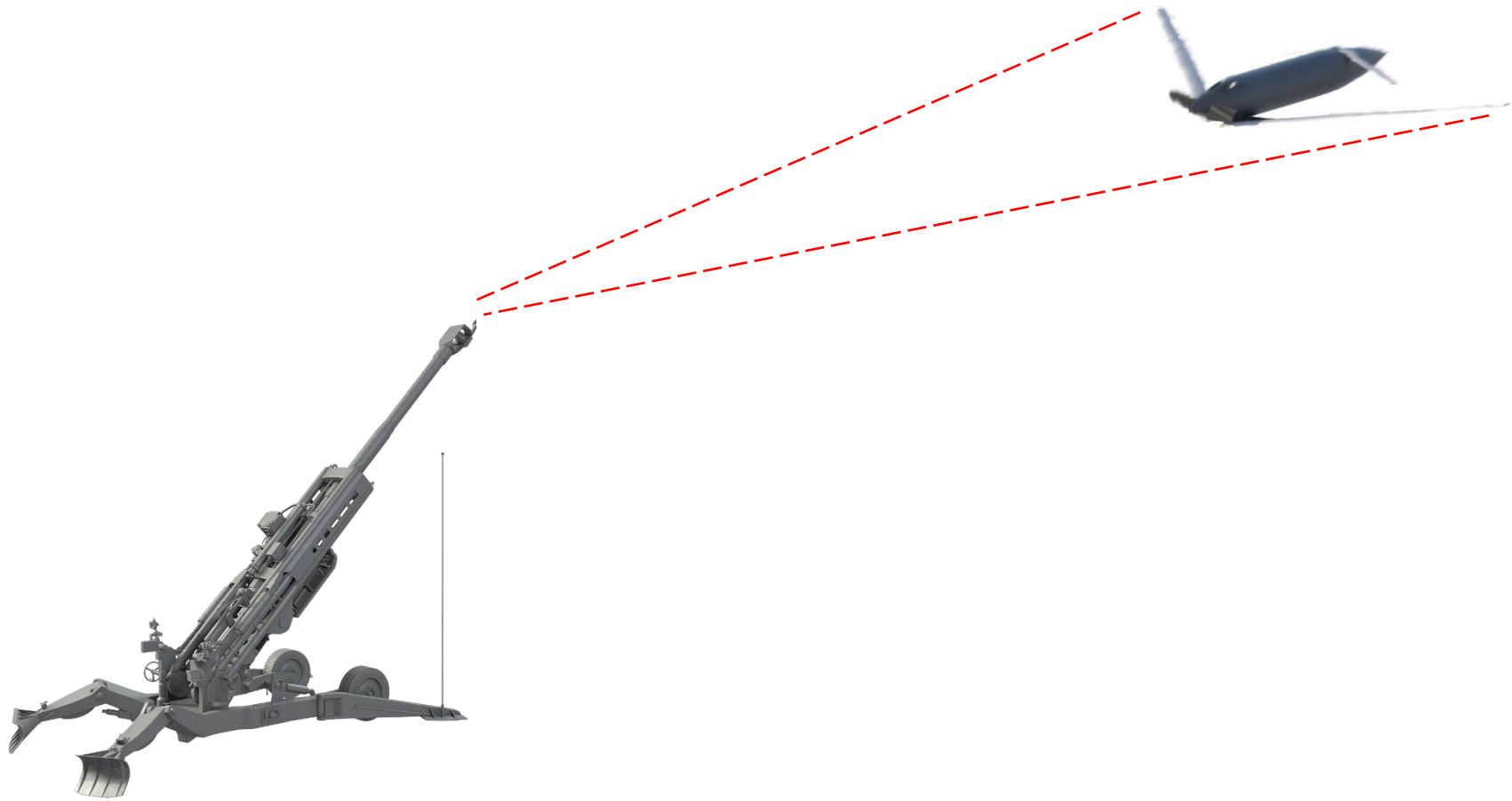


Figure 10.14: Valkyrie Acoustic Vector Sensor Lock-on of Enemy Artillery

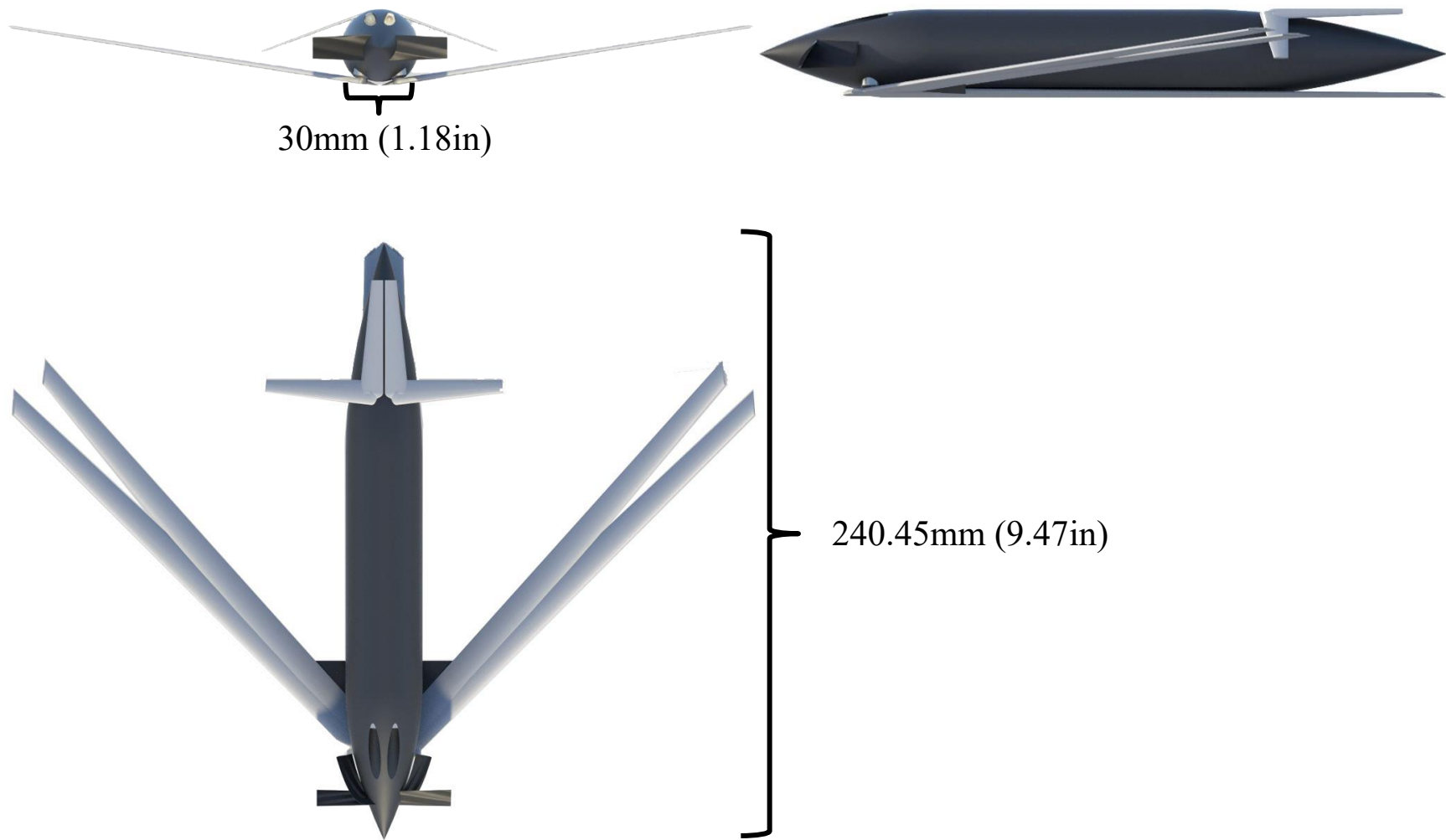


Figure 10.15: Valkyrie 3-view with Folded, Cruise, and Glide Configurations Shown

Table 10.2: Valkyrie Characteristics

Characteristic	Wing	V-Tail
Area	5130 mm ²	668 mm ² 624 mm ² (Effective Horizontal Tail) 237 mm ² (Effective Vertical Tail)
Span	282 mm (climb/cruise) 304 mm (glide)	90 mm
MGC	19 mm	7.7 mm
AR	16 (climb/cruise) 18 (glide)	12
Sweep Angle	42.75° (climb/cruise) 37.75° (glide)	0°
Taper Ratio	0.5	0.5
Thickness Ratio	11.72%	11.72%
Airfoil	Clark Y	Clark Y
Dihedral Angle	28.5°	-20°
Incidence Angle	0°	0°
Total Length	240 mm (9.45 in)	
Fuselage Diameter	30 mm (1.57 in)	

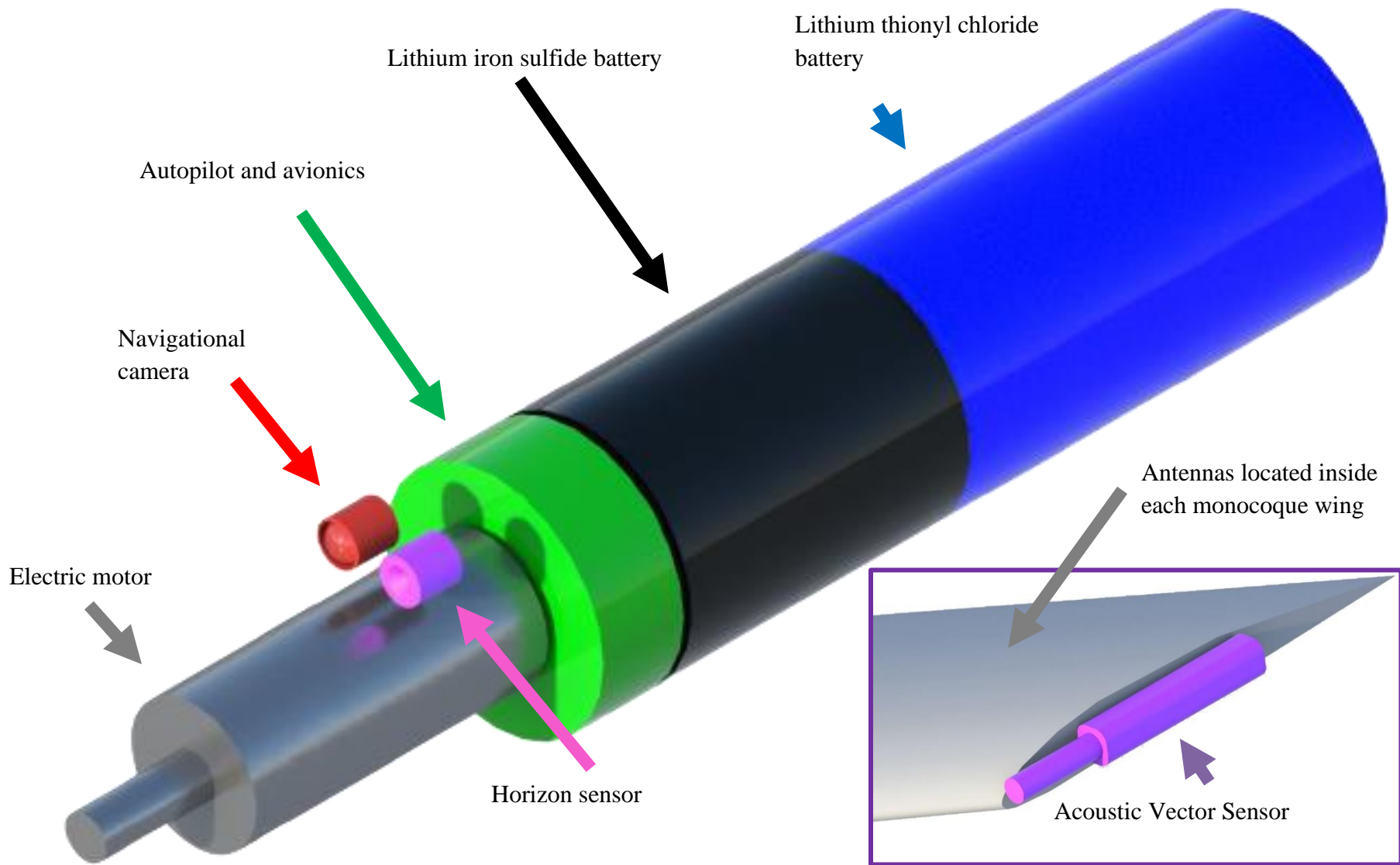


Figure 10.16: Valkyrie Electronics

Internal structure made from PEEK to withstand shock of launch and ARMRS engagement

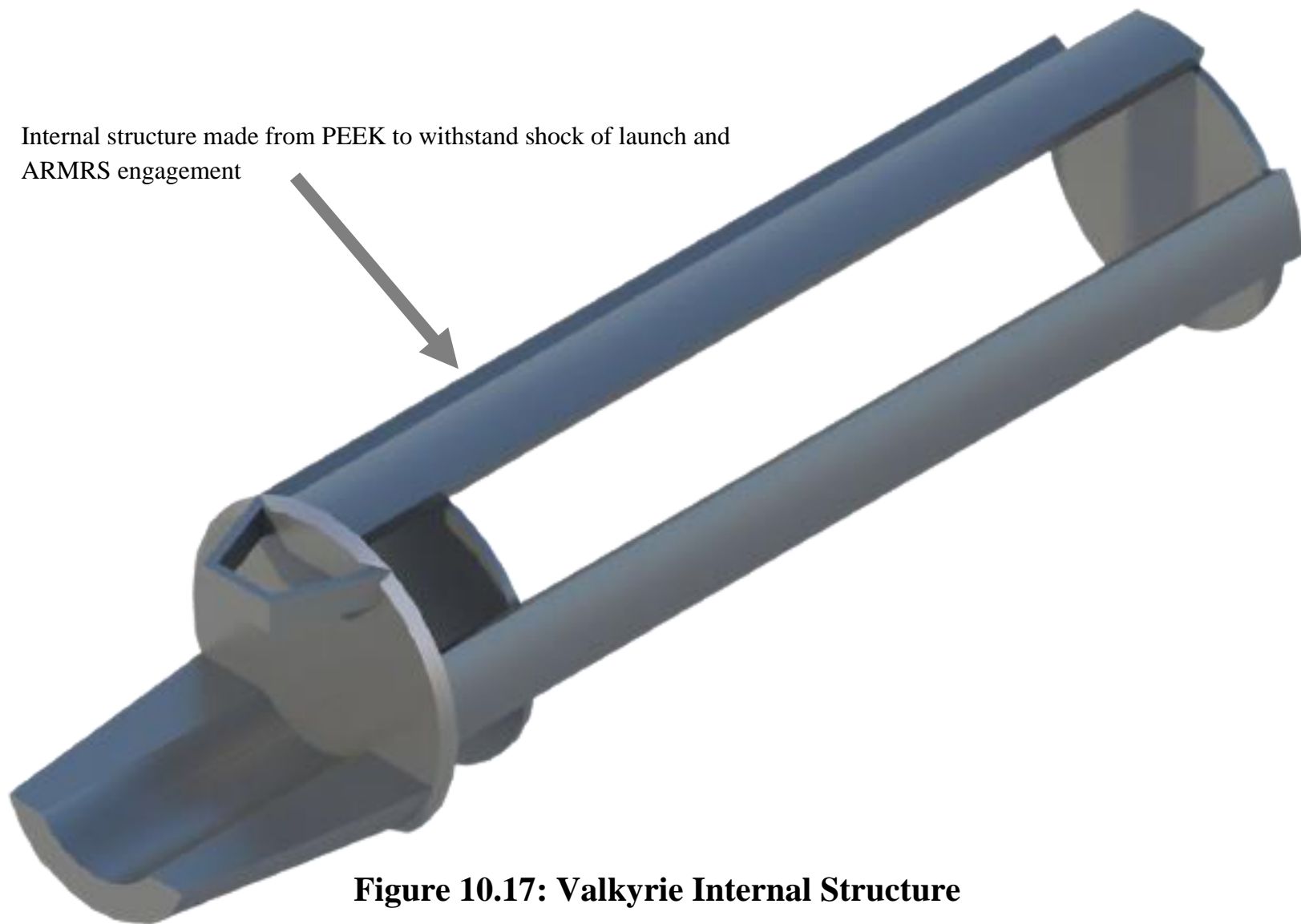


Figure 10.17: Valkyrie Internal Structure

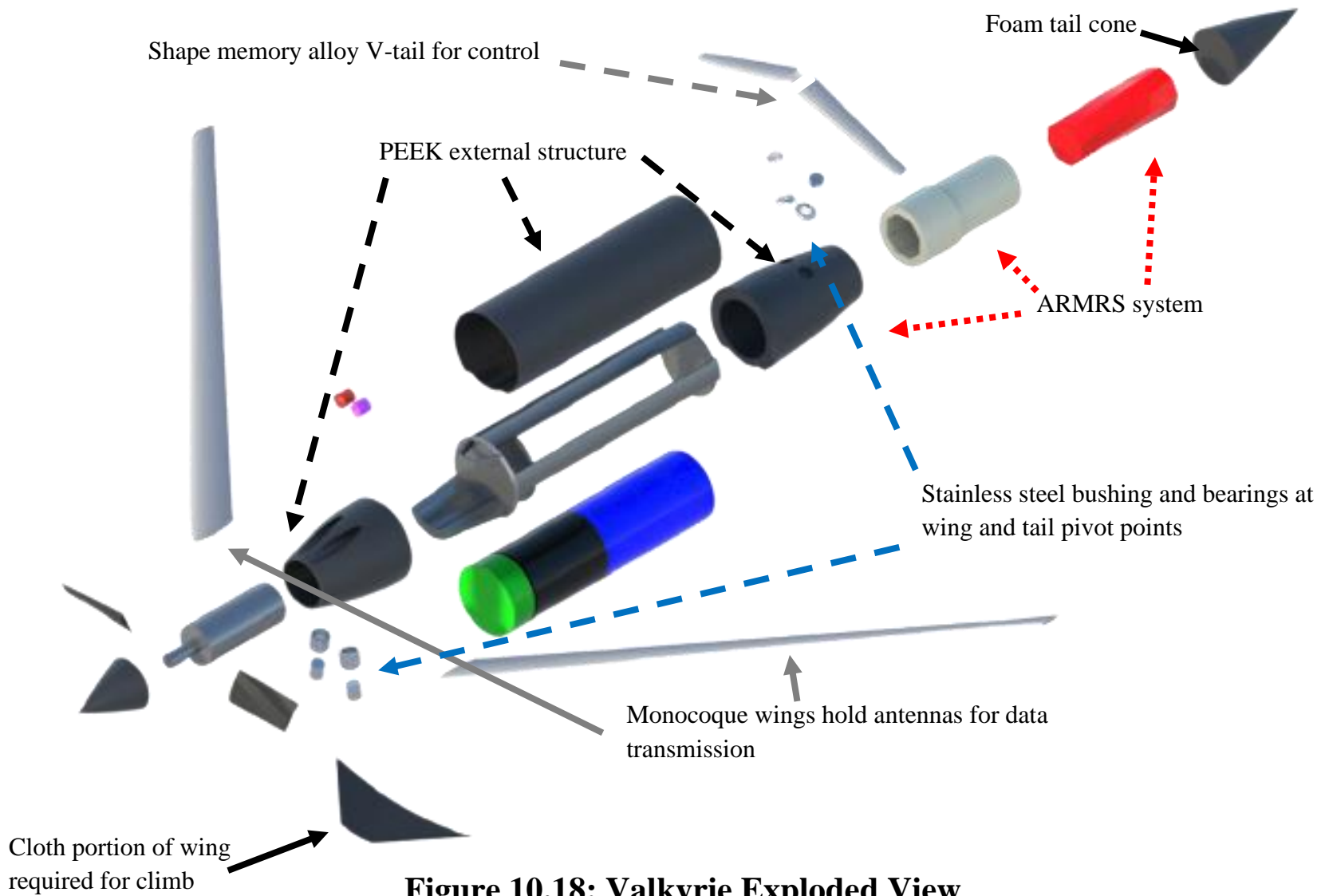


Figure 10.18: Valkyrie Exploded View

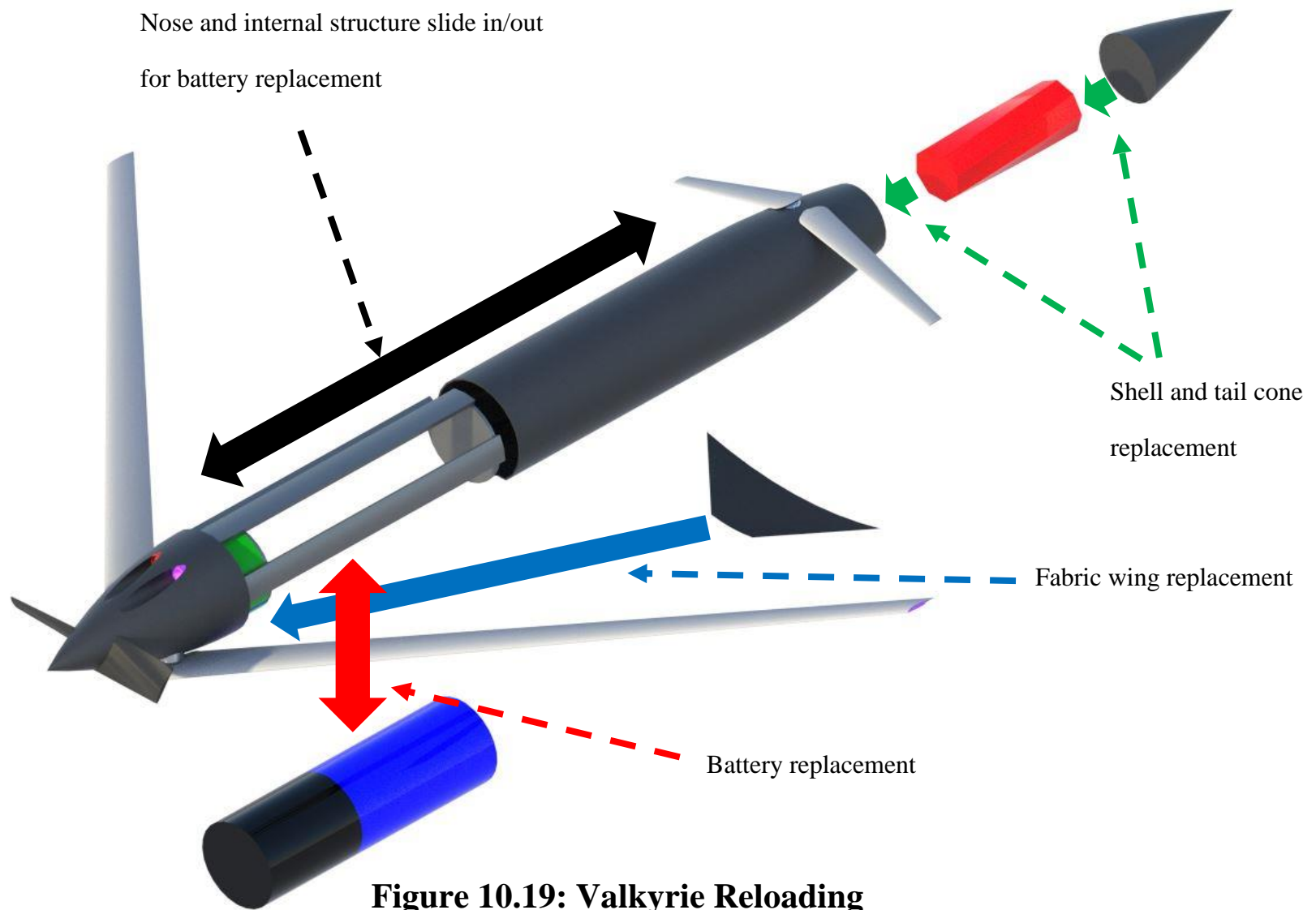


Figure 10.19: Valkyrie Reloading

As stated above, Valkyrie is able to navigate autonomously using its onboard receivers but requires constant communication between itself and the ground station to interpret the acoustic vector sensor data, to send telemetry data, and for optional RC control. An omnidirectional half-wave dipole antenna is used on the air unit and a directional patch antenna on the ground unit. Ansys HFSS [20] is used to design and analyze this antenna configuration to ensure the 3.5nmi design requirement of the aircraft is also achieved with the communications.

Valkyrie is fitted with a dipole antenna inside each wing operating at a resonant frequency of 2.4GHz. The omnidirectional radiation pattern allows for the signal to be transmitted in a donut shape along the plane of the ground. The length of the dipole antenna is estimated to be 62.5mm, determined by the following equations:

$$L = \frac{150}{f}$$

Where:

L = Total length of diople (meters)

f = frequency (MHz)

The initial design is created in HFSS and shown in Figure 10.20. The antenna resonates slightly below 2.4GHz as shown in Figure 10.21, so a design sweep is used to incrementally adjust the antenna length until the proper tuning is reached, shown in Figure 10.22.

Realized gain is a major contributor in determining transmission strength and range. Figure 10.23 shows a polar plot for realized gain of the antenna, where at 360 degrees it has a gain of 2.31dB. Figure 10.24 shows a downscaled 3D radiation pattern and its orientation with respect to the dipole. The darkest red represents the highest gain output and would point horizontally to the ground plane.

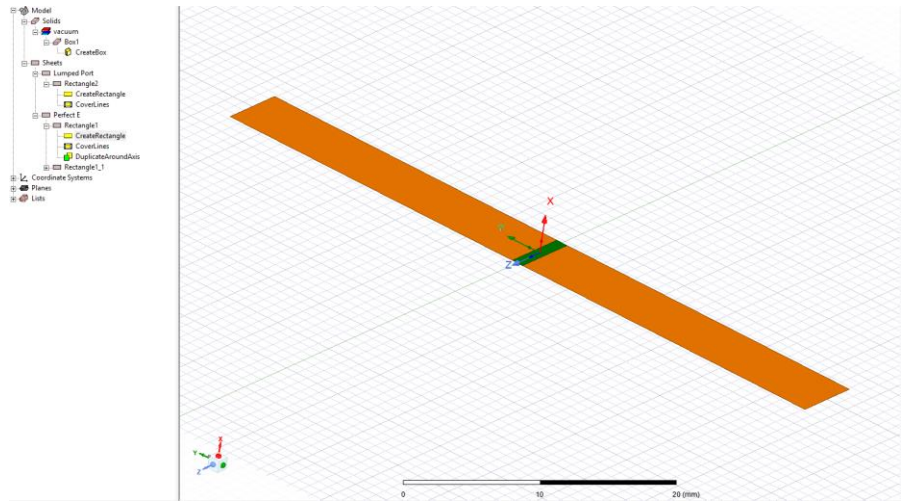


Figure 10.20: Dipole Antenna in HFSS

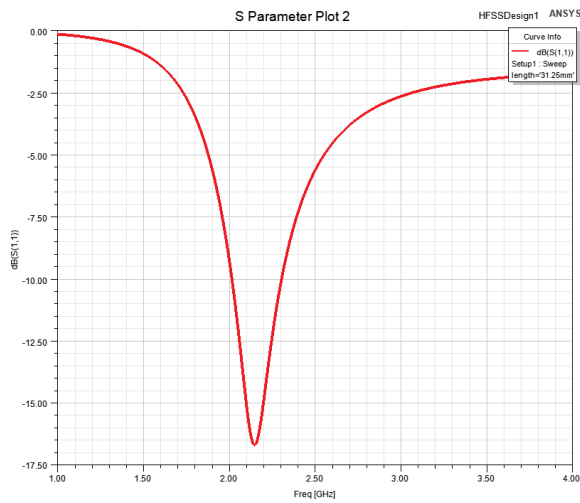


Figure 10.21: Dipole Return Loss and Resonant Frequency before Tuning

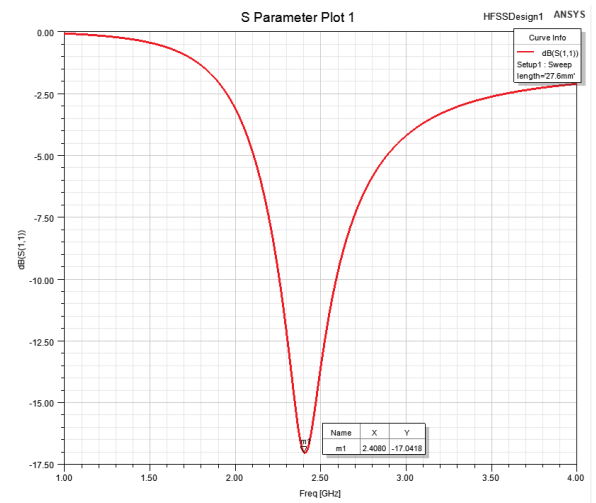


Figure 10.22: Dipole Return Loss and Resonant after Tuning

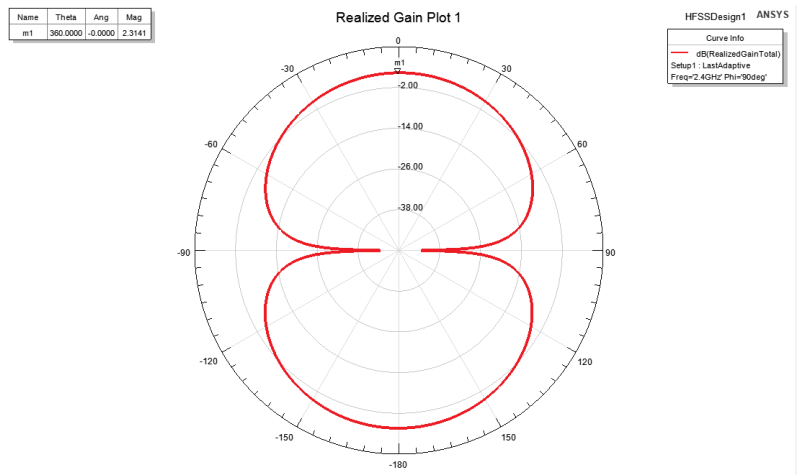


Figure 10.23: Dipole Realized Gain Polar Plot

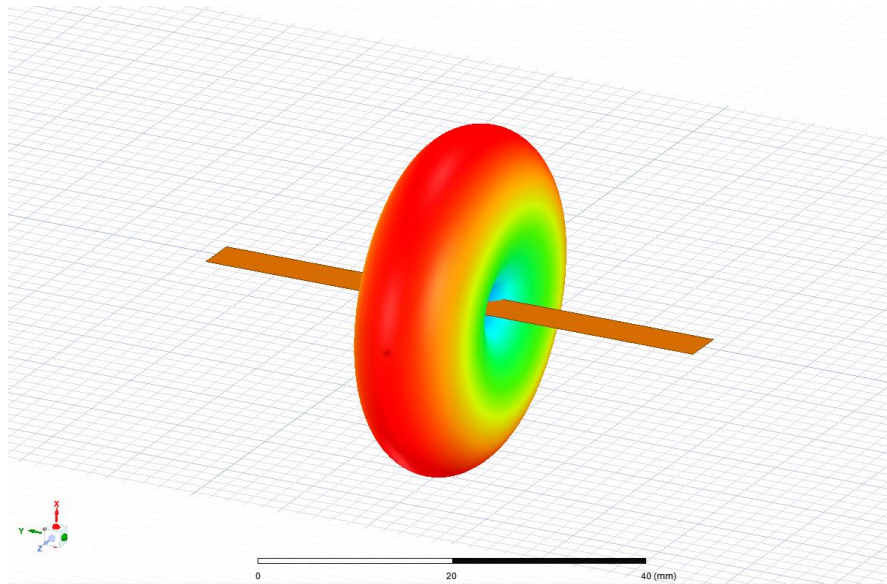


Figure 10.24: Dipole Radiation Pattern

The directional patch antenna is used for the ground station. Directional antennas provide greater directivity and smaller beamwidths, resulting in higher gains in the direction it is pointing. Patch antennas are slightly more complicated designs. The system contains the copper patch antenna with an RF4-epoxy substrate, copper ground plane, and the feed and port, shown in Figure 10.25.

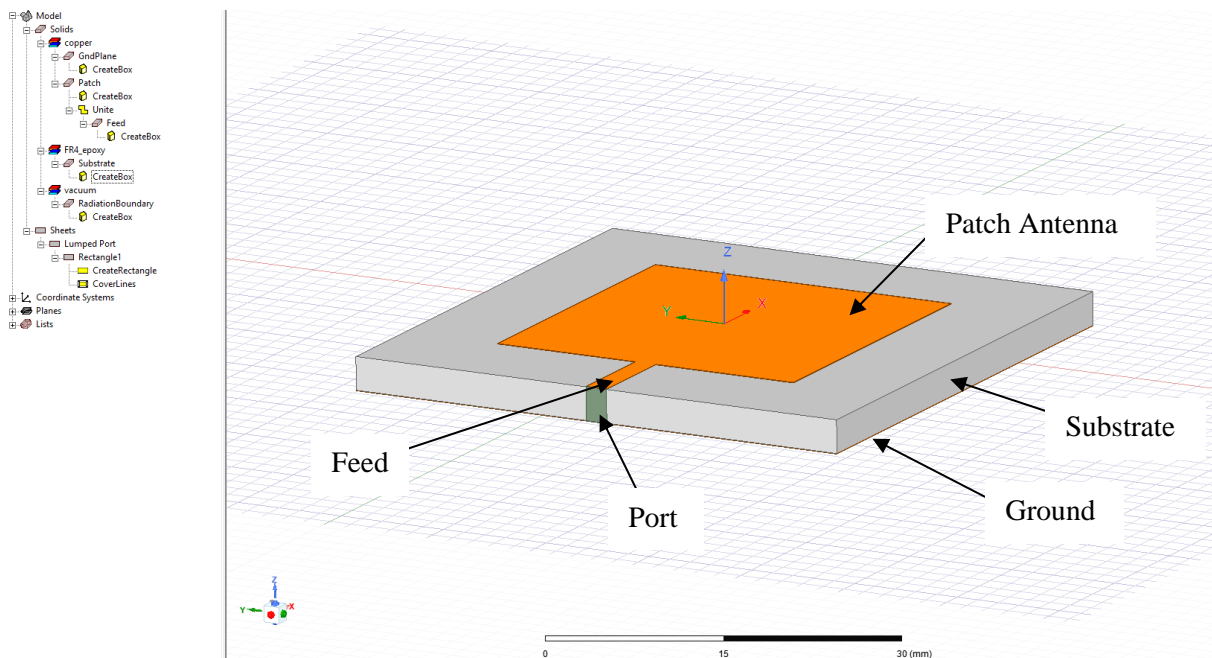


Figure 10.25: Patch Antenna in HFSS

The following calculations are used to determine the effective refractive index and dimensions of the antenna and ground plane:

$$W = \frac{c}{2f} \sqrt{\frac{2}{\epsilon_r + 1}}$$

$$\epsilon_{\text{reff}} = \frac{\epsilon_r + 1}{2} + \frac{\epsilon_r - 1}{2} \left(1 + 12 \frac{h}{W}\right)^{-1/2}$$

$$\Delta L = 0.412h \frac{(\epsilon_{\text{reff}} + 0.3) \left(\frac{W}{h} + 0.264\right)}{(\epsilon_{\text{reff}} - 0.258) \left(\frac{W}{h} + 0.8\right)}$$

$$L = \frac{c}{2f\sqrt{\epsilon_{\text{reff}}}} - 2\Delta L$$

$$L_g = 6h + L$$

Figure 10.26 shows the patch antenna's resonant frequency. It has a smaller 10dB-bandwidth of 84MHz compared to the 844MHz of the dipole. The realized gain is shown in the polar plot in Figure 10.27, and has a gain of 4.18dB at 360deg. Figure 10.28 shows the downscaled 3D radiation pattern and its orientation with respect to the patch antenna, where the darkest red is the point with highest gain.

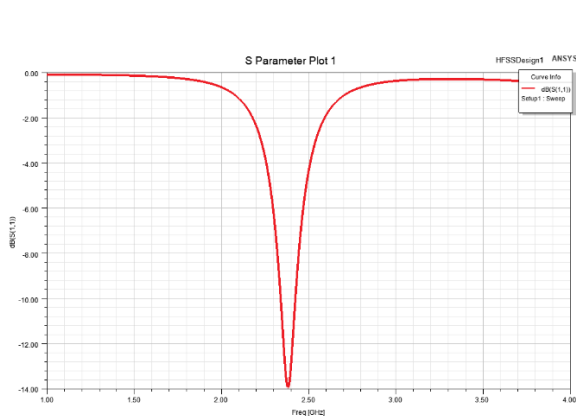


Figure 10.26: Patch Return Loss and Resonant Frequency

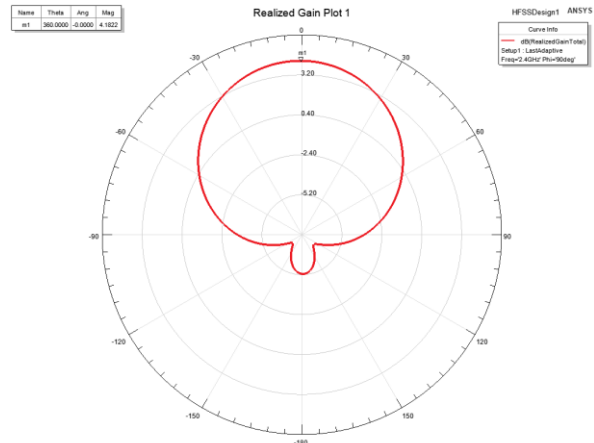


Figure 10.27: Patch Realized Gain Polar Plot

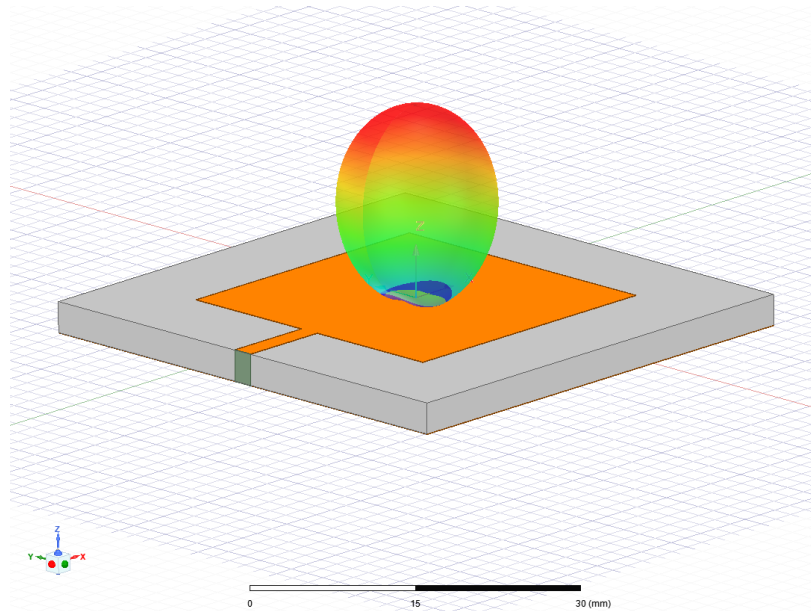


Figure 10.28: Patch Radiation Pattern

Transmission range can be determined using the well-known Friis transmission equation to calculate the power received by one antenna from the other:

$$P_r = \frac{P_t G_t G_r \lambda^2}{(4\pi R)^2}$$

Where:

P_r = Power at the receiving antenna

P_t = Output power of the transmitting antenna

G_t = Gain of the transmitting antenna

G_r = Gain of the receiving antenna

λ = Wavelength

R = Distance between antennas

Per FCC regulations, maximum transmit power is assumed to be 1 Watt, or 30dBm. The dipole is assumed to be the transmitting antenna with a gain of 2.31dB, and the patch antenna is the receiving antenna with a gain of 4.18dB. The receiving and transmitting antennas can be switched with the same results. At a distance of 3.5nmi, power received by the patch antenna from the dipole was -78.6dBm. The sensitivity of

the receiving antenna must be known to determine if the receiver is capable of receiving the signal, but these properties are determined by experimental measures by manufacturers and cannot be simulated. Therefore, similar antennas were researched to determine a range of sensitivities of -80dBm to -100dBm. Results confirmed this configuration is capable of transmitting signals at least 3.5nmi and up to the range of 6-8nmi, assuming conditions are optimal and there is little noise or interference from the surrounding environment.

Because of the small beamwidth, the signal will greatly decrease if the ground station is not pointing in the direction of the aircraft. This is not an issue with the dipole antenna since the signal radiates in a donut shape. Table 10.3 below summarizes the main properties analyzed for both antennas.

Table 10.3: Antenna Properties Summary

	Dipole (Air Unit)	Patch (Ground Controller)
Dimensions	55.2 x 5.25 x 0.5 mm ³	46.8 x 46.8 x 3.1 mm ³ (Overall) 28.8 x 28.8 x 0.05 mm ³ (Patch)
Frequency	2.40 GHz	2.38 GHz
Bandwidth	344 MHz	84 MHz
HPBW	78.6 deg	102.1 deg
Gain	2.31 dB	4.18 dB
Directivity	2.32 dB	6.36 dB

11. V-N DIAGRAM

Figure 11.1 below shows the V-n gust loading diagram. The blue lines on the chart represent the zone of flight conditions the Valkyrie system is capable of operating in. The region is bound on the upper and lower side by a G loading of 17. As the intended enemies of the Valkyrie are typically small, agile, and fast UAVs, designing the structure of the Valkyrie to sustain extremely high G maneuvers increases the likelihood of the aircraft being able to execute and survive high intensity engagements. Of note is the maximum speed indicated on this diagram. While the Valkyrie cannot propel itself to speeds greater than 250 kts, there are certain situations where the vehicle may find itself traveling at higher speeds. The maximum speed denoted on this chart is the dive speed, while the maximum level flight speed occurs on the dashed line at 250 kts. The green upper and lower lines of the V-n diagram are derived from ground handling limits of ± 30 Gs, occurring if dropped in transport. The design setback acceleration for this aircraft will be 1650 Gs due to the firing of the shotgun shell, and the design of the aircraft to withstand speeds in excess of the maximum level flight speed will also be helpful in this respect.

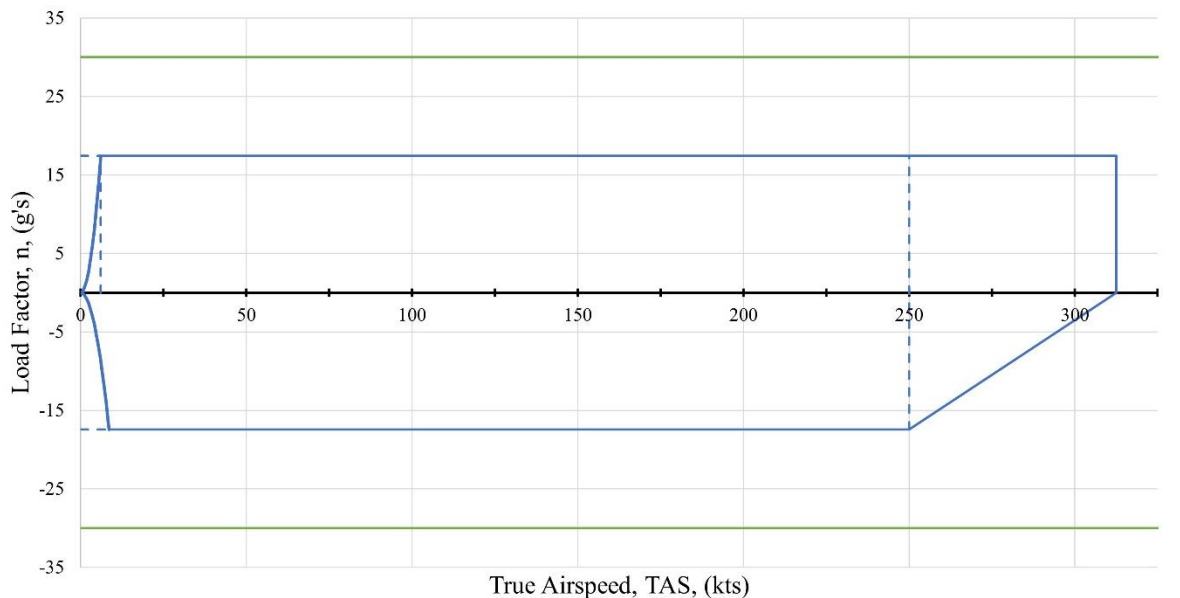


Figure 11.1 Valkyrie V-n Load Diagram

12. DOGHOUSE PLOT AND MANEUVERABILITY DIAGRAM

By tracking the power available at a variety of altitudes as well as the power required at altitude, a thrust matching table was generated, and by tracking the difference in power available minus the power required, the excess power at altitude was ascertained. From this value, the maximum rate of climb was calculated and tracked in Figure 12.1 below. Typically, for internal combustion and jet turbine engines, there is a deprecation of power at altitude due to lower air density, which causes the fuel to burn less effectively. However, since the Valkyrie system utilizes an electric powerplant, it is capable of sustaining power to much higher altitudes than conventionally fueled systems. The flight ceiling is normally set for military aircraft when the rate of climb drops to 100 feet per minute, but for the Valkyrie system, this threshold was never breached, and so the limit was set when the necessary RPM placed the combined tip velocity in the transonic region greatly diminishing the effectiveness of the propeller. Finally, Figure 12.2 on the next page shows the sustainable flight envelope of the Valkyrie system.

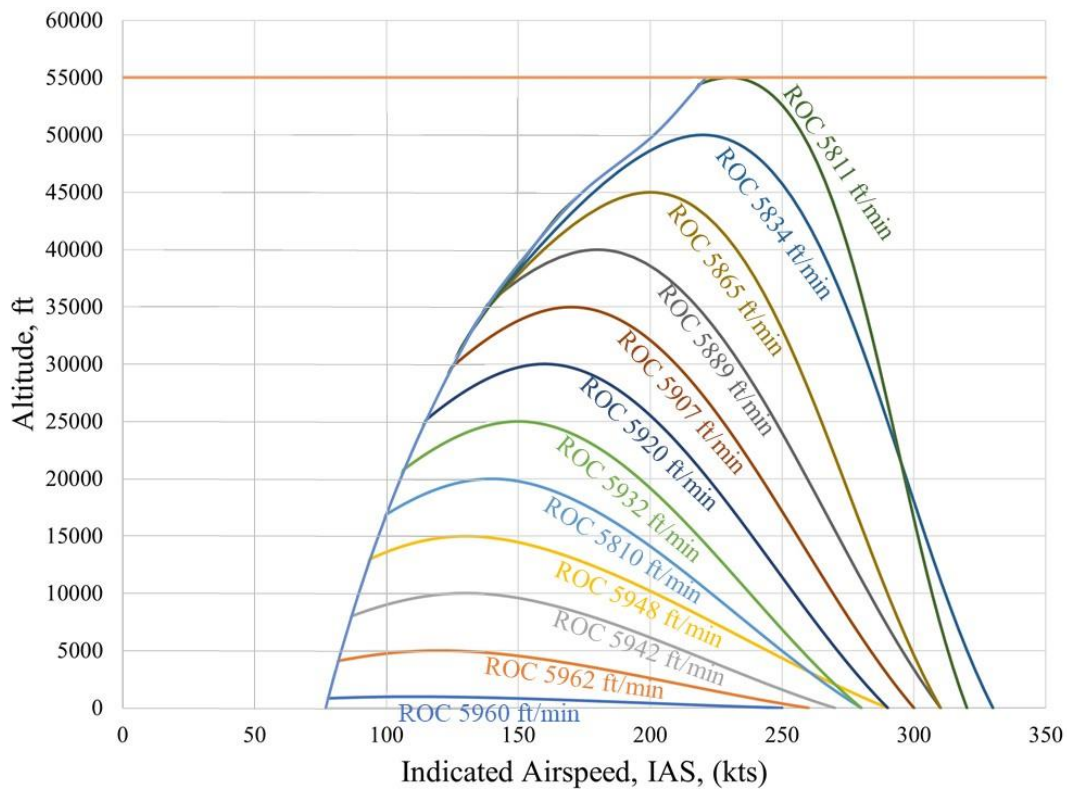


Figure 12.1 Doghouse Plot

The maneuver diagram shown below in Figure 12.2 tracks the degrees per second rate of direction change versus the indicated airspeed the Valkyrie system is capable of executing. As with the V-n diagram, the range of possible flight is delineated by the blue lines. This chart shows that at maximum flight speed, the Valkyrie system is capable of executing a 17 G turn in a radius of just over 300 feet, while at lower airspeeds, the turn radius can be shrunk to under 200 feet. This extreme maneuverability allows the Valkyrie to outmaneuver group 1 and 2 UAV's and ensure proper maneuverability to engage hostiles with the rear facing ARMRS.

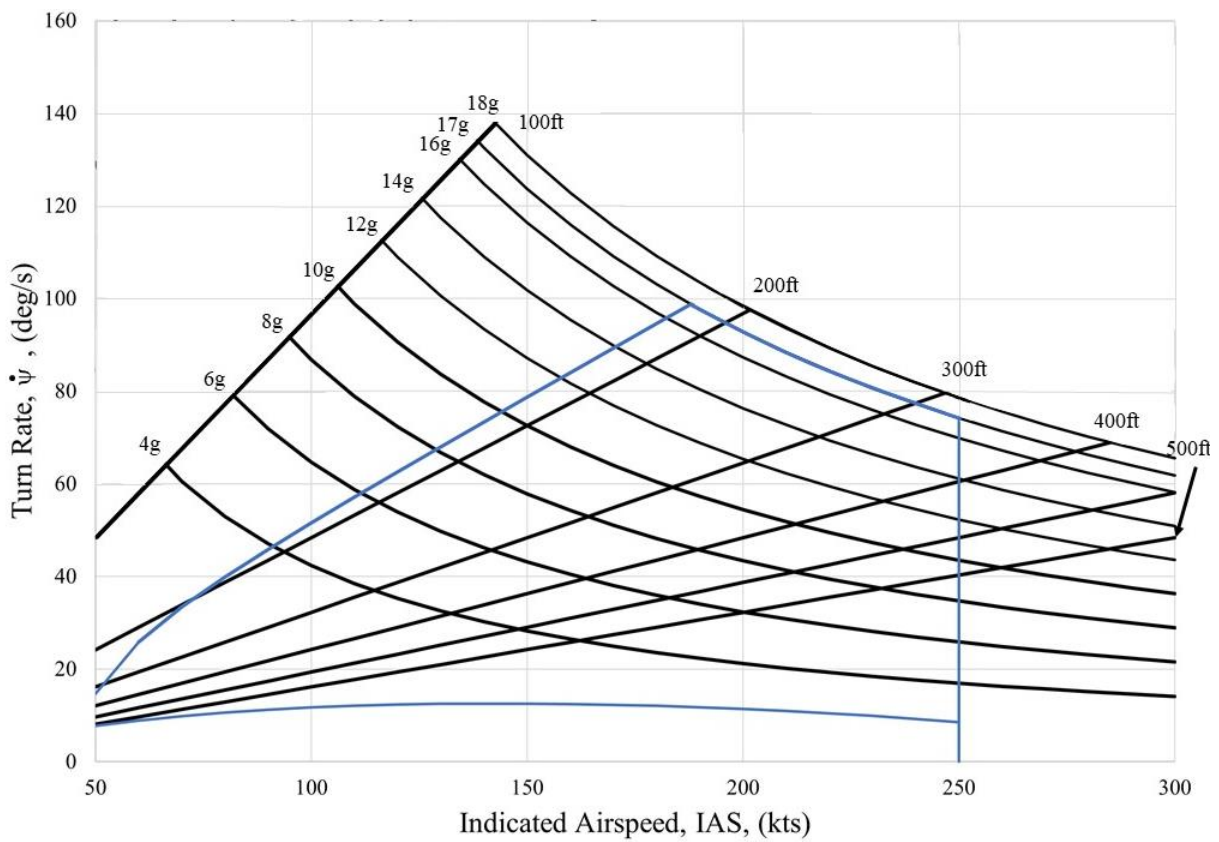


Figure 12.2 Maneuverability Diagram

13. PAYLOAD-RANGE DIAGRAM

Figure 13.1 below presents the payload-range diagram. This figure explores the effect of replacing the kill mechanism mass with increased battery mass upon the range. The empty weight of the aircraft is set at the origin of the graph, and as payload mass is added, the start point of the line moves up the payload axis. From this point, the aircraft can carry out the mission parameters of a 3.5 nautical mile range. Exchanging kill mechanism mass for battery mass increases the mission range. If all payload mass is exchanged for battery mass, the effective ferry mission range of the aircraft can be determined. Figure 13.1 shows a sweep through different cruise speeds and the ferry range abilities of the aircraft. Of note is the dashed lines used to mark the 250 and 225 knot cruise speeds rather than the solid lines used elsewhere. When analyzing the range, battery mass was considered to be entirely composed of the lithium thionyl chloride battery specified previously in the design of the Valkyrie system. This battery chemistry is designed for high discharge rates, and as such will have degraded performance at lower discharge rates. To account for this degradation of performance, the battery power density curve for lithium thionyl chloride was used for the high discharge rates necessary for 250 and 225 knot cruises denoted below with dotted lines, while the remaining lines used the power density line for lithium-ion batteries.

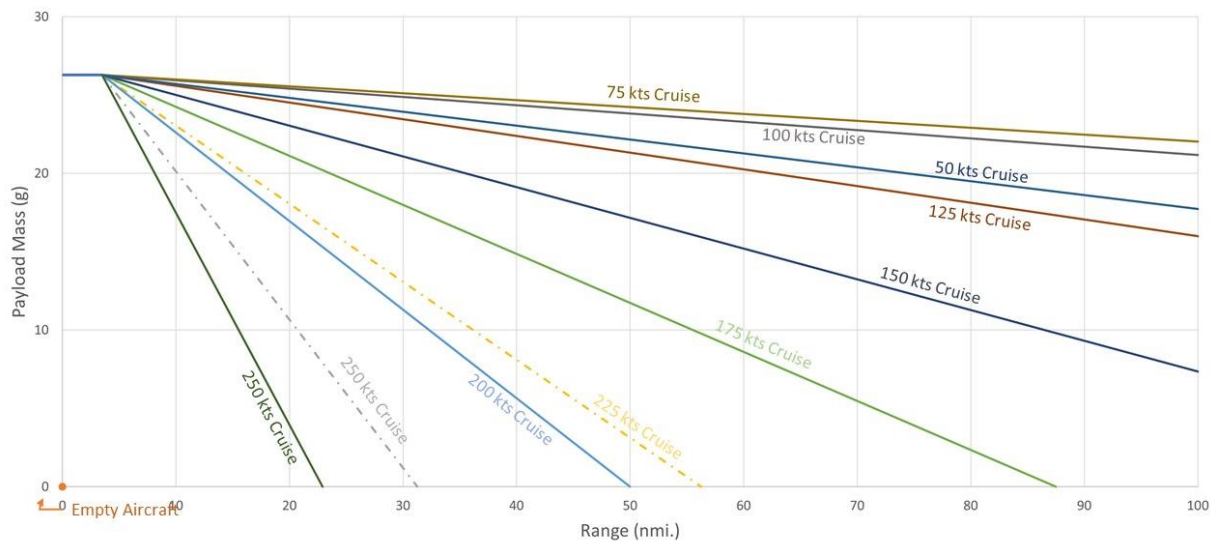


Figure 13.1 Valkyrie Payload Range Diagram for Cruise Altitude of 6000 ft

14. CLASS II WEIGHT AND BALANCE

Class II weight and balance analysis was performed using methods from Roskam's Airplane Design Part V [21]. This section describes the process of determining the updated aircraft component weights, center of gravity locations, the c.g. excursion, and mass moments of inertia.

14.1. WEIGHT AND BALANCE CALCULATIONS

Siemens NX CAD is utilized to determine the volume of components, which along with material density data was used to calculate the weight of components of unknown weight. The c.g. position and weight of each component is summed to determine the overall aircraft weight and c.g.

Table 14.1.1 Component Weights and Locations

Component	Weight (lbf)	F.S. (ft)	B.L. (ft)	W.L. (ft)
Fuselage & Frame	0.0585	0.4593	0.0000	0.0446
Wing	0.0166	0.4003	0.0000	0.0000
V-Tail	0.0128	0.5971	0.0000	0.0732
Battery 1	0.0358	0.2543	0.0000	0.0446
Battery 2	0.0358	0.3101	0.0000	0.0446
Battery 3	0.0362	0.3658	0.0000	0.0446
Battery 4	0.0421	0.4216	0.0000	0.0446
Battery 5	0.0421	0.4774	0.0000	0.0446
Shell	0.0579	0.5217	0.0000	0.0446
Barrel	0.0165	0.5775	0.0000	0.0446
Motor	0.0377	0.1312	0.0000	0.0446
Propeller	0.0077	0.0082	0.0000	0.0446
Electronics	0.0633	0.3937	0.0000	0.0446
Total:	0.4631	0.3513	0.0000	0.0403

of the aircraft. Major components of Valkyrie include the fuselage skin and structure, wing, V-tail, powerplant, batteries, and kill mechanism. Since the aircraft was designed for the x_{cg} location to be directly in the center of the aircraft, the internal components can be rearranged to meet this requirement. Using the c.g. location and weight of each component, their mass moments of inertia are calculated as well. These are used in the following section for Class II stability and control analysis. Weight conditions are considered from both before the kill mechanism shot and after. These are shown in Figure 15.1 below.

14.2. CONCLUSIONS

Class II weight and balance did not change significantly compared to Class I due to the ability to move internal components to adjust the c.g. to the center of the aircraft. Components for which weight percentages were initially used and whose weights were later estimated using material density data had the greatest effect on the c.g., but weight was easily redistributed by reorganizing the battery locations.

15. CLASS I STABILITY AND CONTROL ANALYSIS

The purpose of Class I stability and control analysis is to ensure the current configuration has satisfactory stability and control characteristics. Static longitudinal and directional stability analysis is performed to create x-plots showing the effect of horizontal and vertical tail sizing on control characteristics. Methods from Chapter 11 of Roskam's Airplane Design Part II [14] are used.

The longitudinal stability x-plot shows the aerodynamic center location and center of gravity locations in relation to the horizontal tail sizing. Figure 15.1 shows the x-plot before and after the kill mechanism has been shot. The stability of the aircraft due to the change in weight and balance is compensated by adjusting the wing sweep angle. The c.g. legs are calculated based on Class I weight and balance analysis. The a.c. leg is calculated using the following equations. To initially achieve a ~5% static margin, the mean geometric chord of the wing is moved by adjusting the sweep angle to refrain from changing the horizontal tail sizing dramatically.

$$\bar{X}_{ac_A} = \frac{\bar{X}_{ac_{wf}} C_{L_{\alpha_{wf}}} + C_{L_{\alpha_h}} \left(1 - \frac{d\varepsilon_h}{d\alpha}\right) \frac{S_h}{S} \bar{X}_{ac_h}}{C_{L_{\alpha_{wf}}} + C_{L_{\alpha_h}} \left(1 - \frac{d\varepsilon_h}{d\alpha}\right) \frac{S_h}{S}} \quad K_A = \frac{1}{A} - \frac{1}{1 + A^{1.7}}$$

$$C_{L_{\alpha_{wf}}} = \frac{\pi A}{1 + \sqrt{\frac{A^2 \pi^2}{C_{l_{\alpha}^2(@M)} \left(1 + \frac{\tan^2 \Lambda_{c/2}}{\beta^2}\right)} + 1}} \quad K_\lambda = \frac{10 - 3\lambda}{7}$$

$$\frac{d\varepsilon_h}{d\alpha} = 4.44 \left[\frac{C_{l_{\alpha}(@M)}}{C_{l_{\alpha}(@M=0)}} \{K_A K_\lambda K_h \sqrt{\cos \Lambda_{c/2}}\}^{1.19} \right] \quad K_h = \frac{1 - h_h/b}{\sqrt[3]{2 l_h/b}}$$

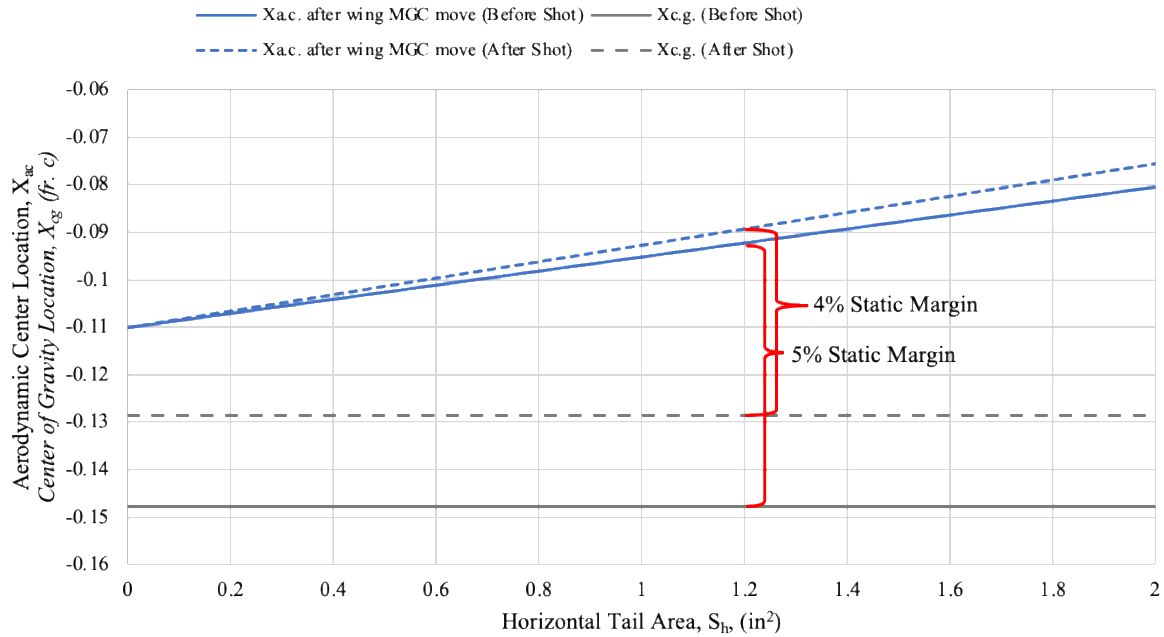


Figure 15.1 Longitudinal Stability X-Plot Before and After Shot

The directional stability x-plot shows the effect of vertical tail size on the yawing moment coefficient due to sideslip, as shown in Figure 15.2. The c.g. legs are again calculated based on Class I weight and balance analysis. The yawing moment coefficient due to sideslip is calculated using the following equations. The vertical tail size is increased until a yawing moment coefficient of at least +0.001 /deg is achieved.

$$C_{n\beta} = C_{n\beta_{wf}} + C_{L\alpha_v} \left(\frac{S_v}{S} \right) \left(\frac{X_v}{b} \right)$$

$$C_{n\beta_{wf}} = -K_N K_{R1} \left(\frac{S_{f_s} l_f}{S b} \right)$$

The value of K_N is determined using factor accounting for wing-fuselage interference with directional stability and K_{R1} is determined using the effect of fuselage Reynold's number on wing-fuselage directional stability from Roskam's Airplane Design Part VI [22].

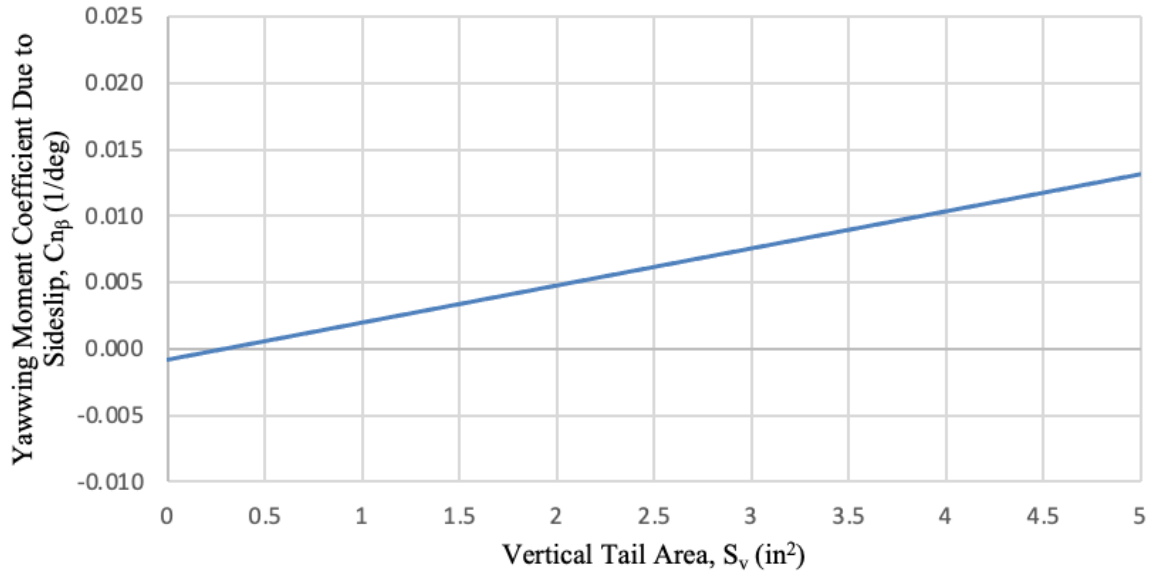


Figure 15.2 Directional Stability X-Plot

16. CLASS I DRAG POLAR

The purpose of this section is to determine the Class 1 drag polar for the Valkyrie system. Methods used in Roskam's Airplane Design Part I [9] and Part II [14] are used.

The three main components used to calculate are the fuselage, wing, and empennage wetted areas, S_{wet} . The wetted area of each section is found using Siemen's NX CAD software and verified analytically to check for accuracy. The local perimeters along the fuselage section of the aircraft can be seen in the perimeter plot in Figure A8.1.

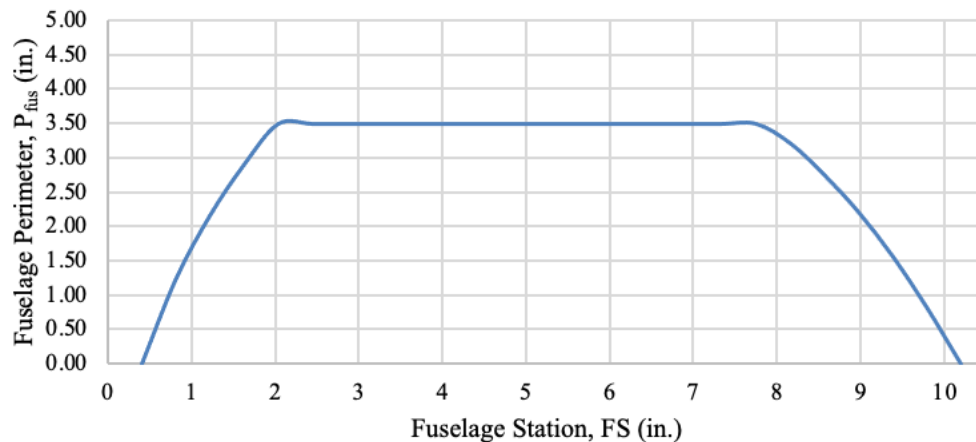


Figure 16.1 Perimeter Plot

The equivalent parasite area, f , is found using equations previously mentioned in this report. The variables a and b are correlation coefficients which are a function of the equivalent skin friction coefficient, c_f . For a c_f 0.0030, variable a is -2.5229 and b is 1.0. The total S_{wet} is 46.3 in^2 . The zero-lift drag coefficient, C_{D0} , is calculated by dividing the equivalent parasite area by the wing area, then drag coefficient is calculated. Since there are no flaps or landing gear, there is no drag increments to consider; therefore only the clean drag polar is calculated. Assuming an aspect ratio of 6 and Oswald efficiency of 0.80, the drag polar can be assumed:

$$C_D = 0.0126 + 0.0663C_L^2$$

17. ANALYSIS OF WEIGHT AND BALANCE, STABILITY AND CONTROL, AND L/D

RESULTS

Longitudinal and directional stability analysis results are listed in Table 17.1. As shown, before the kill mechanism is shot, the static margin is 5.54%. At this point, the wing sweep angle is 42.75 deg. After the shot, the c.g. of the aircraft changes, so the sweep angle is decreased to 37.75 deg to move the m.g.c. enough to achieve a 3.91% static margin. Because it is electrically powered, other factors such as fuel burn will not affect the c.g. throughout flight. For an aircraft of this small size, the static margins are sufficient to achieve longitudinal stability. Yawing moment coefficient with a vertical tail area of 0.65 in² results in a yawing moment coefficient of 0.0010 per deg. being sufficient enough to achieve a +0.001 per deg. minimum.

Table 17.1 Longitudinal and Directional Stability

Static Margin Before Shot	5.54%
Static Margin After Shot	3.91%
Yawing Moment Coefficient, $C_{n\beta}$	0.0010 /deg.

It is assumed that the c.g. of the aircraft is directly at the midpoint of the aircraft lengthwise. This will be managed by repositioning and balancing the aircraft to achieve this. As mentioned, the only factor affecting the c.g. is the weight of the shotgun shell after being shot and the change in c.g. position will be accounted for in reducing the wing sweep angle to move the m.g.c. forward with the c.g.

18. CLASS II STABILITY AND CONTROL

The model of our aircraft was entered into Advanced Aircraft Analysis (AAA). Using the various outputs from our AAA model, further calculations could be made to determine our aircrafts phugoid, short period, spiral, and Dutch roll modes as well as the max roll rate and pitch break. These equations and relationships were determined using AAA and other equations from Roskam's Airplane Design Part VII chapter 3 [20].

Stability regulations are broken down into three levels based on handling quality and tolerated pilot workload, with Level 1 being the best and Level 3 being the worst. Valkyrie is considered Class IV, which encompasses high maneuverability aircraft such as fighters, attack, and tactical reconnaissance aircraft. Therefore Military Appendix B regulations are followed for dynamic stability flight condition requirements.

For longitudinal stability, phugoid and short period flight dynamic modes are analyzed. For phugoid mode, speed and attitude angle account for a low undamped natural frequency and low damping ratio. For short period mode, angle of attack and attitude angle account for a high undamped natural frequency and moderately high damping ratio. Valkyrie is also considered a category A, B, and C aircraft because it utilizes nonterminal flight phases that require rapid and gradual maneuvering, and terminal flight phases that require gradual maneuvering. Lateral-directional stability, roll, spiral, and Dutch roll modes are also analyzed. Roll angle has the most effect on the roll mode, roll angle and yaw angle have the most effect on spiral mode,

and Dutch roll is affected most by sideslip angle and roll angle. Results for both longitudinal and lateral-directional and their respective limits are summarized in Table 18.1 below.

Table 18.1: Class II Stability and Control Variables

Stability Criteria	Stability Limits	Valkyrie
ω_{np}	~	0.081 rad/s
ζ_p	$\zeta_p > 0.04$	0.497
ω_{nsp}	$\omega_{nsp} < 100$ Hz	15.63 rad/s
ζ_{sp}	Category A & C: $0.35 < \zeta_{sp} < 1.30$ Category B: $0.30 < \zeta_{sp} < 2.00$	0.930
ω_{nd}	$\omega_{nd} < 1.0$	19.08 rad/s
ζ_d	$\zeta_d < 0.19$	0.910
$ P_{max} $	~	.0045 rad/s
T_{2s}	$T_{2s} > 0$ s	5.04 s
T_R	$T_R < 0.4$ s	-0.70 s

AAA also determines if the stability criteria fit into specified groups and levels. Valkyrie is considered a Group IV Category A aircraft. Figure 18.1 below shows the levels achieved by the longitudinal damping ratios followed by Figure 18.2 with the Dutch roll and spiral modes. AAA does not show roll performance check modes for a V-tail aircraft without true lateral control surfaces, though it still calculates the roll mode time constant. All stability requirements fall within the Level 1 requirements.

$T_{1/2p}$	<input type="text" value="17.149"/> s	? Level _p = 1	? Level $\zeta_{sp} = 1$? Level $\omega_{nsp} = 1$
------------	---------------------------------------	--------------------------	--------------------------	----------------------------

Figure 18.1: Longitudinal Damping Ratio Levels Achieved

$T_{1/2s}$	<input type="text" value="11.065"/> s	? Level _s = Stable	? Level $\zeta_D = 2$? Level $\omega_{nD} = 1$
------------	---------------------------------------	-------------------------------	-----------------------	---------------------------

Figure 18.2: Spiral and Dutch Roll Levels Achieved

$$\omega_{np} = 1.414 \left(\frac{g}{U_1} \right) \text{ eq. 3.10 [23]}$$

$$\omega_{nD} = \sqrt{\frac{Y_\beta N_r + N_\beta (U_1 - Y_r)}{U_1}} \text{ eq. 3.26 [23]}$$

$$\zeta_p = \frac{C_{Du} + 2C_{D1} - C_{T_{xu}} - 2C_{T_{x1}}}{2.828C_{L1}} \text{ eq. 3.9, 3.10 [23]}$$

$$\zeta_D = -\frac{N_r + Y_\beta / U_1}{2\omega_{nD}} \text{ eq. 3.27 [23]}$$

$$\omega_{nSP} = \sqrt{\frac{Z_\alpha M_q}{U_1} - M_\alpha} \text{ eq. 3.11 [23]}$$

$$|P_{\max}| = \left| \frac{L_{\epsilon_a} \delta_a}{L_p} \right| \text{ eq. 3.37 [23]}$$

$$\zeta_{SP} = -\frac{M_q + \frac{Z_\alpha}{U_1} + M_{\dot{\alpha}}}{2\omega_{nSP}} \text{ eq. 3.12 [23]}$$

A trim diagram is used to show the relationship between the aircraft lift coefficient and pitching moment. Two plots are generated using AAA for lift coefficient vs. angle of attack and lift coefficient vs. pitching moment coefficient as seen in Figure 18.3. The black lines represent the most forward and aft c.g. positions. The lines are capped by the maximum angle of attack line and the area inside represents the area and angle of attacks the aircraft can be properly trimmed.

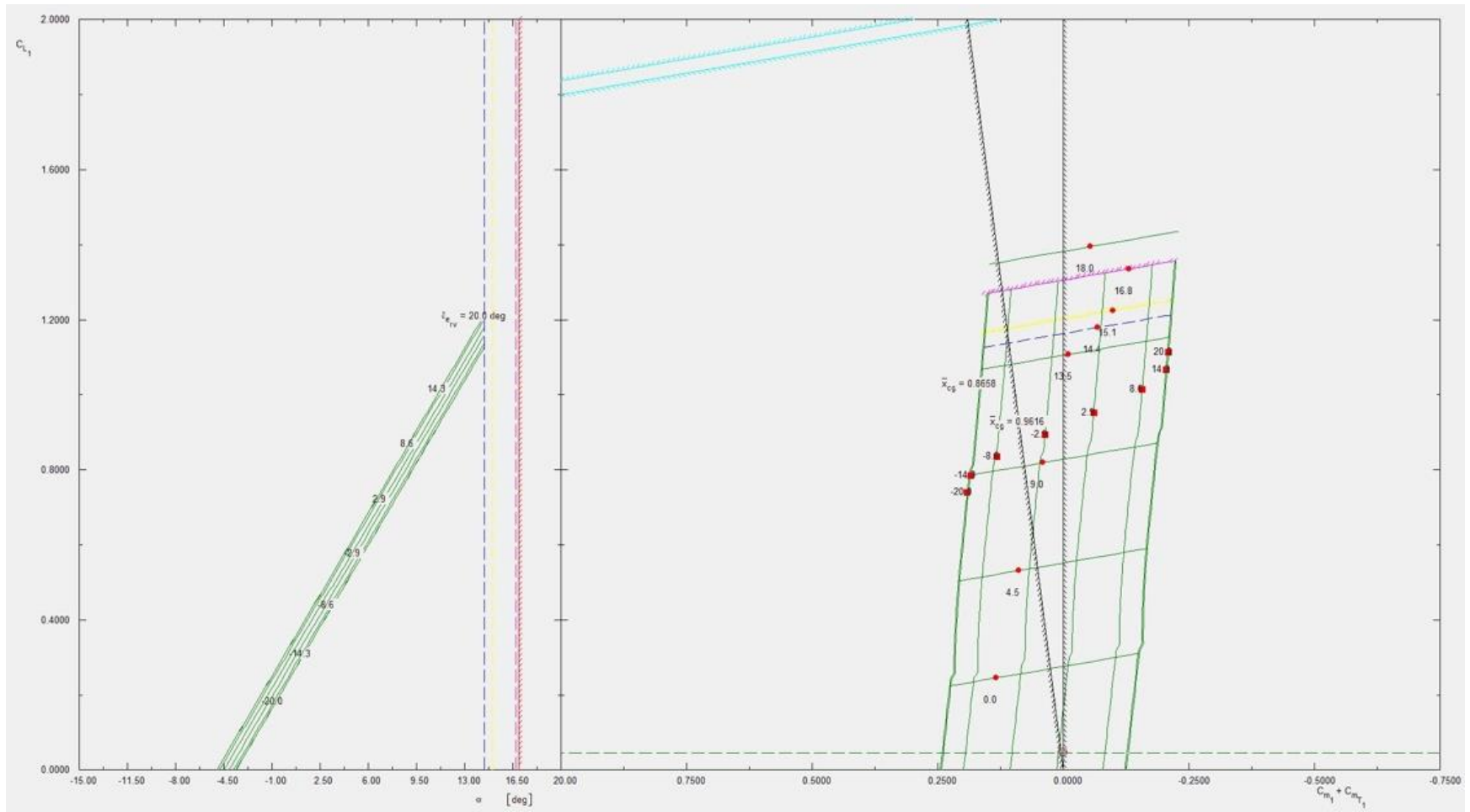


Figure 18.3: AAA Trim Diagram

Table 18.2: Stability and Control Derivatives

Longitudinal Stability Derivatives		
Steady State		
$C_{D_1} = 0.0143$	$C_{L_1} = 0.0485$	$C_{m_1} = 0.0193$
$C_{T_{x_1}} = 0.0143$	$C_{T_{z_1}} = -0.0009$	$C_{m_{T_1}} = -0.0193$
Speed		
$C_{D_u} = 0.0038$	$C_{L_u} = 0.0043$	$C_{m_u} = -0.0044$
$C_{T_{x_u}} = -0.0430$		$C_{m_{T_u}} = 0.0000$
Angle of Attack (rad^{-1})		
$C_{D_\alpha} = 0.0297$		$C_{L_\alpha} = 3.5798$
$C_{m_\alpha} = -0.6607$		$C_{m_{T_\alpha}} = 0.3631$
Angle of Attack Rate (rad^{-1})		
$C_{D_{\dot{\alpha}}} = 0.0000$	$C_{L_{\dot{\alpha}}} = 1.2701$	$C_{m_{\dot{\alpha}}} = -5.5311$
Pitch Rate (rad^{-1})		
$C_{D_q} = 0.0000$	$C_{L_q} = 6.7035$	$C_{m_q} = -54.1707$
Lateral-Directional Stability Derivatives		
Sideslip (rad^{-1})		
$C_{y_\beta} = -0.2309$	$C_{l_\beta} = 2.0644$	$C_{n_\beta} = -0.0435$
$C_{y_{T_\beta}} = -0.0494$		$C_{n_{T_\beta}} = -0.0207$
Sideslip Rate (rad^{-1})		
$C_{y_{\dot{\beta}}} = 0.0136$	$C_{l_{\dot{\beta}}} = -0.0014$	$C_{n_{\dot{\beta}}} = -0.0043$
Roll Rate (rad^{-1})		
$C_{y_p} = -0.0041$	$C_{l_p} = -0.3226$	$C_{n_p} = -0.0177$
Yaw Rate (rad^{-1})		
$C_{y_r} = 0.0636$	$C_{l_r} = 0.0429$	$C_{n_r} = -0.0259$
Longitudinal Control Derivatives		
V-Tail Incidence Control Derivatives (rad^{-1})		
$C_{D_{i_{vee}}} = 0.0055$	$C_{L_{i_{vee}}} = 0.2171$	$C_{m_{i_{vee}}} = -0.9452$
Lateral-Directional Control Derivatives		
V-Tail Control Derivatives (rad^{-1})		
$C_{y_{i_{vee}}} = 0.0272$	$C_{l_{i_{vee}}} = 0.0027$	$C_{n_{i_{vee}}} = -0.0072$

19. COST ANALYSIS AND DEVELOPMENT PLAN

19.1. COST ANALYSIS

The cost of our system was estimated using Dr. Roskam's techniques presented in Part VIII of his Airplane Design series [24]. Table 19.1.1 shows the cost analysis of the missile program for a production of 200 missiles a year for 10 years, assuming 15 missiles for development testing based on the request for proposal [1]. Table 19.1.1 below shows the estimated price per missile at various production runs. Of note is that Table 19.1.1 and the calculations used to generate Figure 19.1.1 do not take into account the reusability of our design and therefore only account for the amount of complete systems built.

Table 19.1.1: Cost Analysis of Program Development

Airframe engineering and design cost	\$1,293
Development support and testing cost	\$1,559
Cost of flight tests models	\$190,422
Cost of engines and avionics in RDT&E	\$9,993
Manufacturing labor costs in RDT&E	\$91,233
Materials cost in RDT&E	\$40,334
Tooling cost in RDT&E	\$37,000
Quality control cost in RDT&E	\$11,860
Flight test operations cost	\$284
Test and simulation facilities cost	\$200,000
Profit cost	\$1,000,000
Financing cost	\$1,202
Total RDT&E cost	\$1,393,559
Tooling cost for manufacturing	\$79,056
Materials cost for manufacturing	\$1,914,903
Manufacturing labor cost	\$1,098,148
Cost of engine and avionics for production	\$1,332,450
Airframe production cost	\$4,567,317
Airframe engineering and design cost	\$40,482
Total materials cost for program	\$1,955,238
Total profit of program	\$207,350
Total manufacturing cost of program	\$4,607,798
Total acquisition cost of program	\$4,815,149
Estimated price per missile	\$3,104

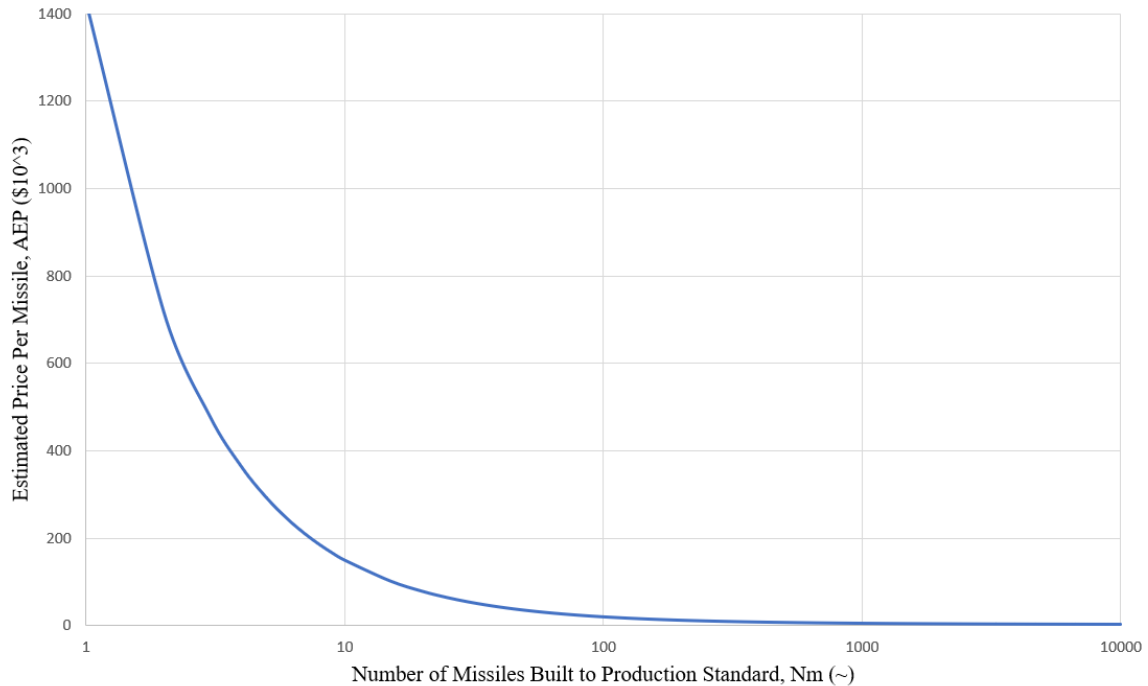


Figure 19.1.1: Estimated Price per Missile at Various Production Runs on a Logarithmic Scale

19.2. DEVELOPMENT PLAN

The Valkyrie system is only 10 in long and 1.6 in wide, so it does not require large manufacturing facilities. In addition, many of the parts can be outsourced. For these reasons the assembly process can be done almost anywhere. However, consideration must be given to finding engineering talent to work at the location and proximity to DoD testing grounds and facilities. Examples of such locations are Huntsville Alabama, Rockaway New Jersey, and Baltimore Maryland. Finally, the Valkyrie system does not use any emerging technologies and therefore can be manufactured immediately if required, thus meeting the RFP requirement of having an initial operational capability before December 2027.

The assembly process is broken down into five different parts: skin, wing, tail, ARMRS, structural/electronics assembly, and final assembly. As shown previously, the outer skin of Valkyrie is built from graphite PEEK composite. Therefore, the manufacturing process is relatively simple in taking the raw graphite PEEK composite and completing a traditional vacuum molded composite lay-up. Once

completed, the composites would undergo quality assurance testing to ensure accuracy and structural capability (Figure 19.2.1).

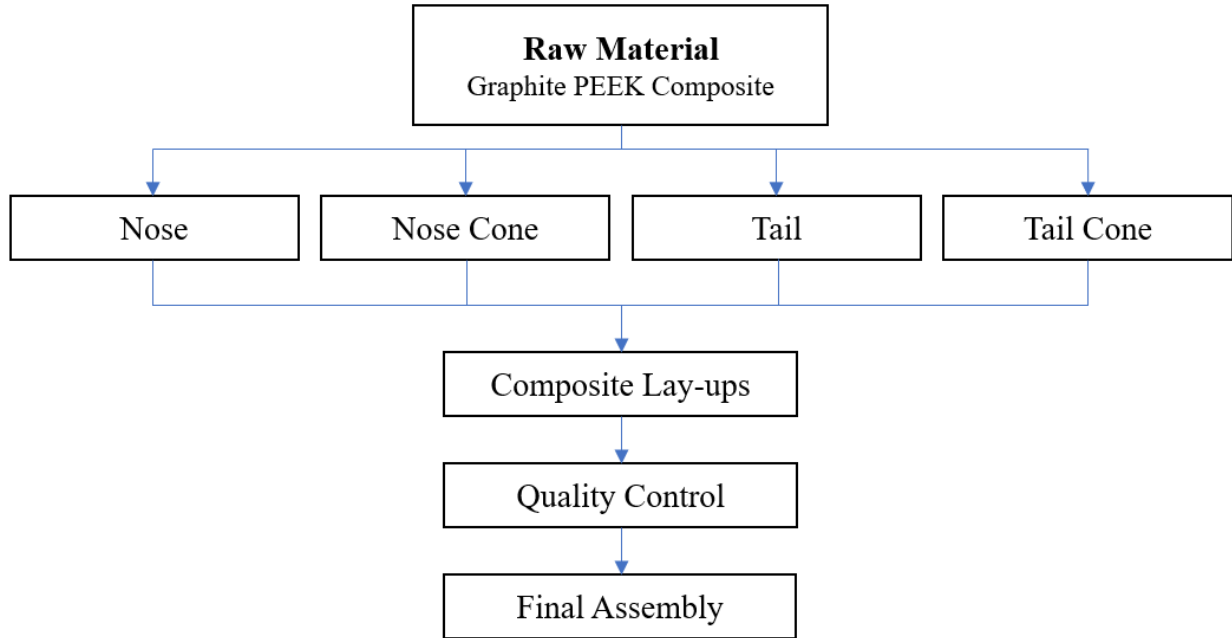


Figure 19.2.1: Skin Manufacturing and Assembly Diagram

The assembly process of the wing follows a very similar process wherein the raw graphite PEEK composite would be laid up into a wing mold. However, it differs in that the antennas and steel pivot bushings and posts would be outsourced and then integrated onto the wing before final assembly (Figure 19.2.2).

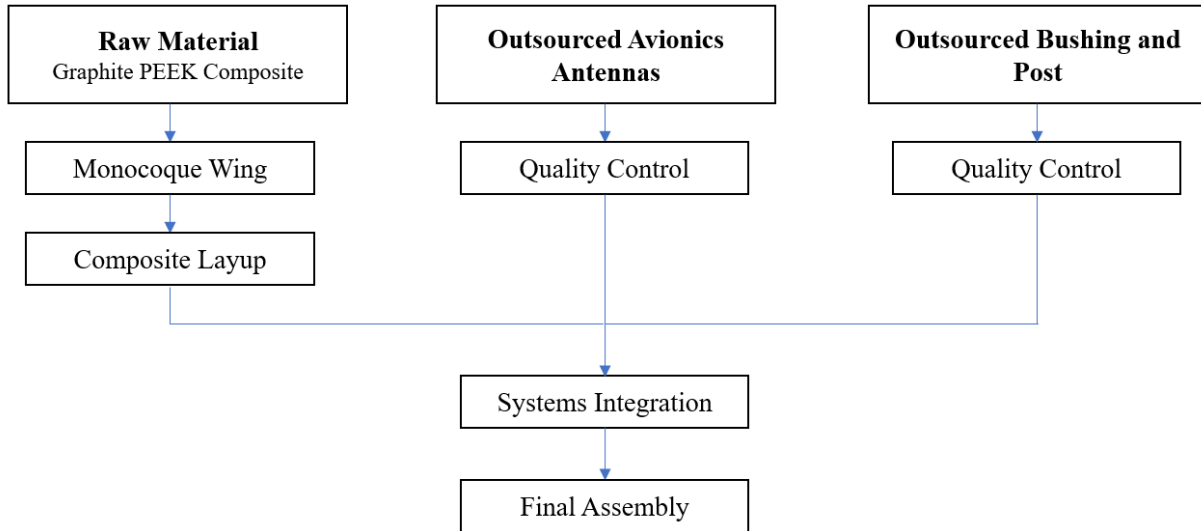


Figure 19.2.2: Wing Manufacturing and Assembly Diagram

Almost identical to the wing assembly process is the V-tail assembly process. Once again, graphite PEEK composite is laid up into a mold. However, it differs in that instead of antennas being placed in the wing, a piezoelectric torque plate is placed in the wing for control. This torque plate and the steel pivot bushings and posts are outsourced and then integrated onto the wing before final assembly (Figure 19.2.3).

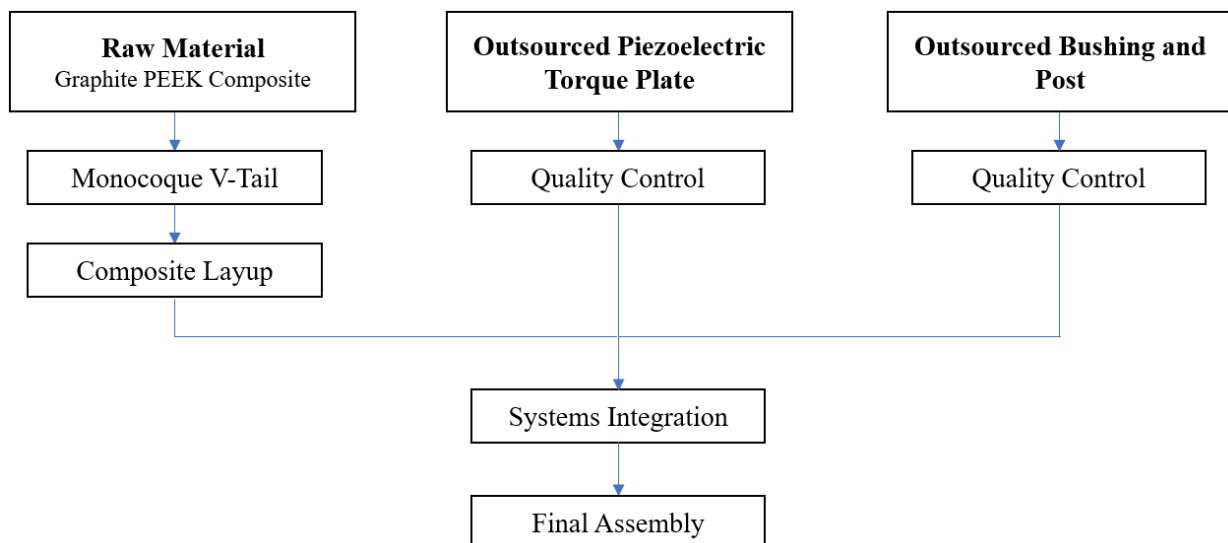


Figure 19.2.3: V-tail Manufacturing and Assembly Diagram

The two complex assembly processes occur in the ARMRS and electronics and internal structure assembly. The inner and outer structure of the ARMRS system is 3D printed and then assembled together while the hexagonal shot is assembled separately in a similar manner to traditional shotgun shells where unloaded shells are loaded with carefully measured amounts of shot and gunpowder. Once the shells have been checked for quality assurance, they can undergo system integration with the inner and outer ARMRS structure before passing on to final assembly (Figure 19.2.4).

The internal structure undergoes a traditional graphite PEEK composite layup. However, it has to be integrated with the internal battery, avionics, and sensors before final assembly. The batteries follow a traditional C-cell and 2/3 C-cell size and so are easily outsourced. In addition, avionics and sensors for the Valkyrie system are readily found online and can be outsourced as well. Therefore, the avionics and sensors need only to undergo quality assurance when delivered and then assembled onto the internal structure for final assembly (Figure 19.2.5).

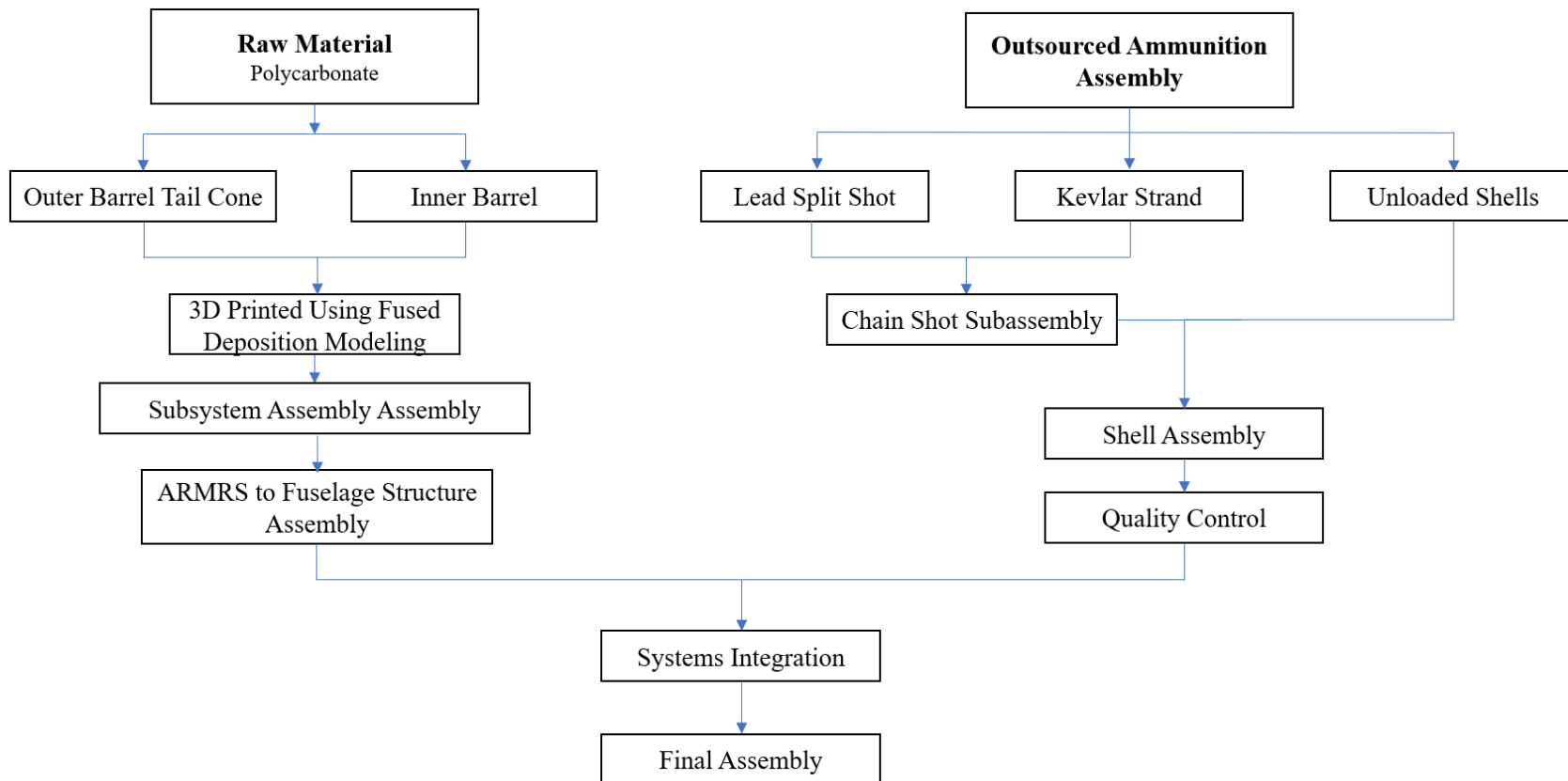


Figure 19.2.4: ARMRS Manufacturing and Assembly Diagram

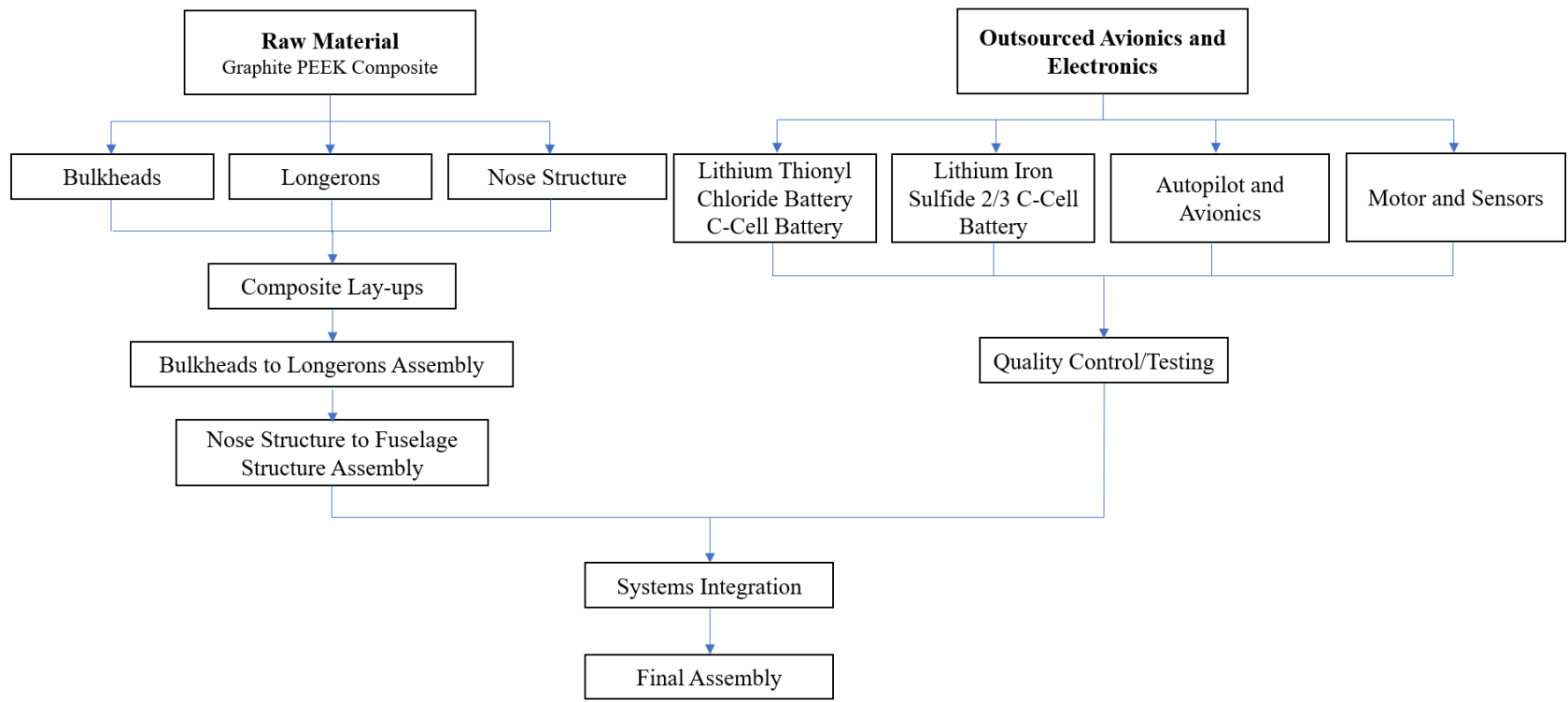


Figure 19.2.5: Internal Structure and Electronics Manufacturing and Assembly Diagram

Figure 19.2.6 below shows the final assembly process where the five different sub-assemblies are assembled together and then inspected, ground tested, and finally flight tested before undergoing delivery to customers.

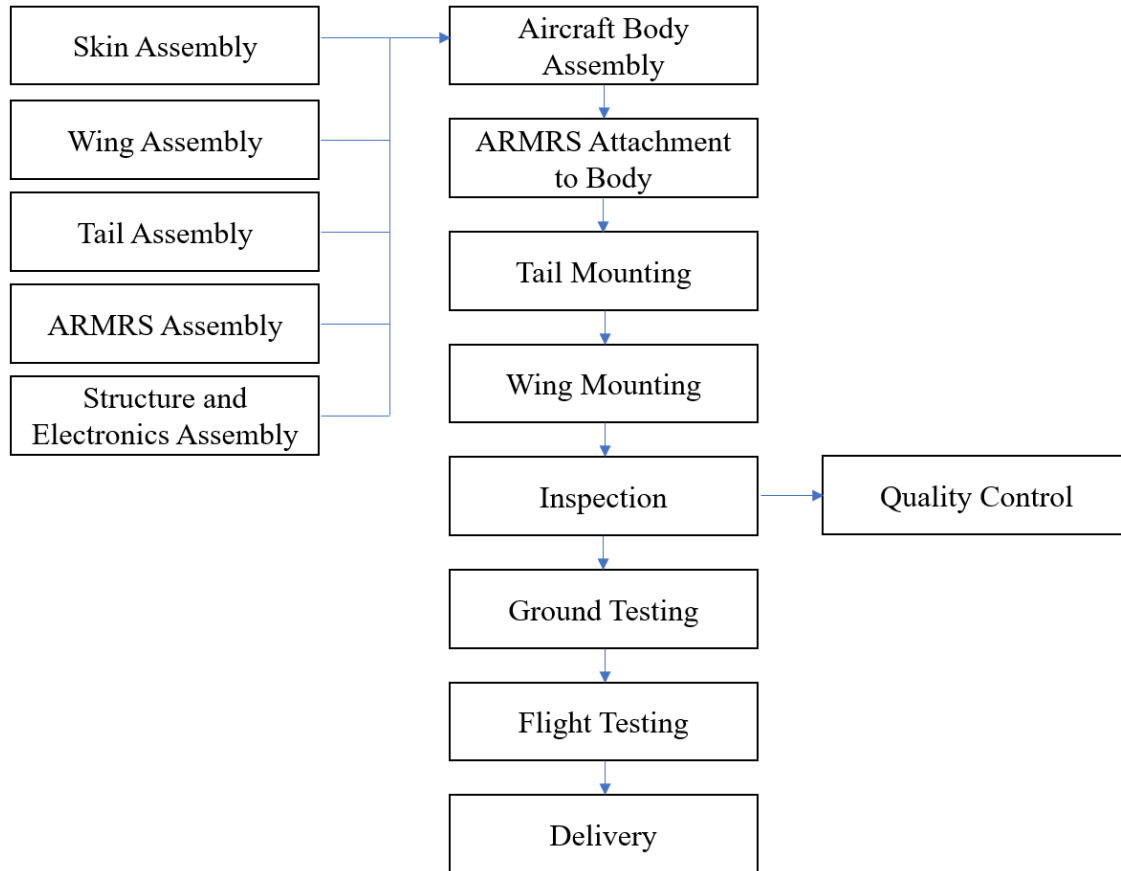


Figure 19.2.6: Final Assembly and Testing Diagram

20. WIND TUNNEL AND FLIGHT TESTING [25]

20.1. WIND TUNNEL AND FLIGHT TEST MODEL FABRICATION

The Valkyrie model used for wind tunnel testing was designed at the full-scale.

This was possible due to the Valkyrie's naturally relatively small form factor and allowed the test to capture Reynolds numbers effects. Given limited time, workforce, and budget, the model was designed to be unpowered and in a typical cruise configuration. The model was designed with a removable empennage assembly and closeout ogive so as to allow

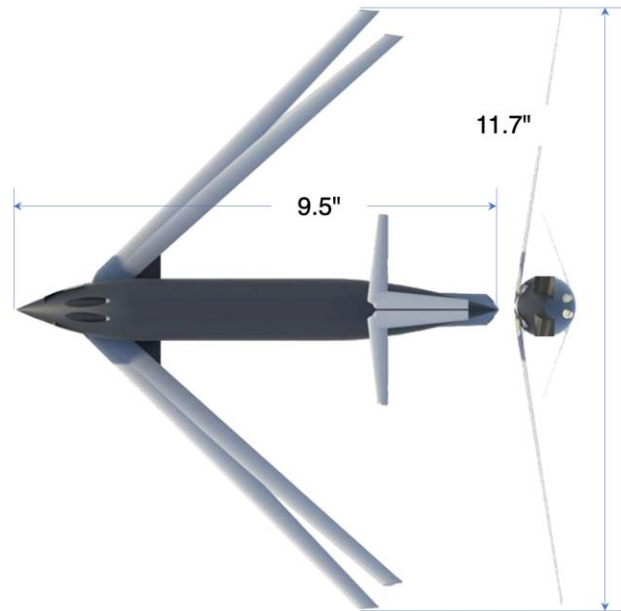


Figure 20.1.1: Wind Tunnel Model Dimensions

for sting mounting as well as testing of the wing-body combinations for more detailed design of the empennage and its effectors. The wind tunnel model was laid out in the return-cruise configuration initially with the possibility of changing sweep angle to the climb-interceptor configuration (more aft sweep configuration, at right) in future testing.

The Valkyrie wind tunnel was fabricated from flight-weight materials including balsa wood and flight body tubes. The goal of the fabrication was to generate an aircraft model that could be used for both wind tunnel testing, freeflight, and aeromechanical spin testing. As such, weight was a concern. Fillets were formed at all structural joints by using flight-weight filler with fixed pitches. Three different empennages



Figure 20.1.2: Wind Tunnel Model During Fabrication

and closeout ogives were fabricated so as to accommodate wing-body testing as well as two different pitch positions of the empennage to verify control authority. The completed, finished model weighed in at 26.2g (0.92 oz). The surface was finished to a 400-grit stage before priming and painting. Figure 20.2.1 below shows the finished test model in hand with the flight-worthy

empennage and tail ogive installed.

20.2. WIND TUNNEL TESTING

Subsonic testing of the model was conducted at the University of Kansas 3 x 4' subsonic wind tunnel. Test conditions ranged from 0 to 50 ft/s at limited angles of attack. Basic instrumentation was used to verify lift coefficients with angles of attack as well as aerodynamic center locations. Unfortunately, due to the fragility of the model, angles of attack were limited to under 5 deg. However, lift trends were established and almost precisely modeled



Figure 20.1.1: 100% Scale Wind Tunnel Model

aerodynamic predicted by AAA, thus validating our Class II stability and control. The aerodynamic center was determined to be 4.72" back from the nose ogive apex, again mirroring AAA results. Unfortunately, stall performance was not able to be captured given limited time.

20.3. FREEFLIGHT AND SPIN TESTING

A series of freeflights and spin tests were conducted to verify a.c. location. Spin testing was conducted at speeds ranging from 30 - 35 ft/s on the 100% scale model built for wind tunnel testing. Freeflight testing was conducted at 20 - 25 ft/s with a trimmed empennage configuration for gliding flight. These tests demonstrated the a.c. to be between 4.71 and 4.75" from the nose ogive apex over 30 spin tests. Glide ratios of 17.2 - 18.9:1 were observed over 15 free flights. Continued testing is planned over the summer.



Figure 20.2.1: 100% Scale Wind Tunnel Model in KU 3 x 4' Tunnel



Figure 20.3.2: 100% Scale Model prior to Spin Test Launch

REFERENCES

1. Anon, *2020-2021 Graduate Team Missile Systems Design Competition – Shoulder-Launched Anti-UAV Missile System*, pp 1-2.
2. Hoen, John R. and Sayler, Kelley M., “Department of Defense Counter-Unmanned Aircraft Systems” *Congressional Research Service* [<https://fas.org/>] 11, January 2021.
3. Anon, “DroneHunter,” *Fortem Technologies* [<https://fortemtech.com>].
4. Anon, “12 Gauge: SKYNET Mi5,” *Pacem Defense* [<https://www.lessletha.com/>].
5. Anon, “NetGun X1 – Short Range Drone Protection,” *Drone Defense* [<https://www.dronedefence.co.uk/>].
6. Anon, “More European Police Choose Skywall Net Capture Following Competitive Tender,” *Dronewatch EU* [<https://www.dronewatch.eu/>].
7. Anon, “Skywall Patrol,” *OpenWorks Engineering* [<http://openworksenineering.com/>].
8. Anon, “DRONEKILLER,” *IXI Electronic Warfare* [<https://www.ixiew.com/>].
9. Roskam, J., *Airplane Design Part I: Preliminary Sizing of Airplanes*, Lawrence, Kansas: DARcorporation, 2018.
10. Beard, Kirby, *Linden’s Handbook of Batteries*, Fifth Edition.
11. Barrett, R., “AE 722 Lecture Powerpoint Slides,” Lawrence Kansas, 5 March 2021.
12. Anon., *Tadiran Lithium Batteries*.
13. Crispin, M., “BEMT Technical Conversation,” Lawrence Kansas, 25 April 2021.
14. Roskam, J., *Airplane Design Part II: Preliminary Configuration Design and Integration of the Propulsion System*, Lawrence, Kansas: DARcorporation, 2018.
15. Anon., “M203 grenade launcher,” *Wikipedia* [<https://wikipedia.org/>].
16. Amrein, Bruce, Letowski, Tomasz, *High Level Impulse Sounds and Human Hearing Standards, Physiology, Quantification*, May 2012.
17. Anon., *Shoulder-Launched-Energy-Report*, Fort Detrick, US Army, May 2004.

18. Anon., "M-4 Carbine," *Wikipedia* [<https://wikipedia.org/>].
19. Barrett, R., "AE 722 Lecture Powerpoint Slides," Lawrence Kansas, 17 February 2021.
20. Ansys HFSS, Software Package, Ver. 15.0, ANSYS, Inc., Canonsburg, PA, 2014
21. Roskam, J., *Airplane Design Part V: Component Weight Estimation*, Lawrence, Kansas: DARcorporation, 2018.
22. Roskam., J., *Airplane Design Part VI: Preliminary Calculation of Aerodynamic, Thrust, and Power Characteristic*, Lawrence, Kansas: DARcorporation, 2018.
23. Roskam, J., *Airplane Design Part VII: Determination of Stability, Control, and Performance Characteristics: FAR and Military Requirements*, Lawrence, Kansas: DARcorporation, 2018.
24. Roskam, J., *Airplane Design Part VIII: Airplane Cost Estimation: Design, Development, Manufacturing and Operating*, Lawrence, Kansas: DARcorporation, 2018.
25. Barrett, R., *Wind Tunnel and Flight Testing Data and Draft*, Lawrence Kansas, 13 May 2021